Technical University of Munich
Department of Physics
Experimental Physics with Cosmic Particles

Master's Thesis

The Pacific Ocean Neutrino Experiment: Photosensor Research and Qualification Setup Development

Eva Laura Winter

28.02.2022

Matriculation No.: 03673381

First Examiner: Prof. Dr. Elisa Resconi
Second Examiner: Prof. Dr. Susanne Mertens

Abstract

The Pacific Ocean Neutrino Experiment (P-ONE) is a future neutrino telescope in the deep Pacific Ocean off the coast of Vancouver Island. Within the infrastructure of Ocean Networks Canada (ONC), a first line of P-ONE is planned to follow the successful deployment of the two pathfinder missions STRAW ("STRings for Absorption length in Water") and STRAW-b (part b). The design of this first moored observatory (P-ONE-1) and its optical modules are currently under development. For the indirect detection of neutrinos via Cherenkov radiation induced by charged particles, photomultiplier tubes (PMTs) are used. To help the selection of the PMTs for the prototype line, a test and calibration setup has been established. The different components are presented focusing on the developed code to operate them, allowing a "plug and play" usage. Different PMT candidates from Hamamatsu, ET Enterprises, and a third supplier, of which results cannot be published in the scope of this thesis, have been pre-selected for evaluation. Measurements to determine the dark rate, the gain and the transit time spread have been performed. The results of those are presented and analysed. Thereafter, the prospects of further measurements to perform a photocathode scan or to determine the quantum efficiency are discussed. After a summary and conclusion, an outlook of the future of P-ONE is given.

Contents

Introduction

The Pacific Ocean Neutrino Experiment (P-ONE) is a multi-cubic-kilometre scale neutrino telescope currently under development. The indirect detection of neutrinos via Cherenkov radiation is performed with photomultiplier tubes (PMT). As there exist different companies that manufacture PMTs and there are differences in shape and performance, a selection and calibration setup is needed to evaluate various possible candidates for the P-ONE prototype line (P-ONE-1). The aim of this work is to develop such a setup that can be remotely operated and functions as a "plug and play" station. Furthermore, first measurements with several PMT candidates to compare their different characteristics were performed to help the selection of the PMT to be used in the P-ONE prototype line.

In order to understand the theoretical background, the basics of astroparticle physics are explained in chapter 1 beginning with a historical introduction. This is followed by an overview of cosmic rays in sec. 1.1 and multi-messenger astronomy in sec. 1.2. Chapter 2 discusses neutrinos, the particles to be detected with P-ONE, in more detail. The basics of neutrino physics are handled in sec. 2.1, cosmic neutrino sources in sec. 2.2, the principles of high-energy neutrino detection in sec. 2.3, and concluding this chapter, examples of neutrino detectors are given in sec. 2.4. In chapter 3, the developed concept of the P-ONE prototype line (or P-ONE-1) (sec. 3.1) and the current design of the P-ONE modules (sec. 3.2) are explained. In chapter 4, first, the basics of photomultiplier tubes (sec. 4), and their characterising parameters (sec. 4.2) are explained. After that, the requirements and possible candidates for P-ONE-1 are discussed in sec. 4.3, and an outlook of the calibration of the optical modules is given in sec. 4.4. Chapter 5 covers the experimental part of this work. The designed PMT test and calibration setup is presented by introducing the components (sec. 5.1), the optical fibre path (sec. 5.2), and its systematic uncertainties (sec. 5.3). Furthermore, performed measurements and results are shown in sec. 5.4. Finally, chapter 6 gives a summary and conclusion of this work and chapter 7 an outlook of further developments of the project.

Chapter 1

Astroparticle Physics

Historically, astroparticle physics has its origin in optical astronomy. With increasingly improved measurement techniques, this field of science has evolved into astrophysics, an extensive branch of research. It involves many subfields of physics, like mechanics and electrodynamics, thermodynamics, plasma physics, nuclear physics, elementary particle physics, and special and general relativity. The term *astroparticle physics* is used for the study of particles of astrophysical origin. In order to understand the astrophysical contexts, profound knowledge of particle physics is necessary. Further, as the Universe provides experimental conditions that laboratories can not provide (in the context of vast dimensions or energies), it poses an exceptional environment for high-energy physics [38].

The birth of astroparticle physics can be traced back to the discovery of cosmic radiation by V. Hess in 1912 [42]. The measurements showed that additionally to the terrestrial component, another source of ionising radiation increasing with altitude must exist [38, p. 4]. The discovery of radioactivity by H. Becquerel in 1896 indicated already an extraterrestrial origin [70, p. 4]. The name "Höhenstrahlung", introduced by V. Hess, was soon reinvented by R. A. Millikan. Together with G. H. Cameron, they performed absorption measurements in 1926 and found the radiation to consist of high-energy gamma rays. They called the extraterrestrial radiation "cosmic rays" [26, p. 89].

The belief that cosmic rays consisted mainly of gamma rays persisted until 1928 when J. Clay found that ionisation increased with latitude. This was the proof of the interaction of cosmic rays with the geomagnetic field and hence the composition of mostly charged particles. The confirmation of an electrical charge came soon with the invention of the Geiger-Müller tube in 1928. In 1933, the experiments by L. W. Alvarez and A. Compton, T. H. Johnson, and B. Rossi showed that the radiation was compounded of mostly *positively* charged particles, most probably protons as it could be demonstrated some years later [26, p. 90].

1.1 Cosmic Rays

Today we know that cosmic rays consist of approximately 90% protons, 9% α-particles, and heavier nuclei. They have relativistic and even ultra-relativistic energies up to 10^{20} eV [33, p. 1]. The discovery of such highly energetic particles entering the Earth's atmosphere led inevitably to the study of their sources. While it is not yet fully understood where they originate from, it is believed that most of them come from outside the Solar System but within the Galaxy. Violent events of the Sun pose the primary source for particles of solar origin [33].

Outside the Solar System, the acceleration of high-energy particles is predicted to occur in supernova remnants (SNRs) [70, p. 7] and other even more violent processes in the universe, like active galactic nuclei (AGNs) or gamma ray bursts (GRBs) [26, p. 21]. The research field of astroparticle physics aims to identify these galactic and even extragalactic engines.

Generally, there are two components: *primary* and *secondary* cosmic rays. Primary cosmic rays are high-energy protons, nuclei, and, to a smaller fraction, electrons generated in astrophysical contexts. They fill up the galactic space and hit the Earth's atmosphere with a rate of about 1000 per square meter per second [33, p. 1]. The measurement of these particles and thus of the chemical composition of cosmic rays with energies up to around 10^{14} eV can be done on top or outside the atmosphere [70]. So-called *direct measurements* are done with satellite telescopes like the Alpha Magnetic Spectrometer (AMS) on-board the ISS [14] or the Large Area Telescope (LAT) on-board of NASA's gamma ray satellite telescope Fermi [16]. Due to a low cosmic ray flux of only a few tens of particles per m^2 per year above 10^{15} eV, it is not possible to measure incident particles with such high energies with airborne detectors due to their limited detection area [70, p. 87].

In interaction processes of the primaries with nuclei in the Earth's atmosphere, secondary cosmic rays are produced, so-called air showers. The basic mechanism for a cosmic ray proton p interacting with a nucleon N is [70, p. 8]:

$$p + N \rightarrow \pi^{\pm}, \pi^0, K^{\pm}, K^0, p, n, ... \tag{1.1}$$

The short-lived hadrons decay further into an electromagnetic component consisting of photons, electrons and positrons, and a penetrating part: muons and neutrinos.

The secondary particles with the highest energies can be measured with ground-based detectors, so-called *indirect measurements* [70]. Examples for such detectors are IceCube [4], MAGIC [30] or Super-Kamiokande [31].
At energies larger than few GeV up to 10^{20} eV, the energy spectrum of cosmic rays can be described using a power-law [70, p. 37]:

$$\Phi(E) \propto E^{-\alpha} \tag{1.2}$$

with α, the *differential spectral index*. Fig. 1.1 shows the all-particle spectrum of cosmic rays measured by several *direct* and *indirect* experiments.

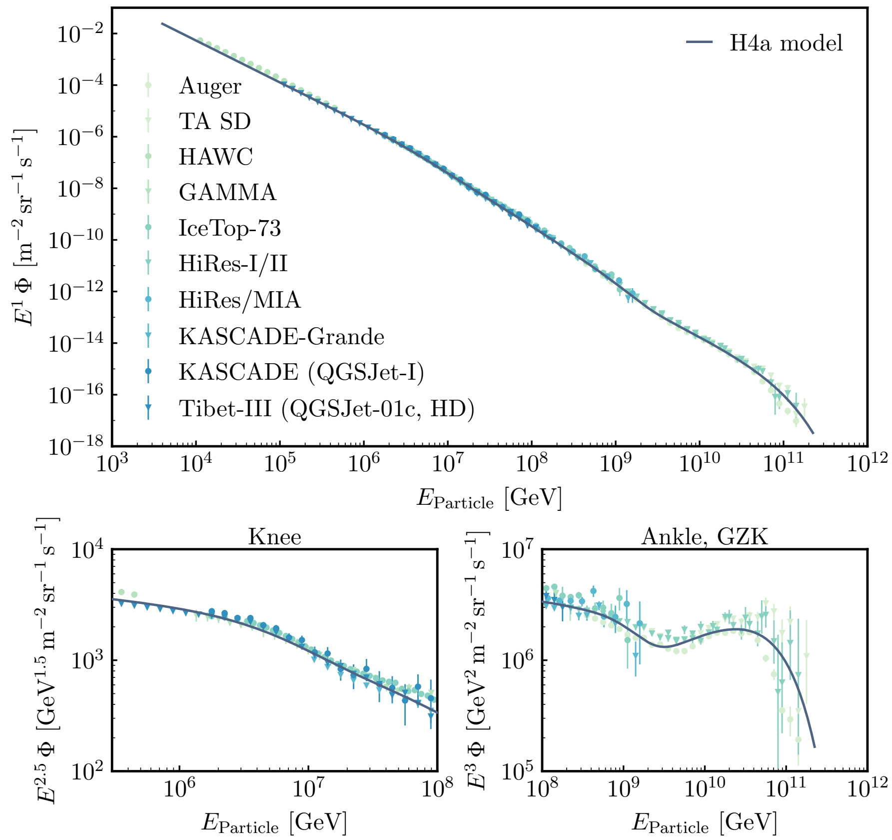

Figure 1.1: High-energy spectrum of cosmic rays with data from various experiments. The full spectrum scaled with E^1 (top) and detailed subplots of the knee (scaled with $E^{2.5}$) and the ankle combined with the GZK cut-off (scaled with E^3) are displayed. Figure courtesy of Felix Henningsen with data from T. Gaisser, R. Engel, E. Resconi [33] and K. Krings.

The *kink* between 10^6 and 10^7 GeV, known as the *knee*, marks the region argued to be the limit for most galactic accelerators [70]. Further, the *ankle* is situated at roughly 10^{10} GeV and poses presumably the transition point to cosmic rays with extragalactic origin [26, 70]. However, details of acceleration mechanisms at those energies are not yet fully understood. Lastly, the ultra-high-energy cut-off at about 10^{11} GeV can be explained via the interaction of protons with cosmic microwave background (CMB) photons [70, p. 216]:

$$
\begin{aligned}
p + \gamma_{\mathrm{CMB}} \rightarrow \Delta^{+} &\rightarrow n + \pi^{+} &\quad (1.3)\\
&\rightarrow p + \pi^{0}. &\quad (1.4)
\end{aligned}
$$

Further decays show that in the final state there is always a proton with reduced energy

$$
\begin{aligned}
\pi^{0} &\rightarrow \gamma\gamma &\quad (1.5)\\
\pi^{+} &\rightarrow \mu^{+} + \nu_{\mu} &\quad (1.6)\\
n &\rightarrow p + e^{-} + \bar{\nu}_{e}. &\quad (1.7)
\end{aligned}
$$

This means that the cosmic ray protons have a threshold above which their energy is reduced, and high-energy photons and neutrinos are produced. This effect was independently predicted by K. Greisen, G. Zatsepin and V. Kuzmin in 1966 and is therefore called the *GZK cut-off* [36, 74]. Another explanation for the cut-off in the energy spectrum could be that cosmic accelerators do not have the power to produce higher-energy particles in observable numbers [70].

1.2 Multi-Messenger Astronomy

Most of the present knowledge of the universe was gained by detecting cosmic messengers [71]. Historically, the first observations were made by measuring different forms of light. Not only visible light but also other wavelengths of the electromagnetic spectrum were discovered throughout the development of advanced experimental techniques. This includes infrared, ultraviolet, radio, X-ray, and gamma ray radiation. The detection of this wide range of radiation helped improve our knowledge of astrophysical processes. In the 1960s, for example, new measurement techniques were developed to detect wavelengths in the radio region [71]. In that way, the cosmic microwave background, pulsars, and quasars were discovered. As most electromagnetic radiation is blocked by the Earth's atmosphere, airborne detectors are needed to measure these photons. Therefore, X-ray detectors were brought above the atmosphere with the help of newly developed rockets in the 1960s-1970s. It was not until the 1980s that new detectors enabled the measurement of individ-

ual photons with energies above GeV, charged cosmic rays, neutrinos and, finally, gravitational waves. This led to unexpected discoveries as e.g. the detection of a neutrino burst from a stellar gravitational collapse in 1987. The first detection of solar neutrinos marks the start of *multi-messenger astronomy* (MMA): the combined detection of multiple cosmic messengers of one astrophysical object or process. In summary, there are four different cosmic messengers: photons, electrically charged subatomic particles (cosmic rays), neutrinos, and gravitational waves [71].
Due to their different physical characteristics, especially their electrical charge and mass, they traverse the Universe differently. Cosmic messengers carry various information about their sources, and the detection techniques need to be distinct. Fig. 1.2 explains the different propagations of cosmic rays, gamma rays and neutrinos from their source to Earth.

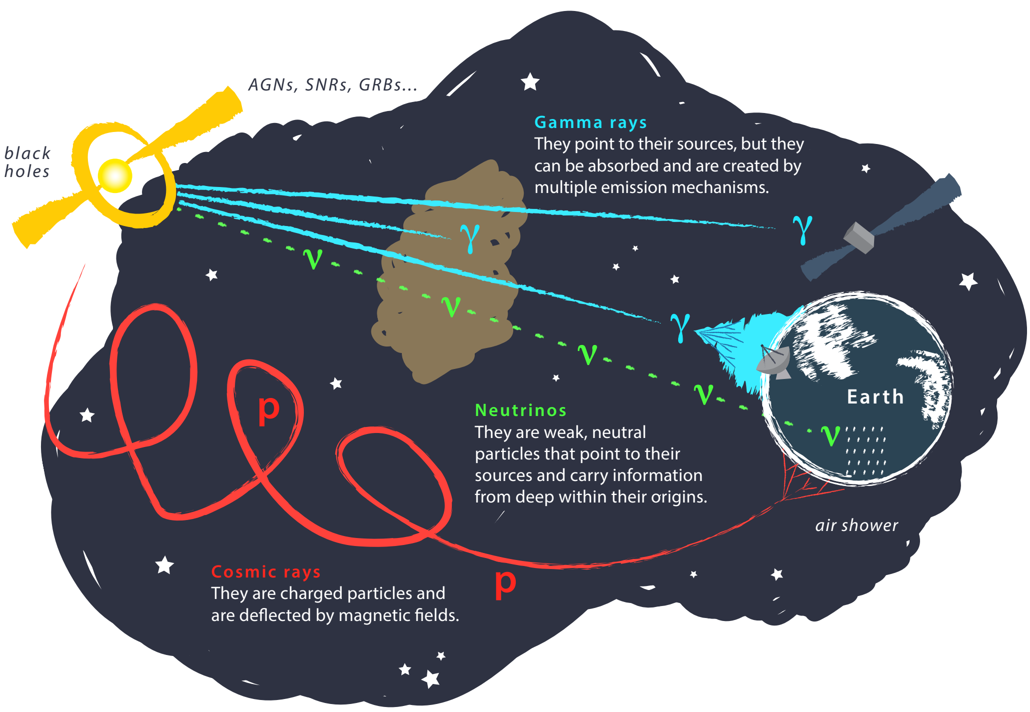

Figure 1.2: Concept of Multi-messenger astronomy. Depicted are gamma rays, neutrinos, and cosmic rays emitted from an astrophysical source. They differ in their propagation due two varying electric charge and mass. Figure from [45].

Charged Particles As explained above, the term *cosmic rays* comprises protons, α-particles, heavier nuclei, and electrons. The relative abundances can be measured with satellite telescopes like AMS on-board the ISS [14].

Since charged particles are deflected from their initial path by intergalactic magnetic fields, they propagate spiralling through the Universe. This causes a problem in identifying their sources as they do not point directly to them. The combined measurement of cosmic rays and other cosmic messengers emitted from the same source helps to address this problem [19].

The largest cosmic ray detector is the Pierre Auger Cosmic Ray Observatory. It uses two measurement techniques: Cherenkov detectors and telescopes detecting the fluorescent emission from the ionised particles in the shower. Since Cherenkov radiation is also an essential physical phenomenon for the detection of neutrinos, it will be discussed in detail in sec. 2.3.

Gamma rays The most energetic part of the electromagnetic spectrum are gamma rays. The highest energy ever detected of a gamma ray photon was around 450 TeV with the Crab Nebula as origin [19, p. 177].

The study of gamma rays aims to understand the astrophysical environments they originate from. Gamma rays travel along straight paths, which is advantageous for identifying their sources. It is, however, possible that they interact with CMB photons on their way and produce pairs of electrons or positrons. The deflection by magnetic fields of these electrically charged particles makes it impossible to determine the initial gamma ray photons [68]. On the other hand, beams of gamma rays travelling non-deflected to us point directly to their sources. They are produced in violent processes, like SNRs, AGNs or gamma ray bursts (GRBs). The interaction of charged particles near the acceleration sites (*hadronic model*) or the synchrotron emission from relativistic electrons moving in a magnetic field (*leptonic model*) are possible explanations for a high-energy photon flux [70].

As the Earth's atmosphere is not transparent to gamma rays, they can only outside the atmosphere be directly measured [70]. The FermiLAT on-board of NASA's gamma ray satellite telescope [16] performs regular all-sky scans and detects numerous gamma ray sources. The detector is capable of measuring energies of up to 300 GeV [70, p. 262].

The other possibility of gamma ray detection is to measure the photons indirectly by analysing the produced secondaries following the interaction with a nucleus of the atmosphere. Like charged particles, also gammas induce cascades when hitting the Earth's atmosphere. The term *cosmic ray* can thus be extended to charged particles and gamma ray photons.

There are gamma ray detectors that can be directly pointed to a particle shower.

The MAGIC telescope [30], for example, measures Cherenkov radiation and can automatically distinguish between electromagnetic showers produced by gamma rays, and hadronic showers produced by charged particles [19, p. 279f]. The MAGIC collaboration contributed, together with FermiLAT and IceCube (sec. 2.4), to the identification of the multi-messenger event blazar TXS 0506+56 [46, 47, 59].

Neutrinos The third cosmic messenger displayed in fig. 1.1 is the neutrino. Neutrinos are elusive particles with almost no mass, electromagnetically neutral, and very rarely interacting with other particles [70].
Neutrinos are produced as secondaries in cascades when primary cosmic rays or photons hit Earth's atmosphere. However, they are also emitted by the Sun [25] and in violent processes such as Supernovae [43]. Other possible source candidates are SNRs, GRBs, and there has been evidence for neutrino emission from AGNs [34, 46, 47, 59]. Due to their small cross section, they can emerge from deep inside the core of astrophysical objects. Hence, they can reveal the innermost physical processes of these environments. In addition, they propagate the Universe on unimpeded paths and experience no deflection by magnetic fields. These advantageous features distinguish neutrinos from other cosmic messengers [70, 38]. Albeit, large detector volumes are needed to detect these penetrating particles.

Gravitational Waves The so-far least explored cosmic messengers are gravitational waves predicted by A. Einstein in 1915 in his theory of General Relativity. When massive objects undergo acceleration, they can disturb the curvature of space-time and produce gravitational waves. This gravitational wave transports energy in the form of gravitational radiation. The first direct observation was made when the LIGO telescopes detected gravitational waves for the first time in 2015 [54]. The signal originated from the merger of two black holes, causing a local gravitational field deformation. This structural change propagated at the speed of light and generated ripples in the fabric of space-time. The resulting velocity difference of a laser beam, depending on its orientation, was measured with two independent Michelson interferometers [19, 38].

In order to probe the acceleration sites of highly energetic particles, this thesis focuses on neutrino detection. The following chapter 2 explains the underlying physics (sec. 2.1) and the detection principle (sec. 2.3), and presents neutrino detectors (sec. 2.4).

Chapter 2

Neutrinos

In 1930, Pauli predicted the existence of a new particle as an explanation for the missing momentum when a neutron spontaneously decays into proton and electron and called it *neutrino* [19]. Today, we know that an electron anti-neutrino carries the rest energy and momentum of a β-decay [27, p. 176]:

$$n \rightarrow p + e + \bar{\nu}_e \tag{2.1}$$

Neutrinos can be used as cosmic messengers. As aforementioned, they can help us understand astrophysical environments and processes once detected. The key feature of cosmic neutrinos is that they point us directly to their sources due to their low interaction cross section. However, this poses also the most significant challenge in detecting them. This chapter gives an overview of the fundamental physics of neutrinos and their astronomical sources. A more detailed discussion on detecting high-energy neutrinos and examples for neutrino detectors will complete this chapter.

2.1 Neutrino Physics

To understand neutrino interactions and why neutrino detectors are designed the way they are, this section briefly explains their role in the Standard Model and neutrino oscillations.

2.1.1 Neutrinos as part of the Standard Model

The Standard Model of particle physics is a unifying theory of elementary particles and their interactions. It combines the fundamental forces (strong, electromagnetic, and weak), their mediators (gauge bosons) and the affected fermions (leptons and

quarks) as well as the Higgs boson. It is not possible yet to include the gravitational force coherently, which indicates some limitations of the Standard Model [64, p. 205].
Neutrinos are spin-1/2-particles and belong thus to the fermions. Together with the electron e^-, the muon μ^-, and the tau τ^-, they are leptons. While e^-, μ^-, and τ^- have electric charge, the corresponding neutrinos (ν_e, ν_μ, ν_τ) are electrically neutral and do hence not take part in electromagnetic interactions. As leptons are naturally unaffected by strong interactions, neutrinos interact only weakly. The mediators of the weak interaction are the $W^\pm$ and the Z^0 bosons, which couple to the flavour of particles. Due to their large masses ($\mathrm{m}_W \approx 80\,\mathrm{GeV}$ and $\mathrm{m}_Z \approx 91\,\mathrm{GeV}$) [64, p. 4], the weak interaction is strongly suppressed compared to the electromagnetic and the strong interaction. Weak processes are characterised by their mediator. The exchange of a $W^\pm$ boson is called *charged current* (CC) and the one of a Z^0 boson *neutral current* (NC). Further, they can be categorised in leptonic, semi-leptonic, and hadronic processes, depending on the involved fermions [75]. Exemplary Feynman diagrams of leptonic processes are given in fig. 2.1a, 2.1b and of semi-leptonic processes in fig. 2.1c, 2.1d.

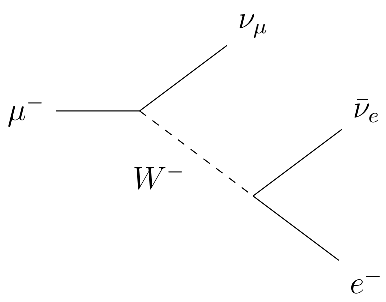

(a) Muon decay (CC) $\mu^- \to e^- + \nu_\mu + \bar{\nu}_e$

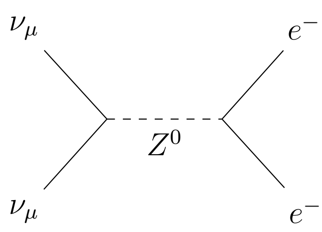

(b) Neutrino-electron scattering (NC) $\nu_\mu + e^- \to \nu_\mu + e^-$

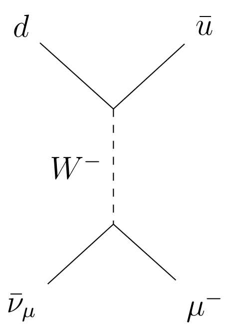

(c) Pion decay (CC) $\pi^- \to \mu^- + \bar{\nu}_\mu$

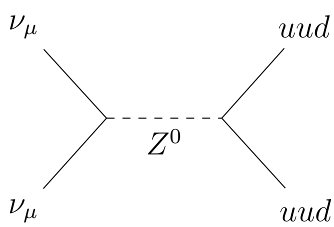

(d) Neutrino-proton scattering (NC) $\nu_\mu + p \to \nu_\mu + p$

Figure 2.1: Feynman diagrams of exemplary **leptonic** (top) and **semi-leptonic** (bottom) processes. Data taken from [37, p. 66, 68].

2.1.2 Neutrino Oscillations

In weak interactions, neutrinos are identified by the corresponding *flavour eigenstates* $|\nu_e\rangle$, $|\nu_\mu\rangle$, and $|\nu_\tau\rangle$. However, neutrinos can change their flavour, which is called *flavour* or *neutrino oscillation*. This effect emerges since neutrinos also have *mass eigenstates* $|\nu_1\rangle$, $|\nu_2\rangle$, and $|\nu_3\rangle$, which are a quantum-mechanical superposition of the flavour eigenstates. In the case of a non-zero mass, those eigenstates are not identical and can mathematically be described using a rotation matrix [64, p. 166]

$$\begin{pmatrix} |\nu_e\rangle \\ |\nu_\mu\rangle \\ |\nu_\tau\rangle \end{pmatrix} = \begin{pmatrix} U_{e1} & U_{e2} & U_{e3} \\ U_{\mu 1} & U_{\mu 2} & U_{\mu 3} \\ U_{\tau 1} & U_{\tau 2} & U_{\tau 3} \end{pmatrix} \cdot \begin{pmatrix} |\nu_1\rangle \\ |\nu_2\rangle \\ |\nu_3\rangle \end{pmatrix} \tag{2.2}$$

This matrix is called Pontecorvo-Maki-Nakagawa-Sakata (PKMS) matrix. It is parametrised by the mixing angles θ_{12}, θ_{23}, θ_{13}, and a CP-violating phase δ. Several experiments, like Double Chooz [6], or Super-Kamiokande [31], are investigating the values of those parameters using neutrinos of terrestrial, atmospheric, or solar origin [70, p. 414].

The time dependence of the neutrino eigenstates can be derived using a unitary mixing matrix U. Assuming neutrinos with momentum p emitted by a source at $x = 0$ and time $t = 0$, the mass eigenstates $|\nu_i\rangle$ show a time dependence as follows

$$|\nu_i(x,t)\rangle = \mathrm{e}^{-\mathrm{i}E_i t}|\nu_i(x,0)\rangle \tag{2.3}$$

with

$$|\nu_i(x,0)\rangle = \mathrm{e}^{\mathrm{i}px}|\nu_i\rangle \tag{2.4}$$

with the relativistic energy

$$E_i = \sqrt{m_i^2 + p_i^2} \simeq p_i + \frac{m_i^2}{2p_i} \simeq E + \frac{m_i^2}{2E} \tag{2.5}$$

while $p \gg m_i$, $E \approx p$ denotes the neutrino energy. As neutrinos are produced and detected as flavour states, they develop with time into

$$|\nu(x,t)\rangle = \sum_i U_{\alpha i}\mathrm{e}^{-\mathrm{i}E_i t}|\nu_i\rangle. \tag{2.6}$$

The final state is thus different from the initial one for varying neutrino masses. Macroscopically, this effect can become observable despite the small differences in neutrino masses. The time-dependent transition probability for a flavour oscillation $\nu_\alpha \rightarrow \nu_\beta$ is given by

$$P_{\alpha\rightarrow\beta}(t) = |\langle\nu_\beta|\nu(x,t)\rangle|^2 \tag{2.7}$$

$$= \delta_{\alpha\beta} - 4\sum_{j>i} U_{\alpha i}U_{\alpha j}U_{\beta i}U_{\beta j}\sin^2\left(\frac{\Delta m_{ij}^2}{4}\frac{L}{E}\right) \tag{2.8}$$

with

$$\Delta m_{ij}^2 = m_i^2 - m_j^2 \tag{2.9}$$

using CP invariance. Δm^2 is the squared mass difference of neutrino mass eigenstates. It is visible that neutrino oscillations are only possible if at least one mass is different from zero. Further, $L = x = ct$ is the distance between source and detector. An accurate knowledge of L is crucial for the experiment's sensitivity [75, p. 194f]. While an absolute mass limit cannot be measured, the observation of neutrino oscillations allows the determination of the weak mixing angles and the squared mass differences. Experiments like Super-Kamiokande [31], KamLAND [5], or Double Chooz [6] have performed measurements to determine those values.
Experimental data have shown, that $\mid \Delta m_{32}^2 \mid \simeq \mid \Delta m_{31}^2 \mid \gg \mid \Delta m_{21}^2 \mid$ [26]. As the sign of Δm_{21}^2 is yet unknown, there are two possible neutrino mass hierarchies, i.e., the ordering of mass eigenstates, the *normal* (NH) or *inverted* (IH) hierarchy

$$m_1 < m_2 < m_3 \quad \text{(NH)}$$
$$m_3 < m_1 < m_2 \quad \text{(IH).}$$

Determining the actual mass hierarchy is one of the significant aims of current and future neutrino experiments.

2.2 Neutrino Sources

Atmospheric Neutrinos Primary cosmic rays interact with nuclei in the atmosphere and produce secondary particles (see also sec. 1.1, eq. (1.1)). The predominant products are charged pions. With a lifetime of only 26 ns they decay further and produce muon neutrinos, which themselves are unstable and decay with a lifetime of 2.2 μs into neutrinos:

$$\begin{aligned}\pi^+ &\to \mu^+ + \nu_\mu \\ &\quad \mu^+ \to e^+ + \nu_e + \bar{\nu}_\mu \\ \pi^- &\to \mu^- + \bar{\nu}_\mu \\ &\quad \mu^- \to e^- + \bar{\nu}_e + \nu_\mu .\end{aligned}$$

Therefore, the atmospheric neutrino beam contains muon and electron neutrinos with an expected ratio of

$$\frac{N(\nu_\mu, \bar{\nu}_\mu)}{N(\nu_e, \bar{\nu}_e)} \equiv \frac{N_\mu}{N_e} \approx 2. \tag{2.10}$$

While atmospheric neutrinos pose one of the most significant backgrounds for fundamental neutrino astronomy, they have been proven helpful for particle physics research. One of the leading detectors measuring atmospheric neutrinos is Super-Kamiokande. Its measurements showed that while N_e meets the theoretical expectation, N_μ is clearly reduced [32]. This deficit of muon neutrinos indicated neutrino oscillations happening along the path from the source to the detector. If, in reality, the ν_μ was a superposition of two mass eigenstates $|\nu_1\rangle$ and $|\nu_2\rangle$ and these states propagated at varying velocities, they would get out of phase, and the neutrino could change its flavour. This is only possible for different masses because otherwise, all neutrinos would propagate precisely at the speed of light, and the mass components could not get out of phase with each other [38, p. 142ff].

Solar Neutrinos Solar neutrinos provide a direct view into the internal processes of the Sun. Like other active stars, the Sun acts like a nuclear fusion reactor where mainly hydrogen is burned to helium within its core. As such, it is a generator of powerful electron neutrinos in the MeV range. The *pp-chain*

$$p + p \to^2 H + e^+ + \nu_e \tag{2.11}$$

produces approximately 86% of the solar neutrinos via the weak interaction [38, p. 150]. The Sun provides a unique opportunity to study the evolution of stars, with a rate of around $6 \times 10^{10}\,\mathrm{m}^{-2}\mathrm{s}^{-1}$ solar ν_e that reach Earth [71, p. 17]. Further, solar neutrinos are used to study neutrino oscillation parameters, as in Super-Kamiokande [31].

Supernova Neutrinos When a star runs out of elements to fuse, it reaches its final stage, marked by a core collapse and a massive explosion. Stellar material of the outer shells is ejected, and the remaining object forms either a neutron star or a black hole depending on the mass. Approximately 99% of the emitted energy is carried by neutrinos, and 1% is transferred into kinetic energy of the expelled stellar material forming a shock wave. Only about one percent of the kinetic energy is in the form of electromagnetic radiation [70, p. 176f].

The brightest supernova since Kepler's observation in 1604 was detected in 1987. *SN1987A* is part of the Large Magellanic Cloud at a distance of about 50 kpc [33, p. 263].

Cosmogenic Neutrinos As stated in sec. 1.1, high-energy cosmic rays can interact with photons of the CMB and produce secondary particles (eq. (1.4)). In further decays, also neutrinos are created (eq. (1.6) and (1.7)). These so-called *cosmosgenic neutrinos* can reach ultra-high energies up to a few PeV [3].

Relic Neutrinos After the Big Bang, neutrinos were in thermal equilibrium in the hot plasma, filling the Universe. With its expansion, the Universe cooled down, and the rates of weak interaction processes decreased. At rates lower than the expansion rate, neutrinos began to decouple. *Relic neutrinos* or the *cosmic neutrino background* (CνB) would provide unique insight into the very early universe. However, the direct detection is challenging and could not have been performed yet [35].

This section concludes with a complementary collection of models and experimental results for the neutrino spectra mentioned above (fig. 2.2).

2.3 High-Energy Neutrino Detection

High-energy neutrinos are a key signature of astrophysical neutrino sources. Their detection requires a thorough understanding of their interactions with their surroundings. This section focuses first on neutrino interactions in matter and then describes the distinct neutrino signatures caused by the different interaction events.

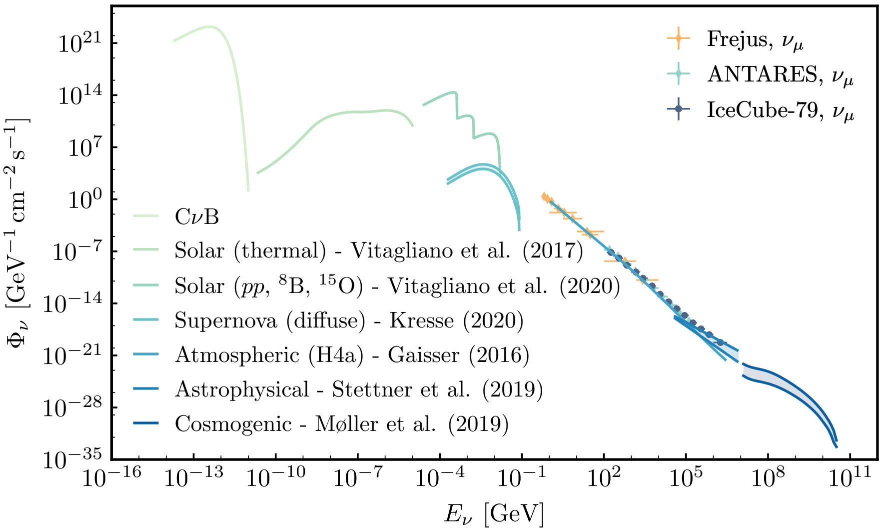

Figure 2.2: Cosmic neutrino fluxes as a function of energy. Figure courtesy of Felix Henningsen with experimental data from Frejus [24], ANTARES [7], and IceCube [4], and exemplary all-flavour model assumptions for solar, supernova, atmospheric, astrophysical, and cosmogenic neutrino fluxes based on data as denoted.

2.3.1 Neutrino Interactions

When high-energy neutrinos travel through matter, they can interact with a nucleon N via charged (CC) or neutral current (NC) processes

$$\nu_l + N \to l^- + X \qquad \bar{\nu}_l + N \to l^+ + X \quad \text{(CC)} \tag{2.12}$$

$$\nu_l + N \to \nu_l + X \qquad \bar{\nu}_l + N \to \bar{\nu}_l + X \quad \text{(NC)} \tag{2.13}$$

with $l = e, \mu, \tau$ representing the corresponding neutrino flavours and X the formed hadronic system [71]. At high energies, the CC interactions are dominated by deeply inelastic scattering processes [35]. The target N absorbs some kinetic energy of the incoming neutrino, which can generate the emission of particles, resulting in the outcoming final state X. However, the produced charged leptons carry away most of the energy and traverse the medium with enormous velocities [33]. If those velocities exceed the speed of light in the medium, light is emitted, which is called the *Cherenkov effect*.

As neutrinos interact only weakly, their interaction cross section is relatively low (in the order of $10^{-38}\,\mathrm{cm}^2 \times E_\nu/(\mathrm{GeV})$ [75, p. 76]), and large volumes in the range of kilometres are needed for the detection [33].

2.3.2 The Cherenkov Effect

The speed of light in a medium is the fraction of the speed of light in vacuum c and the optical refraction index n

$$c_n = \frac{c}{n}. \tag{2.14}$$

A charged particle traversing a medium causes polarisation of the electric field along its path. When the particle has passed, the medium returns to its unpolarised state, releasing energy in the form of electromagnetic radiation. This is known as the *Cherenkov effect*. If the particle travels with a velocity $v < c_n$, the electromagnetic perturbations propagate faster than the particle and eventually arrive randomly at any point in space and annihilate each other. If, however, the particle is faster than the electromagnetic perturbations ($v \geq c_n$), the phases between those are not randomly distributed. They add up to a unified wavefront travelling outwards of the event creating a characteristic light cone with the opening angle θ [72]

$$\cos\theta = \frac{c}{vn} = \frac{1}{\beta n} \tag{2.15}$$

with $\beta = v/c$. This shows the dependence of θ on the particle's velocity, i.e. its energy. Fig. 2.3 shows a depiction of the Cherenkov effect.

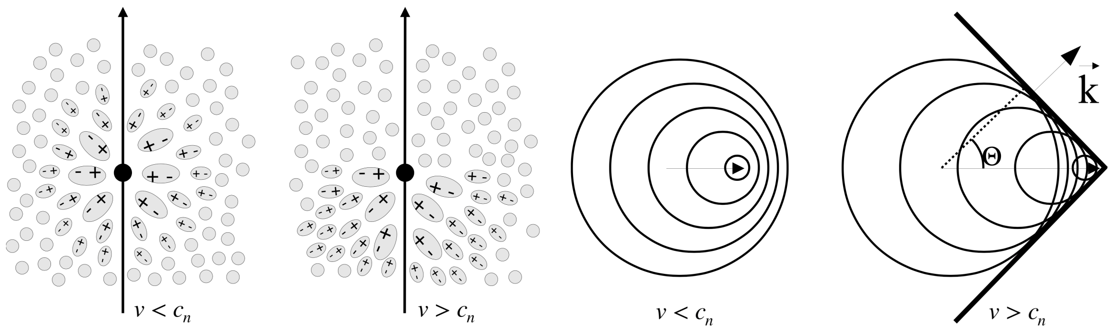

(a) Illustration of the polarisation of the medium induced by the crossing of a relativistic particle.

(b) Construction of a Cherenkov wavefront.

Figure 2.3: Qualitative summary of the Cherenkov effect. The figures on the left show the case for particles with velocities smaller than the local speed of light c_n, the figures on the right depict the case for larger velocities. Figures from [56].

The number of emitted Cherenkov photons per travelled distance is proportional to $1/\lambda^2$ and is most significant in the visible light regime between 300 - 600 nm [1]. Large-volume neutrino detectors are built into water or ice, where the optical properties allow the measurement of the Cherenkov radiation with light sensors.

2.3.3 Neutrino Detection Principle

High-energy neutrinos are detected indirectly by measuring the emitted Cherenkov photons due to relativistic charged secondaries produced in neutrino interactions with the medium. A three-dimensional array of photomultiplier tubes (PMTs, ch. 4) collects the Cherenkov radiation within the volume, usually consisting of water or ice. The number of detected photons and their arrival times are essential information used to determine the neutrino flavour, initial direction, and energy [35, 71].

The choice of water or ice as a detector medium is plausible for several reasons. First, both are available in large quantities like e.g. seas, oceans, or ice in the Antarctic. As indicated before, the neutrino interaction cross section is very low, making it indispensable to instrument large volumes. Secondly, the medium must be transparent for Cherenkov photons and optically clear to avoid deviation and absorption. Crucial characteristics of neutrino telescopes are thus the absorption length and the scattering length of the detector medium, which depend on the wavelength. While a large attenuation length allows a wider spacing of the PMTs, an extensive scattering length is essential for geometry preservation of the Cherenkov radiation. Therefore, the geometry of the detector is determined by the desired detectable energy [75].

Furthermore, neutrino detectors must be deployed deep under the surface to reduce background signals. The atmospheric muon flux exceeds the neutrino interaction rate by far, especially in the low energy range. A shielding of several kilometres can reduce this background. Atmospheric neutrinos, on the other hand, pose an inescapable background source [71, 75].

2.3.4 Neutrino Signatures

The charged particles produced in neutrino interactions travel through the medium until they either decay or interact. The path length, i.e. the mean distance travelled by those secondaries, is dependent on their energy and energy loss propagating through the medium. For example, the path length of a 200 GeV muon corresponds to roughly 1 km [71, p. 358].

There are two basic event types registered in large neutrino detectors: tracks and cascades. CC interactions of muon neutrinos produce tracks that can either enter the detector volume from interactions in the surroundings or are initiated within the detector. In water, Cherenkov photons are emitted with an opening angle of 41° [33, p. 362f], which allows the reconstruction of the track from the timing of photons hitting the photosensors. For that, the light scattering in the detector must not be too severe and the attenuation not too strong. The energy reconstruction of the initial neutrino is affected by stochastic losses as bremsstrahlung, and hadronic interactions of the muons above a critical energy [33].

Cascades are induced by CC interactions of electron and tau neutrinos or by NC interactions of all flavours. Those events can occur inside or near the detector volume. Since they have an extension of only about 10 m, the spacing of the photosensors determines the spatial resolution. However, most of the energy is contained in the detector, and hence the energy resolution is better than for tracks.

A particular case occurs for CC interactions of a tau neutrino. The produced τ generates a hadronic cascade at the neutrino vertex and at the decay vertex after a relatively short path length. For energies E_τ in the PeV range, the two can be separated as long as they occur within the detector volume [33]. A depiction of neutrino event signatures in the IceCube detector is given in fig. 2.4.

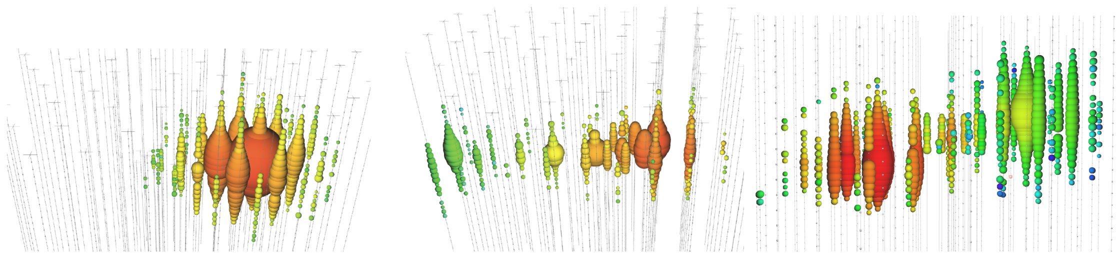

(a) The cascade is the result of an electron neutrino CC interaction or of NC interactions of all neutrino flavours.

(b) The track is the signature of a muon. Muons are the secondary particles of CC interactions of muon neutrinos.

(c) The double-bang is the signature of a tau neutrino CC interaction. Two hadronic cascades occur at the neutrino vertex and at the decay vertex of the tau.

Figure 2.4: Illustration of high-energy neutrino event signatures in the IceCube detector. The dots represent the photosensors, detecting Cherenkov radiation. The size of the dots describes the amount of light detected, the color the arrival time (red to blue corresponds to an early to late arrival time). Figures from [48].

2.4 Neutrino Detectors

The pioneer project for neutrino detectors was DUMAND (Deep Underwater Muon and Neutrino Detector), designed as an array of photomultipliers in the deep-sea close to the Hawaiian shore. However, due to insuperable oceanographic and fi-

nancial challenges, the detector was eventually never realised [29]. Nonetheless, it triggered the development of the successful experiments Baikal-GVD [17, 20], AMANDA (Antarctic Muon And Neutrino Detector Array) [15], and ANTARES (Astronomy with a Neutrino Telescope and Abyss environmental RESearch) [9].
In this section, the main concepts of IceCube and the KM3NeT detectors will be explained. The section will conclude with a prospect of a new neutrino detector, P-ONE, which is currently under development.

IceCube The IceCube neutrino observatory [2], deployed in 2010, is a high-energy neutrino detector in the cubic-kilometre range. As the successor of the AMANDA detector, it is built into the South Pole ice at depths between 1450 and 2450 m. There are 86 vertical strings, each instrumented with 60 evenly distributed digital optical modules (DOM). Each DOM consists of a pressurised glass sphere hosting a downward-facing 10" PMT and circuit boards, allowing operation, data acquisition, communication, and calibration. IceCube is designed to measure neutrinos of all flavours with energies between approximately 100 GeV and 10^9 GeV [2, 49].
Within the In-Ice Array, a much denser instrumented subsystem of IceCube, called DeepCore, is installed. It is designed to have a lower energy threshold and makes hence the detector more sensitive to neutrinos with energies between 10 to 100 GeV. This facilitates the ability to observe atmospheric neutrino oscillations. IceTop, at the surface above the in-ice detection units, consists of 162 ice-filled tanks instrumented with PMTs. It functions as a veto for the detection of downward-going neutrinos. The IceCube laboratory located at the surface in the centre of the array hosts a server room, data acquisition, and online filtering computers [2]. Fig. 2.5 shows an illustration of the IceCube detector and one DOM.
In 2017, IceCube identified, together with Fermi, MAGIC, and several other experiments, a source of extragalactic neutrinos and high-energy cosmic rays for the first time [46, 47, 59]. This marks a breakthrough event for the multi-messenger community.

KM3NeT KM3NeT (km^3 Neutrino Telescope) [55] is a research infrastructure in the deep Mediterranean sea and is currently being constructed. The design and the construction are based on experiences with the pilot projects NESTOR, NEMO, and ANTARES [9] in the deep-sea close to Pylos (Greece), Sicily (Italy), and Toulon (France) [23].
There are two different detector types in KM3NeT: ARCA (Astroparticle Research

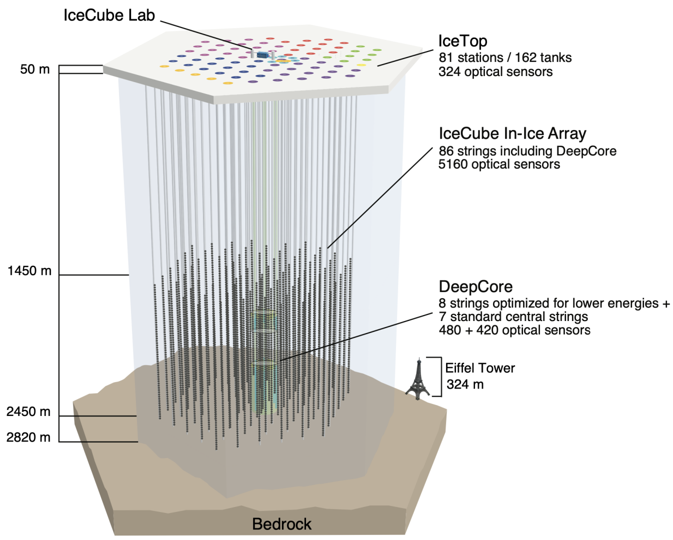

(a) The IceCube Detector

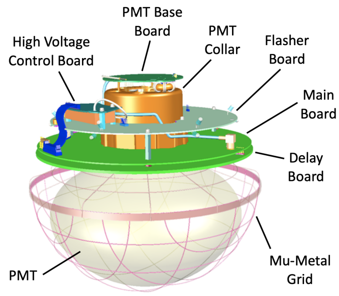

(b) Digital Optical Module

Figure 2.5: A side-view of the IceCube Detector and one DOM. There are over 80 vertical strings built into the ice instrumented with 60 photosensors. Corresponding depths are denoted, as well as a sketch of the Eiffel Tower for size comparison. The different components IceCube Lab, IceTop, IceCube In-Ice Array, and DeepCore are labelled. Please refer to the text for further information. Figures from [2].

with Cosmics in the Abyss) and ORCA (Oscillation Research with Cosmics in the Abyss). They have different sizes and geometries but use the same technology. Vertical detection units instrumented with optical sensors detect the Cherenkov light in the deep-sea. While ARCA will have only twice as many optical modules as ORCA, it will be approximately 100 times as big. A more sparse distribution of detection units in ARCA will enable the detection of high-energy cosmic neutrinos, whereas ORCA will be optimised for lower energy neutrinos and the study of neutrino oscillations [51]. A comparison of the physical sizes and geometries of the two detector types is depicted in fig. 2.6a.

In contrast to IceCube, the optical modules of KM3NeT host several smaller PMTs. One DOM consists of a 17" glass-sphere hosting 31 photomultipliers of 3" diameter and associated readout electronics. By this, the photocathode area is enlarged and segmented, allowing the various PMTs to detect multiple photons arriving at the DOM at the same time. Further, by having an almost uniform angular coverage, the directional information is improved [8]. A photograph of the KM3NeT DOM is depicted in 2.6b.

The already deployed detection units of KM3NeT are already taking data. First results include the atmospheric muon flux in the Mediterranean Sea at depths between ~ 2200 - $3400\,\mathrm{m}$ [10] and, most recently, new findings on the neutrino mass ordering and oscillation parameters [13].

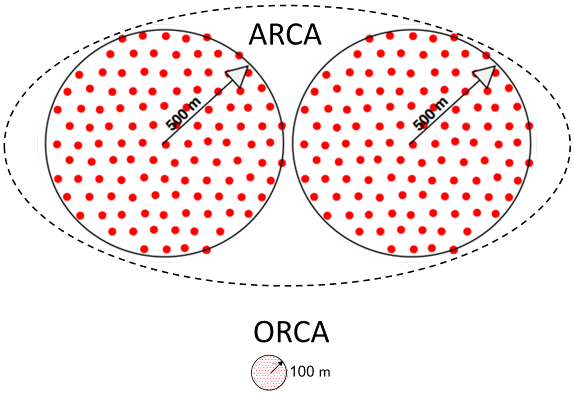

(a) Comparison of the physical sizes of ARCA and ORCA

(b) KM3NeT Digital Optical Module

Figure 2.6: Layout of the KM3NeT Detectors and photograph of one DOM. For more information please refer to the text. Figures from [51].

The Pacific Ocean Neutrino Experiment The Pacific Ocean Neutrino Experiment (P-ONE) is envisioned as a multi-cubic-kilometre neutrino telescope in the deep Pacific Ocean off the coast of British Columbia, Canada [11, 66]. Situated at the Cascadia Basin site within the NEPTUNE observatory of Ocean Networks Canada (ONC) [58], the telescope will complement the neutrino sky coverage. The P-ONE design proposed in [11] and [66] (fig. 2.7) foresees seven clusters of 10 vertical strings with a length of approximately 1 km. Each string will be instrumented with 20 optical modules, including dedicated calibration instruments. The infrastructure of ONC provides communication, data transfer, and power supply.

Using the oceanographic expertise of ONC and the experiences gained in IceCube, and other experiments, the P-ONE collaboration is working on a design to improve the sensitivity at the PeV scale. In 2018 and 202, two pathfinder missions, STRAW (STRings for Absorption length in Water) [21] and STRAW-b [65], with the goal of the characterisation of the site's optical properties [18], have been deployed. Furthermore, those pathfinder experiments proved the feasibility of deploying long vertical instrumented strings at Cascadia Basin. The current status of the development of the first P-ONE line, which also serves as a prototype, will be discussed in the chapter hereafter.

Another approach apart from single detectors instrumenting increasingly large volumes would be the combination of several neutrino telescopes around the globe as one conjoint detector [67]. The prospects and benefits of a global neutrino telescope will be discussed in the outlook of this thesis in chapter 7).

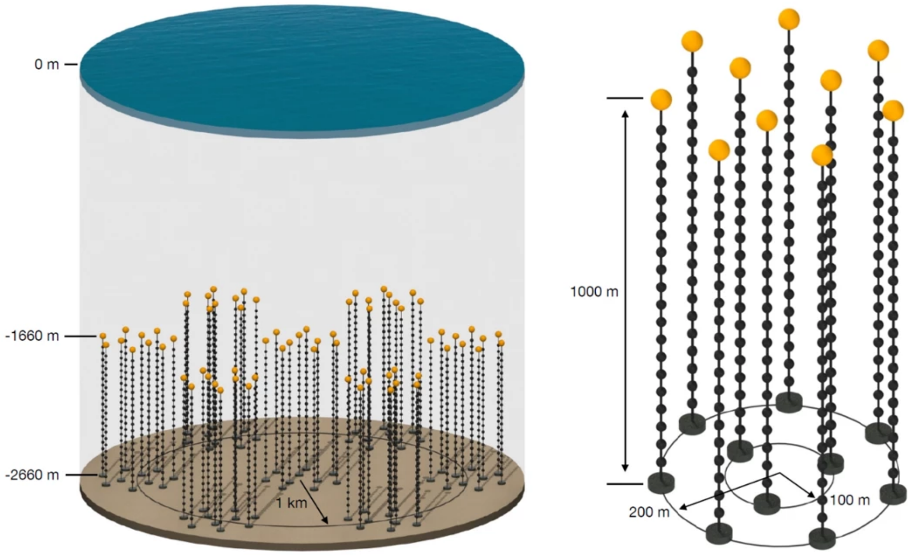

Figure 2.7: Design of the Pacific Ocean Neutrino Experiment. Left figure shows the complete detector consisting of seven clusters. The depth of the Cascadia Basin site is 2660 m. Right figure depicts an individual cluster of 10 strings each with 20 optical modules and a buoy at the top. Figure from [66].

Chapter 3

P-ONE Prototype Line (P-ONE-1)

After the successful deployment of the two pathfinder missions STRAW [21] and STRAW-b [65], the P-ONE Collaboration is currently working on the development of a first line of P-ONE (P-ONE-1). This line aims to be the prototype of the following mooring lines and shall serve as a blueprint for them [69]. This chapter will give an overview of the overall concept and design of the P-ONE prototype line, including the optical and calibration modules, leading over to the task of this work. In the following, P-ONE prototype line and P-ONE-1 will be used synonymously.

3.1 Concept

The P-ONE prototype line has the purpose of being the first operating string of P-ONE. The mooring is envisioned with a length of approximately 1000 m and to host around 16 optical and 4 calibration modules [69]. Next to the mechanical mounting structure for the modules, the string is equipped with an anchor at the bottom and a buoy at the top to ensure steadiness and verticality. Fig. 3.1 shows the current design of the P-ONE prototype line.

Fibre-optical cables will be used for time synchronisation between the individual modules and moorings. The development of the data transfer protocol is currently ongoing, where a reasonable time resolution at possibly picosecond-scale and low power consumption are vital parameters.

With the vision of scalable P-ONE installations, the main objective is the development of a design that can be applied to the follow-up strings. Further, the progress of a deployment strategy that allows the rapid construction of multiple strings is paramount in this project.

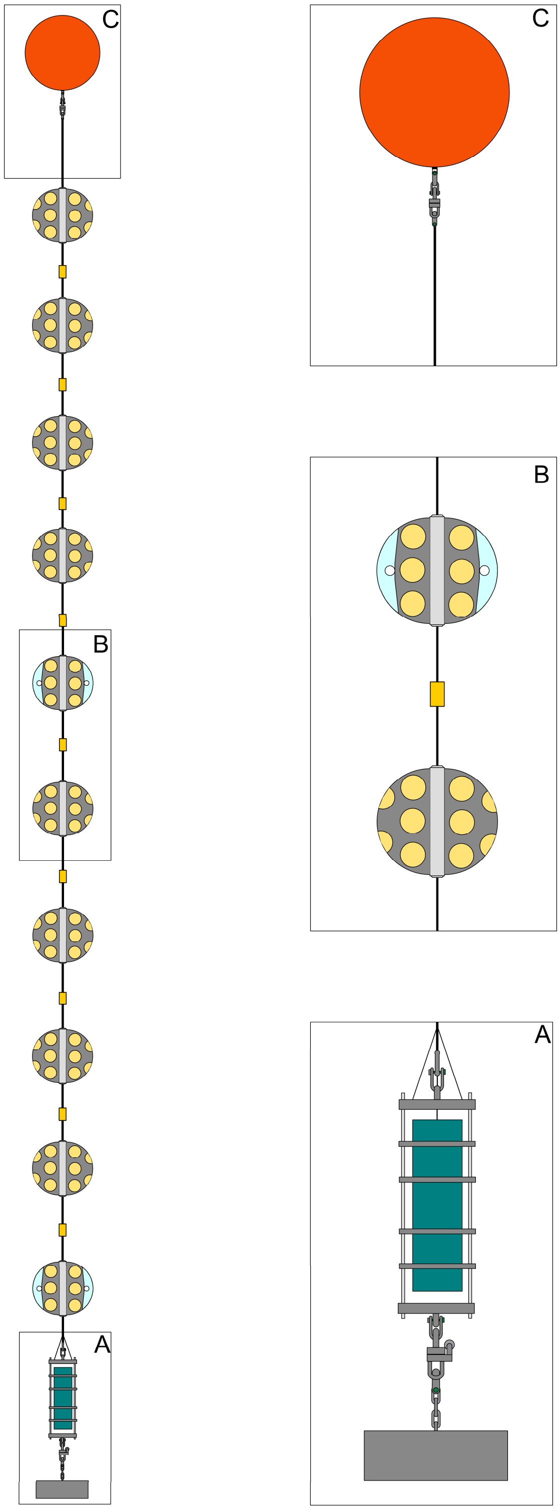

Figure 3.1: Concept of the P-ONE prototype line, depicted with 10 of the planned 20 optical modules. A: anchor and mini junction box, B: calibration module (top) and optical module (bottom), C: buoy. Image from [69].

3.2 Modules

There will be two types of modules for the P-ONE prototype line: the optical module and the calibration module. The former will serve as a light detector for the Cherenkov radiation. The latter will have light emitters used for calibration.

Optical Module The P-ONE optical module will consist of two glass hemispheres assembled through titanium rings to an internal junction box. The module with a diameter of 17" will contain multiple photomultiplier tubes in order to have an ambient view of the surrounding. As anticipated by KM3NeT, a multi-PMT configuration is beneficial within the high light-background environment of the deep Ocean ($\mathcal{O}(10)$ kHz per PMT). As biological processes, that emit photons, are slow compared to the neutrino-induced flashes of Cherenkov light, time resolution at least at nanosecond-scale is required. By this, the discrimination of signal from background events of coincident hits in two or more PMTs is enabled.

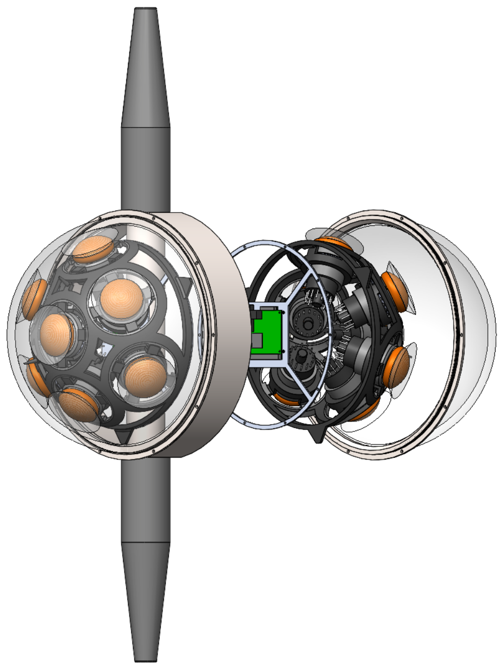

Figure 3.2: Preliminary concept of the P-ONE optical module. Image courtesy of C. Spannfellner and L. Papp.

The current design of the P-ONE optical module (fig. 3.2) foresees photomultiplier tubes with 3-3.5 inch photocathode diameter. Reflective cones around the photosensors shall help increase the modules' effective area and thus the collection efficiency. Further, the PMTs need to be optically coupled to the glass to minimise refraction effects. For this purpose, the study of pre-moulded gel pads to place between the photocathode and the glass sphere is currently ongoing. The internal mounting of the PMTs and supplementary electronics is based on a modular system. A mounting frame with a spring-loaded configuration mechanically supports the tubes. The click-in mounting system allows not only a simplified assembly and disassembly but also reasonable flexibility in case of significant temperature gradients [66, 69].

Calibration Module In order to obtain the best possible data and angular resolution, the optical sensors of P-ONE need to be continually calibrated. The P-ONE calibration module will regularly emit nanosecond isotropic light pulses, detectable by the optical modules. In that way, the optical properties and the geometry of the sensor array can be monitored. However, this approach requires very good time synchronisation between the modules and moorings. This calibration concept has been proven with the first pathfinder mission STRAW [21].
In order to avoid adding complexity to the deployment strategy and mounting system, the calibration module will have the optical module's housing structure. Additionally to the light flashers, the possibility of installing PMTs in the calibration module is currently under investigation. In that way, the module could also function as a Cherenkov light detector and blind spots of the detector can be avoided. The calibration module is depicted in fig. 3.3.

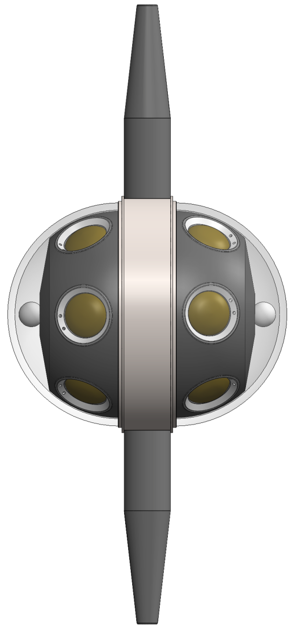

Figure 3.3: Preliminary concept of the P-ONE calibration module. Image courtesy of C. Spannfellner and L. Papp.

The selection of possible PMT candidates and the development of a test and evaluation setup of those was the main task of this work. The following chapter will explain the basic working principle of photomultiplier tubes, followed by an overview of the selection process. In chapter 5, we will introduce the setup developed at the Technical University of Munich to perform analysing measurements of the PMTs and the first results of typical characteristic values will be presented.

Chapter 4

Photomultiplier Tubes

The detection of Cherenkov radiation induced by charged secondaries of neutrino interactions is done with photomultiplier tubes. As the P-ONE optical modules will have a multi-PMT configuration [69], the photosensors need to be examined thoroughly, and different types evaluated beforehand. This chapter will explain the basic working principles and characteristics of photomultiplier tubes. After the theoretical introduction, a list of requirements for the PMTs of the P-ONE-1 line need to fulfil, and attractive PMT candidates will be presented. The chapter will conclude with an introduction to the calibration of PMTs.

4.1 Basic Working Principles

A photomultiplier tube is a highly sensitive detector of weak light signals in the ultraviolet, visible, and near-infrared spectrum. It comprises a photocathode, focusing electrodes, a current multiplier, and an anode within a vacuum glass envelope. An incident photon at the photocathode can excite an electron and induce the emission of a photoelectron into the tube. This is known as the *photoelectric effect* [40]. When supplied with high voltage (HV), the electron is accelerated into the tube. After passing the focusing electrodes, the accelerated photoelectron is directed to the first dynode of a multi-stage system, and secondary electron emission occurs. This is repeated at each dynode of the current multiplier and results in up to 10^7 or 10^8 electrons emitted from the last dynode and extracted from the anode. This multiplication factor is called "gain" and characterises, among other things, a PMT [40, 73].

The gain and other characteristics of a photomultiplier tube are explained in more detail in sec. 4.2. Fig. 4.1 shows the construction of a PMT and illustrates the working principle.

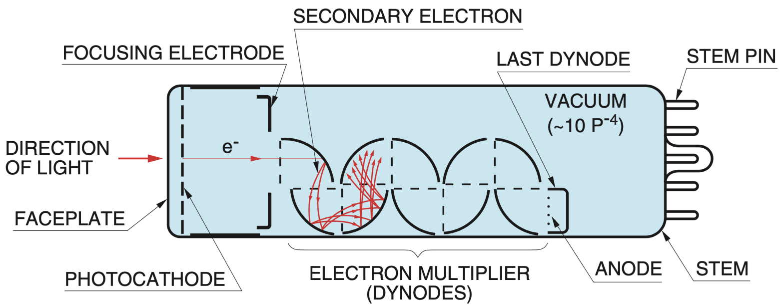

Figure 4.1: Construction of a photomultiplier tube. For more information please refer to the text. Figure from [40].

Photoelectron Emission The conversion of an incident photon at the photocathode into a photoelectron emitted into the vacuum tube is called the *external photoelectric effect*. The maximum kinetic energy of the emitted photoelectron is proportional to the incident photon's energy minus the extraction energy ψ needed for the electron to move to the photocathode's surface and overcome the potential barrier. The so-called work function of a semiconductor thus describes the energy difference between the Fermi and the vacuum level. The escape of a diffused electron into the vacuum tube depends on whether the electron has enough energy $\geq \psi$ and can be described in a probability process. The ratio of the number of photoelectrons to the number of incident photons, i.e. the quantum efficiency, is explained in sec. 4.2. As particularly alkali metals have work functions low enough to be sensitive to visible light, most photocathodes are compound semiconductors with alkali metals. Most commonly used are caesium-antimony (Cs_3Sb), bialkali (K_2CsSb), and multialkali ($Na_2KSb:Cs$) [22, 40].

Electron Trajectory The emitted electron is accelerated and focused onto the first dynode by applying an electric field generated by the high voltage at the electrodes. The electrode arrangement and the applied voltage are configured in a way where the potential distribution between the cathode and the anode is considered, and the motion equation for the electrons is solved[40].

Electron Multiplier When hitting the first stage, the photoelectron is multiplied by a secondary-emissive curved electrode (fig. 4.2). These secondary electrons traverse a multi-stage system of dynodes and are multiplied at up to 19 of such stages (fig. 4.1). The multiplication factor depends on the number of dynodes and, as mentioned above, is called gain [40].

Anode The anode of a PMT is an electrode that collects the emitted secondary electrons. It outputs the current of the collected electrons to an external circuit [40].

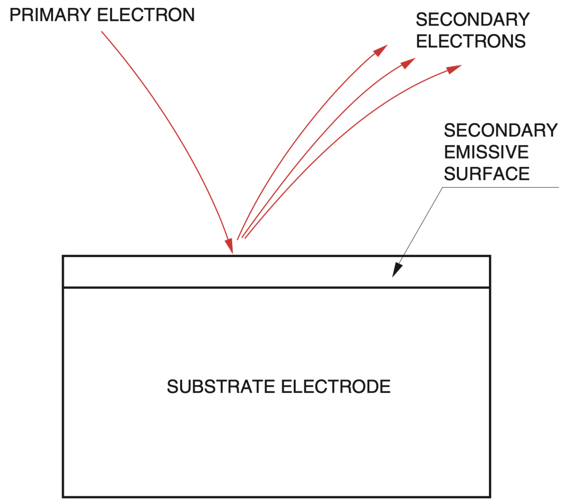

Figure 4.2: Secondary emission model of an electron multiplier. Primary electrons that hit the electrode can excite electrons in the material and induce the emission of secondary electrons. A system of multiple electrodes is used in photomultiplier tubes to amplify the signal of incident photons. Figure from [40].

4.2 Characteristics

This section explains the characterising parameters of photomultiplier tubes.

Quantum Efficiency The quantum efficiency (QE) $\eta(\nu)$, i.e., the ratio of the number of photoelectrons to the number of incident photons, is a function of the wavenumber of light ν and depends on the energy, and thus the wavelength, of the incoming photons and several other parameters. These are characteristics of the photocathode material, such as the reflection coefficient, the total absorption coefficient of photons, and the probability of excitation of electrons to a level greater than the vacuum level. Besides that, the mean escape length of excited electrons and the probability that electrons diffused to the photocathode surface may be released after all into the vacuum affect the quantum efficiency [22, 40].

Collection Efficiency The ratio of electrons landing on the first dynode's effective area to the emitted photoelectrons is called collection efficiency, a function of the supply voltage. At low voltages, the photoelectrons do not enter the effective area of the first dynode or begin their trajectories from unfavourable launch angles. More photoelectrons are collected and traverse the dynode system with increasing supply voltage. Therefore, the collection efficiency can range from 60 to 98 percent [22, 40].

The multiplication product of the quantum and the collection efficiency is the photon detection efficiency (PDE) which is the ratio of the detected signal to the input signal of a PMT (fig. 4.3) [40].

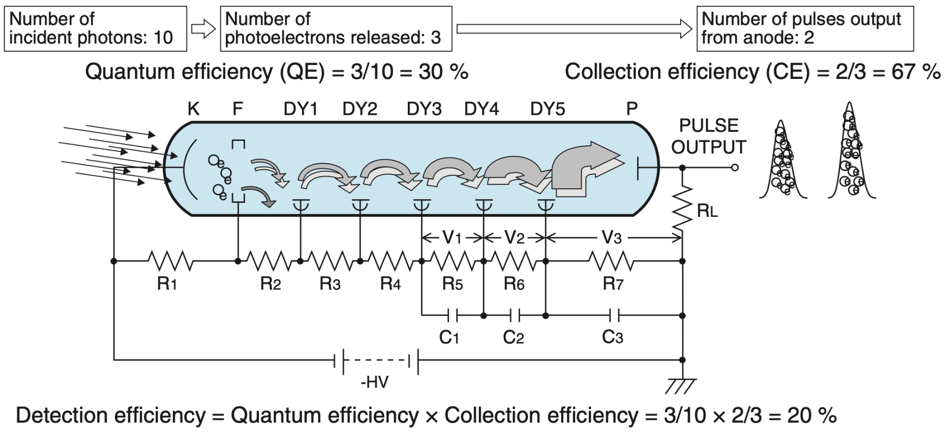

Figure 4.3: Example of photon detection efficiency. Figure from [40].

Gain The gain describes the multiplication factor of one photoelectron after traversing the multi-stage dynode system of a PMT. The gain μ can be expressed with the ratio of secondary electrons emitted from a dynode δ and the number of dynode stages n as follows

$$\mu = \delta^n. \tag{4.1}$$

In this formula, it is assumed that all secondary electrons are collected at the next stage. Losses along the trajectory are negligible compared to the high multiplication factor at the end. The secondary emission ratio δ is proportional to the interstage voltage of the dynodes U_i

$$\delta \propto U_i^k, \tag{4.2}$$

where k is given by the dynodes' material and ranges from 0.7 to 0.8. The gain can therefore be expressed as a function of the supply voltage U_s

$$\mu = A \cdot U_s^{k \cdot n}, \tag{4.3}$$

where A is a constant dependent on the dynodes' material and the number of stages n [40]. A typical gain curve is displayed in fig. 4.4.

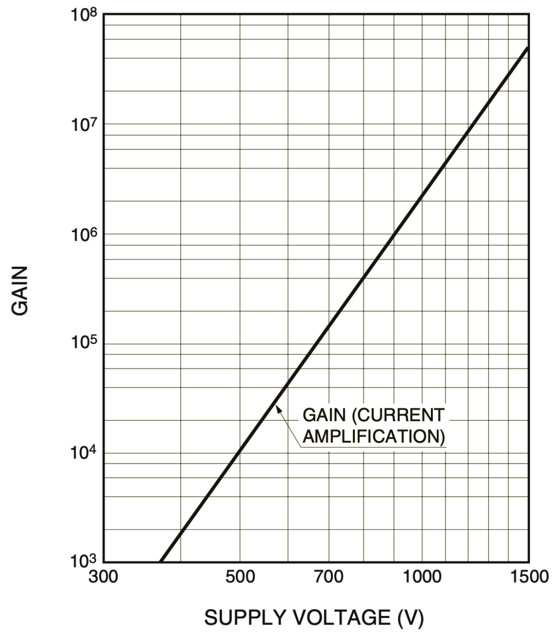

Figure 4.4: Gain of a photomultiplier tube as a function of supply voltage. Figure from [40].

Transit Time The signal waveform of a PMT induced by a short light pulse is characterised by three different time intervals: the rise time, the fall time and the electron transit time (fig. 4.5). The latter describes the time interval between the arrival of a photon at the photocathode and the creation of an output signal at the anode. The rise time is caused by the different transit times of the electrons and denotes an increase from 10 to 90 percent of the maximum output signal. Further, the fall time is the time interval for the pulse to decrease from 90 to 10 percent. Typical values for the rise and fall time are a few nanoseconds, where the fall time is usually longer than the rise time. The electron transit time can range from 16 to 50 ns [40].

Transit Time Spread When illuminated with single photons, the output signals of a PMT differ in electron transit time. These variations are due to the single photons' different initial energies and directions. The FWHM of a transit time histogram for single photons is called the transit time spread (TTS) and is the primary limit to the time resolution of a PMT. Usual values are a few nanoseconds [22, 40].

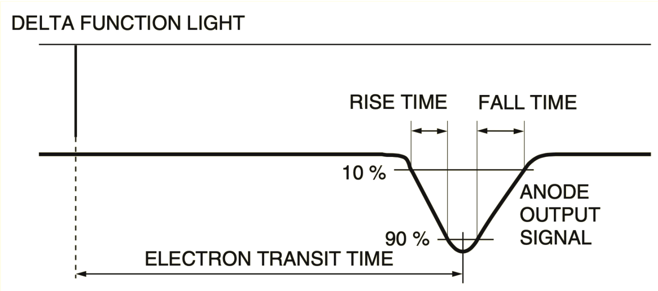

Figure 4.5: Definitions of rise/fall times and electron transit time of a photomultiplier tube. Figure from [40].

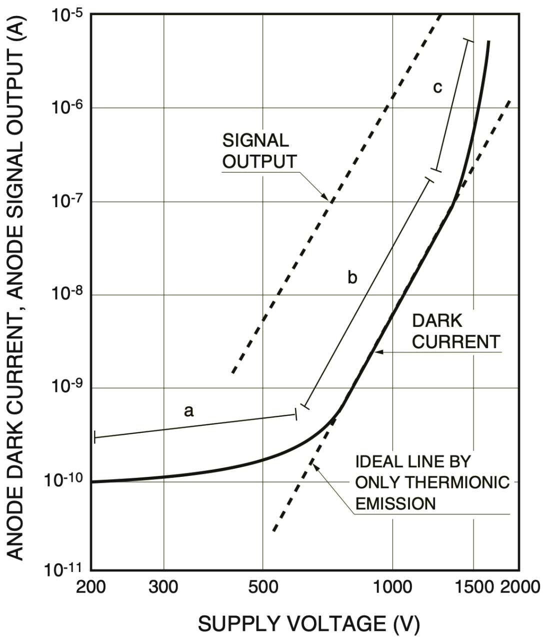

Figure 4.6: Typical dark current vs. supply voltage characteristic of a photomultiplier tube. Figure from [40].

Dark Current and Noise Even when operated in complete darkness, the anode outputs a small current. This so-called dark current is caused by ohmic leakage, thermionic emission, and regenerative effects. Like the signal output, the dark current increases with increasing supply voltage. Fig. 4.6 shows the anode dark current and the anode signal output versus the supply voltage. The curve of the dark current can be divided into three regions: low (a), medium (b) and high (c) supply voltage.

The predominant effect of the low-voltage region is the ohmic leakage. It is caused by imperfect insulations within the tube and is always present. However, the effect is negligible at higher supply voltages, where other sources of dark current dominate.

The main source of the medium-voltage region, which shows a direct proportionality to the gain, is the thermionic emission of electrons. The photocathodes' and the dynodes' surface materials have very low work functions and can emit electrons even at room temperature. The emission of an electron from the photocathode can trigger secondary electron emission with an output signal similar to a single photon event. The rate of those timewise random events usually poses the central part of the dark current. The PMT should be operated in the medium-voltage region as it offers there the best signal-to-noise ratio.
At higher voltages, the photomultiplier tube reaches an unstable region of dark current. Different regenerative effects, such as the production of photocurrent by scintillation from the glass envelope, the electroluminescence from the dynode region, and the back-drift of ions to the cathode, primarily dominate the dark current in this region [22, 40, 52].

4.3 Selection

The main scope of this thesis is to find a suitable photomultiplier tube for the prototype line of P-ONE. As a starting point, a list of requirements for the PMT characteristics has been developed. This was followed by market research and pre-selection of possible PMT candidates, which have been evaluated with the help of a test setup. In the following, the details of these processes will be described.

4.3.1 Requirements

The photomultiplier tubes are essential in neutrino detection and determine the telescope's performance. Therefore, they must satisfy specific technical characteristics to reach the detector's goals. As uncertainties in timing and charge of the detected light affect the track and energy reconstruction of the incident neutrino, they must be reduced. The required parameters are summarised in table 4.1.

4.3.2 Candidates

During the market research, three companies that produce PMTs with the required characteristics were identified: ET Enterprises, Hamamatsu and a third supplier, but results cannot be published in the scope of this thesis. The tubes that fulfil the requirements have been ordered and are listed in table 4.2 together with their main characteristics.

Parameters		
Gain	around 10^6	sufficient signal-to-noise ratio is needed for detecting low-light events
TTS	ideally 2-3 ns, max 5 ns	uncertainties of timing affect track reconstruction
QE	min 20% at 450 nm	important parameter for the detection efficiency and thus for the energy and track reconstruction
Length	as short as possible	satisfy geometry constraints of the optical module
Photocathode	hemispherical with a diameter of ∼3”	maximize effective area of the multi-PMT optical module

Table 4.1: Requirements for the main characteristics of PMTs to be used in the P-ONE prototype line.

Company	**PMT type**	**Photocathode diameter [mm]**		**Gain**	**TTS [ns]**	**QE at peak**
		geometric	**eff. area**			
ET Enterprises	9323KB	82	76	1.0×10^6	3.5	30% (360 nm)
Hamamatsu	R14374	80	72	1.0×10^7	1.3	27% (380 nm)
	R15458	80	72		2.8	
	R14689	90	81		1.5	

Table 4.2: PMT candidates to be tested and their characteristics. Data taken from their respective data sheets [28, 41].

On a side note, the Hamamatsu PMT R15458 is a shorter version of the R12199, which has been used in KM3NeT and STRAW.
For the ET PMTs, two different bases with varying voltage divisions are available. In fig. 4.7 the differences are explained.

9323KB	9323FLB	k	d_1 ········· d_6	d_7	d_8	d_9	d_{10}	a
C636P	C655P	3R	··········	R	R	R	R	R
C636R	C655R	3R	··········	R	1.25R	1.5R	2R	3R

R = 330kΩ

Figure 4.7: ET Enterprises bases with different voltage divisions. The d_i are the connecting points to the PMT pins. Image from [28].

4.4 Calibration

In the scope of the P-ONE project, hundreds of PMTs will need to undergo calibration before they are integrated into the modules. Out of this, a different objective lies in constructing a setup suitable for the calibration of large batches. This setup should be easily accessible to everyone and remotely controllable. The idea is to have a ”plug and play” station that allows simplified and reproducible data taking and evaluation. The calibration of the PMTs is necessary to identify differences in their characteristics, detect malfunctions, and associate the correct high voltage with achieving a specific pre-defined gain value. Further, when finally taking in-situ data and performing data analysis, the knowledge gained from the calibration contributes to the data analysis. Eventually, it can be used to reduce the systematics of the entire system.

Chapter 5

Optical Module Calibration Unit

As described above, the setup that has been developed within this work is designed to measure specific PMT characteristics. To achieve this objective, a *Python* code has been developed to operate the hardware devices and to perform measurements thoroughly from remote. While we concentrate here on the measures with single PMTs, a further goal is to have a setup that, with a few adaptions, will be able to calibrate a complete optical module. This setup will be called Optical Module Calibration Unit (OMCU) in the further documentation.
In this chapter, the different setup components, the structure of the code, the optical fibre path, and the systematic uncertainties of the OMCU will be illustrated and discussed. Finally, performed measurements and results will be presented.

5.1 Setup Components

The OMCU is hosted in a dark box and consists of a rotation stage, a high voltage (HV) supply for the PMTs, and a reference photodiode. Supplementary devices like power supplies (PSU), an Arduino, a picoammeter, and a picoscope are connected from the outside. As light source serves a 405 nm laser, controllable via a laser control device. The laser's output is attenuated and coupled to an optical fibre and divided into two branches. While one fibre is guided into the dark box, the other is coupled to a photodiode connected to a power meter. The instruments are controllable via a dedicated computer. A drawing of the setup with its hardware components is shown in fig. 5.1.
The dark box consists of a galvanised steel box that acts as a Faraday cage and blocks external electric fields. To attain maximised darkness, the leakage of no light was ensured by covering the inner walls with black cloth, and additionally, all cable feed-through holes have been sealed with foam. The setup is pictured in fig. 5.2.

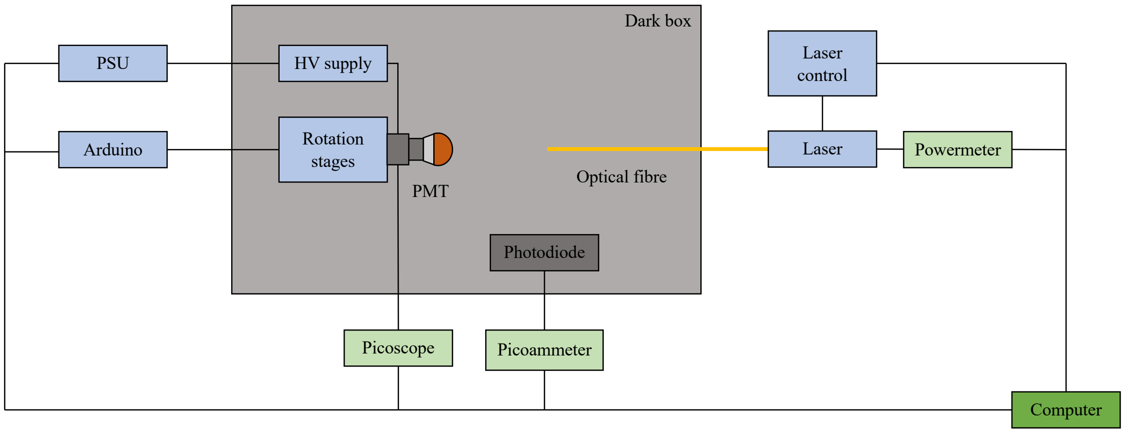

Figure 5.1: Drawing of the OMCU setup with all hardware components. Depicted is the dark box with the devices inside: a photomultiplier mounted on rotation stages, a HV supply, a photodiode, and an optical fibre guided into the box. Connected from outside are power supplies, an Arduino, a laser and a laser control device, a power meter, a picoscope, and a picoammeter. All instruments are coupled to a dedicated computer for remote control. Devices illustrated in blue are supplementary or signal generating devices; green instruments are used for detection.

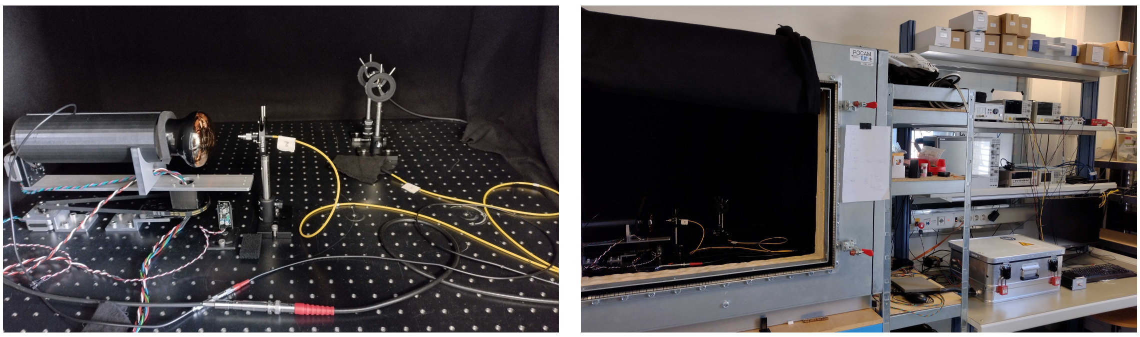

Figure 5.2: Photographs of the OMCU setup. The left picture shows the rotation stage with a mounted PMT, and the laser output fibres with mounting rings. One output fibre is directed at the centre of the PMT, the other can be placed in a mounting ring directed at the diode, that is connected to the picoammeter. The right picture depicts the whole setup with the electronic devices next to the dark box. The laser is placed inside a small dark box on the desk, and its output fibres are fed into the big dark box.

The overall structure of the code is quite simple: each instrument has its class with the necessary functions to operate it. Starting a device is done by calling the according class. To make sure the correct instrument is called, they have fixed names in the device list of the computer. After initiating classes, the required functions can be executed sequentially to perform measurements. After that, the collected data is written into an *hdf5* file and saved on the computer. Details of the measurement and analysis scripts follow in sec. 5.4. In the following, the basic concepts of the devices used in the OMCU setup are explained.

5.1.1 Picoscope

Most of the data needed for the PMT characterisation is taken by the picoscope. Some of its main characteristics are shown in table 5.1.

Picoscope 6424E (Pico Technology)

channels	bandwidth	sampling frequency	buffer size	resolution
4	500 MHz	5 GS/s	4 GS	8-12 bit

Table 5.1: Main characteristics of the OMCU picoscope. Data from [61].

The picoscope can be remotely operated using standard *C* functions. Typically, a sequence of commands needs to be executed successively for taking data [63]:

- open scope unit
- set up input channel with required voltage ranges and coupling type
- set up triggering
- start collecting data
- wait until scope unit is ready
- copy data to buffer
- close scope unit

On the *PicoTech* Github page [62] examples of such sequences can be found. These have been used to understand the structure and the required parameters. The *Picoscope* class defines functions for each of those steps and combines them in measurement functions. There, we differentiate between measurements with one or two channels turned on. Whereas the first is capturing waveforms continuously, the latter is needed for trigger induced signals, e.g. a laser pulse. This will be explained in more detail in sec. 5.4. Some parts of the code can be found in the appendix (code A.1).

5.1.2 Laser

A laser control unit helps to operate the used picosecond pulsed diode laser. Its main characteristics are displayed in table 5.2.
The laser can be handled remotely via serial connection to a computer using predefined commands. For the OMCU setup those were adapted for the *Python* code.

Laser PiL040-FC (NKT Photonics)

output	wavelength	spectral width	pulse width	peak power
FC/APC	405±15 nm	<5 nm	<45 ps	>160 mW

max. repetition rate	avg. power at max. repetition rate
40 MHz	>0.4 mW

Table 5.2: Main characteristics of the OMCU laser. Data from [60].

A code snippet introducing the *Laser* class an be found in the appendix (code A.2). The part shows how the pre-defined functions are converted to Python using the example of turning the laser on or off and getting information about its current status.

5.1.3 Picoammeter

The picoammeter is coupled to a photodiode inside the dark box and measures its current output. When hit by light, the induced current signal of the diode can be monitored with the picoammeter. Like that, a reference measurement of the laser output can be done and compared to the PMT signal. Due to reflections from the second laser output, the measurements are influenced. Therefore, the diode needs to be put in a lightproof box, together with the output fibre dedicated for this measurement. Table 5.3 lists some of the main characteristics of the picoammeter.

Picoammeter 6482 (Keithley)

channels	reading frequency	resolution	dynamic range
2	900 Hz	1 fA	1 fA-20 mA

Table 5.3: Main characteristics of the OMCU picoammeter. Data from [50].

5.1.4 Supplementary Devices

The supplementary devices needed to perform measurements are two power supply instruments, two rotation stages, and a power meter connected to the laser output via a diode. The main parameters are listed in table 5.4.

The power supply devices provide power to the HV supply for the PMT and the Arduino to operate the rotation stage. The *PSU* class defines functions to adjust the voltage and current output and to turn the output on or off (see A.3). This is also used to tune the HV of the PMT bases via a control voltage.

<table>
<tr><th colspan="4">Power Supply GPD-3303S (Gwinstek)</th></tr>
<tr><td>channels</td><td colspan="2">output voltage</td><td>output current</td></tr>
<tr><td>3</td><td colspan="2">2x 0-30 V, 1x 2.5/3.3/5.0 V</td><td>0-3 A</td></tr>
<tr><th colspan="4">Rotation stage RSA1 (Kurokesu)</th></tr>
<tr><td>min. rotation angle</td><td>stepper motor angle</td><td>radial load</td><td>axial load</td></tr>
<tr><td>0.025°</td><td>1.8°</td><td>20 N</td><td>50 N</td></tr>
<tr><th colspan="4">Power meter 2936-R (Newport)</th></tr>
<tr><td colspan="2">sampling rate</td><td colspan="2">measurement rate</td></tr>
<tr><td colspan="2">250 kHz</td><td colspan="2">10 kHz</td></tr>
</table>

Table 5.4: Supplementary devices of the OMCU setup with their main characteristics. Data from the corresponding data sheets [39, 53, 57].

A rotation stage consisting of two stepper motors for the rotation in two planes has been built. A cylindrical, 3D-printed mount holds the PMT and rotates around its longitudinal axis. The second rotation occurs in the x-y-plane of the setup. The angles φ and ϑ describe the position of the PMT and can be set using the functions of the *Rotation* class. The *home* position (0,0) indicates that the PMT is directly "looking" at the laser output fibre. Fig. 5.3 shows a technical drawing of the rotation stage with a mounted PMT. More details regarding the rotation stage can be found in the master's thesis of C. Fink.

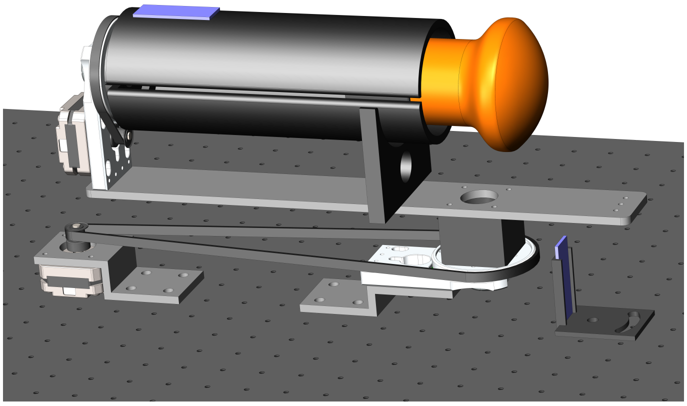

Figure 5.3: Drawing of the rotation stage of the OMCU setup with mounted PMT. Two stepper motors allow the rotation in two planes. Image courtesy of C. Fink.

The powermeter functions as a reference measurement device for the laser output.

It is connected to a diode coupled to one output fibre of the laser. The output is given in Watts. When turning the laser on, an increase of the output power can be observed within the first 5-6 minutes. Afterwards, the value becomes stable. For that reason, a waiting period of 6 minutes is implemented between turning on the laser and taking data.

5.2 Fibre Path

As mentioned at the beginning of this chapter, the laser output is divided into more output channels. Before the first splitting, the output fibre is coupled to an optic attenuator. After that, 90% of the output signal is guided to a power probe, a photodiode, connected to the power meter and the other 10% into the dark box. There, the laser output is again split into 50:50, where one end is illuminating the PMT and the other the photodiode inside the dark box. The splitting fractions have been tested using the powermeter. While the 90:10 splitting was measured to be correct, the 50:50 splitting was measured to be 63:37. This should be taken into account when comparing the different outputs. However, this is no effect on the relative measurements with the PMTs.
Further, it is important to consider the optic fibre connectors. There are two types of fibre-optic connectors (FC): FC/PC with flat polished tip and FC/APC with angle polished tip. The laser output and the attenuator have FC/APC connectors, whereas the splitters use FC/PC connectors. In order to couple the items correctly, a hybrid fibre is used in between. The fibre path with the different connectors is displayed in fig. 5.4.

5.3 Systematic Uncertainties

When performing measurements, the systematic uncertainties of the determined values need to be taken into account. In the OMCU setup, there are different sources of uncertainties.
First, the external power supplies have an uncertainty of 0.001 V. The amplification factor by the HV supply is 250, while the error has been estimated with 5%. The error of the resulting HV value can be calculated using Gaussian error propagation (see appendix, sec A.3.2).
The time resolution of the picoscope is 0.2 ns. However, the Δx between two sampling values is 0.8 ns, which means an uncertainty of 0.4 ns.

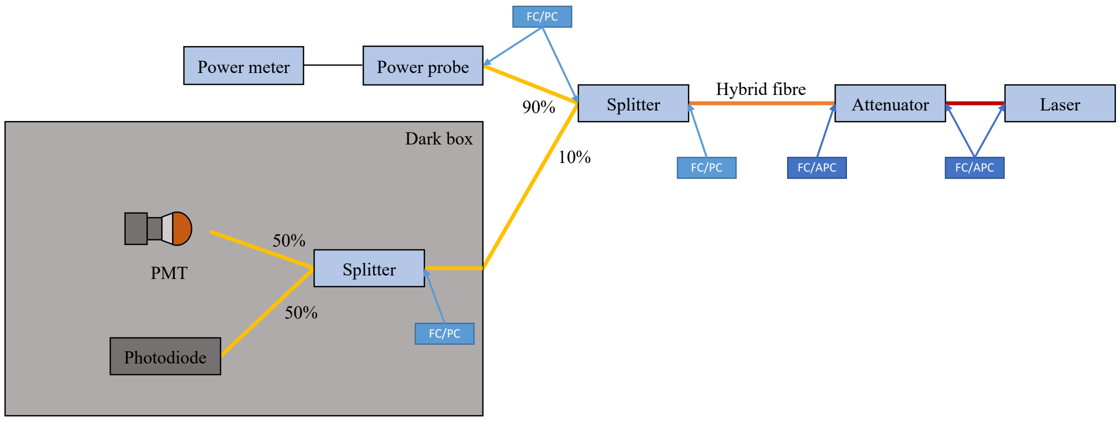

Figure 5.4: Drawing of the optic fibre path with splitters and connectors of the OMCU setup. Splitting fractions are indicated with percentages next to the fibres. Different connectors are labelled with FC/PC, or FC/APC respectively.

How the calculated values, in the following, are affected by systematic uncertainties is explained respectively. The details of the calculations can be found in the appendix A.3.

5.4 Measurements and Results

For the evaluation of the different PMT candidates, various measurements have been performed with two samples of each of the different candidates: three different types from Hamamatsu, one from ET Enterprises (see table 4.2), and one from a third supplier, but results cannot be published in the scope of this thesis. ET Enterprises provides two bases with different voltage divisions (sec. 4.3, fig. 4.7). Both have been used for the measurements and are referred to as "base A" or "A" and "base B" or "B" in the following. The techniques and results are presented hereafter.

5.4.1 Dark Rate

To measure the dark rate of a PMT, the tube is placed inside the dark box. The power cables are connected to the HV supply and the signal cables to the picoscope. After turning on the power supply, a waiting period of 30 minutes is started to reduce the PMT's noise. Then, the measurement is started: the picoscope collects 10^5 waveforms for different supply voltages and writes the data into an *hdf5* file. The pseudo-code 5.1 shows the basic structure of the dark rate measurement.

Code 5.1: Structure of dark rate measurement

```
turn Psu on
wait 1800 s
Vctrl = [3.6, 4.0, 4.4, 4.8, 5.2] # control voltage; the HV supply
    converts: HV = 250*Vctrl
for V in Vctrl:
    Psu settings: channel 2, voltage=V, current=0.1
    data collection of channel 2, 1e5 waveforms without trigger event
    data is written into hdf5 file
```

The dark rate is calculated by counting the pulses that exceed a threshold and dividing the number of counts by the total time interval of the measurement. The width of each pulse is subtracted from the total time as, during this interval, no further pulses could be generated or counted. The threshold is set to 1/3 of the single photoelectron (spe) amplitude, but at least just above the noise band. Especially for the ET PMTs, the threshold needs to be adjusted to a value above the noise band since the spe amplitude is small and 1/3 is within the noise band. The minimum pulse width is set to 2 ns. Table 5.5 shows the results for the tested PMT candidates at room temperature. Unfortunately, no dark rate date for the base A measurements with the ET PMTs is available.
The calculation of the uncertainty can be found in the appendix A.3.1.

Company	PMT type	HV [V]	Dark rate [kHz]
Hamamatsu	R14374 (1)	1100	18.4 ± 0.8
	R14374 (2)	1100	31.6 ± 1.0
	R14689 (1)	1100	16.7 ± 0.8
	R14689 (2)	1100	19.4 ± 0.8
	R15458 (1)	1100	1.8 ± 0.2
	R15458 (2)	1100	3.3 ± 0.3
ET Enterprises	9323KB (1A)		n/a
	9323KB (2A)		n/a
	9323KB (1B)	1300	13.6 ± 0.7
	9323KB (2B)	1300	37.4 ± 1.2

Table 5.5: Measured dark rates of the tested PMT candidates.

The measured dark rates are high in comparison to, for example, the PMT characterisation measurements performed for KM3NeT [12]. Due to limitations by the setup, the maximum amount of waveforms is 10^5. That adds up to a maximum period of 28 ms, with a time interval T=280 ns per waveform. Therefore, the error of the dark rate is relatively high, and higher statistics would be needed. The data taking needs to be changed to a triggered system for a more precise measurement of the dark rate. Additionally, a longer waiting period before taking data will reduce the dark current. Further, performing the measurements at lower temperatures could decrease thermionic emission effects.

5.4.2 Single Photoelectron Signal

The signal pulse induced by a single photon hitting the PMT's photocathode has a characteristic shape. It is defined by the amplitude and pulse width and depends on the applied voltage. Therefore, the PMT is placed inside the dark box and is illuminated with an attenuated pulsed laser beam. The output fibre is directed at the centre of the photocathode and situated at 4 cm distance. The frequency of the laser pulses is set to 10 kHz. To ensure single-photon output, the ratio of pulses passing a determined threshold to the total number of waveforms collected must be below 10%. This ratio is called "occupancy" and is checked before starting a measurement. If it is higher than 10%, the laser output can be attenuated by changing the *tune* value of the laser. To have not too low statistics for the evaluation, the tune value is oppositionally changed if the occupancy is below 2%. Once the occupancy reaches a value between 2% and 10%, the picoscope starts the collection of 10^5 waveforms. The waveforms passing the threshold are saved into an *hdf5* file. This is repeated for different supply voltages. The scheme of this measurement is described in the code 5.2.

Code 5.2: Structure of single photon measurement

```
turn Psu on
Vctrl = [3.6, 4.0, 4.4, 4.8, 5.2] # control voltage; the HV supply
   converts: HV = 250*Vctrl
number = 1
for V in Vctrl:
    Psu settings: channel 2, voltage=V, current=0.1
    tune = 710
    Laser settings: tune value
    data collection, trigger on Laser channel
    calculate occupancy with a threshold of 2 mV
```

```
while occupancy < 0.02:
    tune = tune-5
    Laser settings: new tune value
    data collection, trigger on Laser channel
    calculate occupancy with a threshold of 2 mV
while occupancy > 0.10:
    tune = tune+5
    Laser settings: new tune value
    data collection, trigger on Laser channel
    calculate occupancy with a threshold of 2 mV

data collection of 1e5 waveforms, trigger on Laser channel
calculate occupancy with a threshold of 2 mV

check for every pulse whether the maximum value is above the
    threshold of 2 mV
if yes, write into hdf5 file
```

The picoscope measures the created current output

$$I = \frac{\mathrm{d}Q}{\mathrm{d}t} = \frac{U(t)}{R} \tag{5.1}$$

when a photon hits the PMT's photocathode. The scope's input impedance is $R = 50\,\Omega$.

The mean waveforms of the collected data at different supply voltages from 900 V to 1300 V/1500 V have been determined and are shown for one of each tested Hamamatsu PMT (fig. 5.5) and for one ET PMT with both bases A and B (fig. 5.6). The plots for all of the tested PMTs are depicted in the appendix (sec. A.2.1).

It is visible that the Hamamatsu PMTs perform similarly, while the ET PMT has smaller amplitudes. This indicates a smaller gain for these PMT candidates. Measurements with base A for the ET PMT show a higher amplitude than with base B. In the next step, the gain values of the PMTs are calculated.

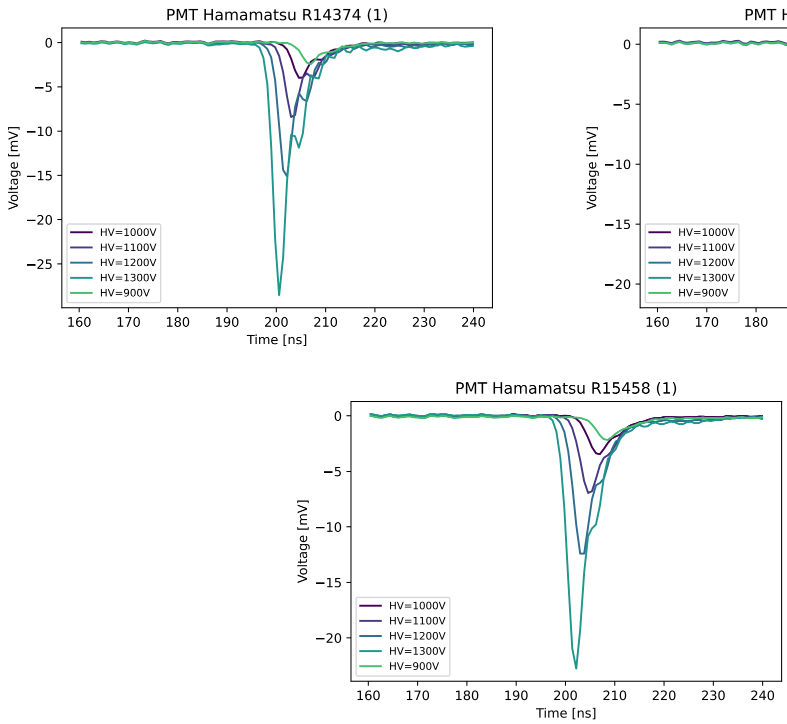

Figure 5.5: Average waveforms of the single photoelectron signal for one of each tested Hamamatsu PMT.

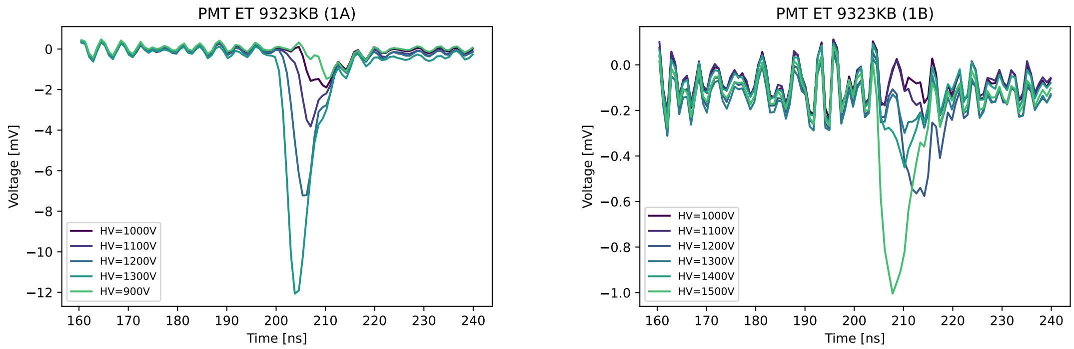

Figure 5.6: Average waveforms of the single photoelectron signal for one ET PMT with both bases A and B.

5.4.3 Gain

For the gain determination, the pulse signals of the single photon events are analysed. Formula 5.1 shows that the area under the curve

$$\int U(t)\,\mathrm{d}t \tag{5.2}$$

is proportional to the created charge Q in one pulse

$$Q_{\text{pulse}} = \frac{1}{R} \int U(t)\,\mathrm{d}t. \tag{5.3}$$

The gain can be calculated by dividing Q_{pulse} by the elementary charge e

$$gain = \frac{Q_{\text{pulse}}}{e}. \tag{5.4}$$

The charge values of the single photon events are calculated and put into a histogram. With a Gaussian fit curve, the mean value can be determined. By using formula 5.4, the gain can be calculated. This has been done for all the PMTs for the different supply voltages. Fig. 5.7 and 5.8 show the charge/gain-histograms of one of each tested PMT type. The histograms of the Hamamatsu PMTs are displayed at HV=1100 V. Due to the lower gain of the ET PMTs, the histograms are shown at HV=1300 V. No fit could have been made for 1000 V and 1100 V with base B. The histograms of all tested PMTs at different voltages are shown in the appendix (A.2.2).
The charge/gain histograms show the single photoelectron distribution fitted with a Gaussian. The peak at around 0 represents dark noise pulses. These waveforms fulfil the requirement of exceeding a threshold, but their peak is before or after the typical transit time, which means they are not induced by the laser pulse.
The mean values of the gain are then put together into a graph displaying the gain dependence on the supply voltage. The data is fitted to a curve to obtain the necessary supply voltage for a specific gain value. Fig. 5.9 shows the gain-HV dependence with errorbars and fitting curve for one of each tested PMT type. As for the ET PMT, the mean value of the gain could not have been determined for most of the HVs with base B, only base A is depicted. The plots for all other PMTs are shown in the appendix (A.2.3). The errors in y-direction arise from the fit function in fig. 5.7 and 5.8. The x-errors are the systematic uncertainties of the supply voltage (see appendix A.3.2).
The HV values for gain values of 5×10^6 and 1×10^7 have been calculated using the fit parameters. They are depicted in the plots (fig. 5.9) and listed in the table 5.6. The uncertainties have been calculated using Gaussian error propagation (see appendix A.3.2 for calculations).
The results of fig. 5.9 and table 5.6 show that the Hamamatsu PMTs have indeed higher gains at lower voltages than the ET PMTs. However, this can be circumvented by supplying higher voltages. It is further visible that base A from ET

Enterprises shows more promising results.

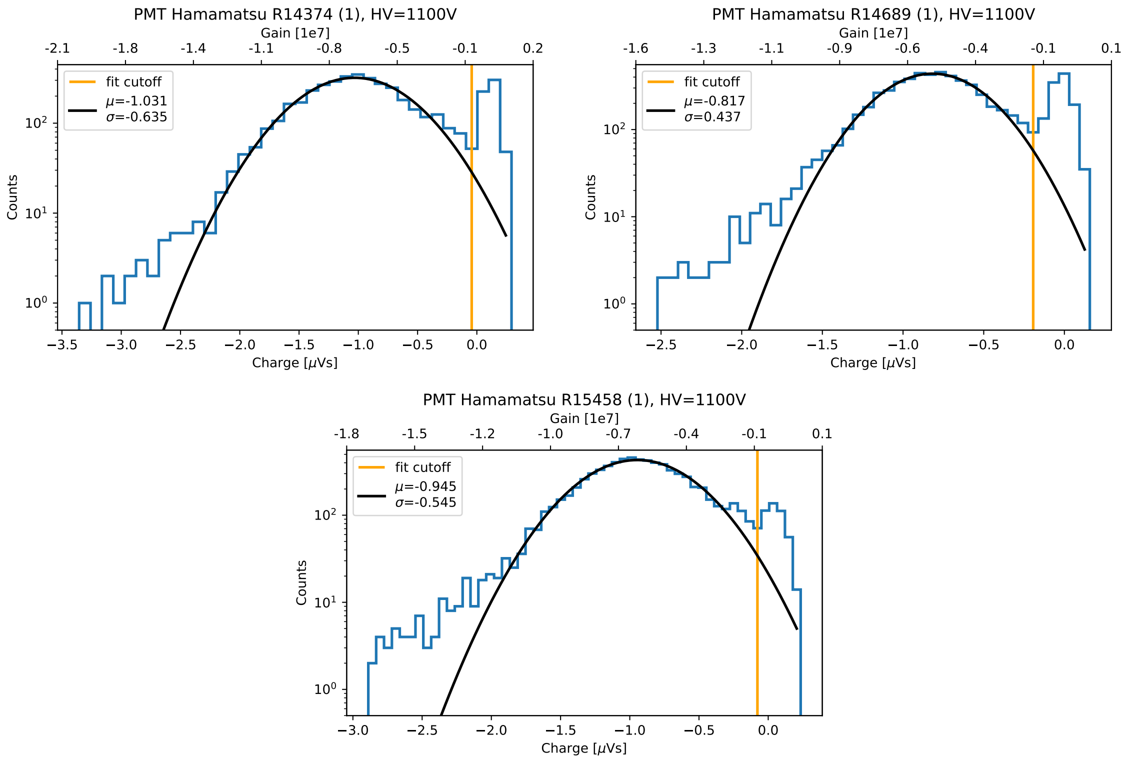

Figure 5.7: Single photoelectron charge/gain distribution at HV=1100 V for one of each tested Hamamatsu PMT. The peak at around 0 represents dark noise pulses. The Gaussian fit curve of the spe charge distribution is depicted in black, the parameters μ and σ are given in the legend. The vertical line marks the y-value of the fit cutoff.

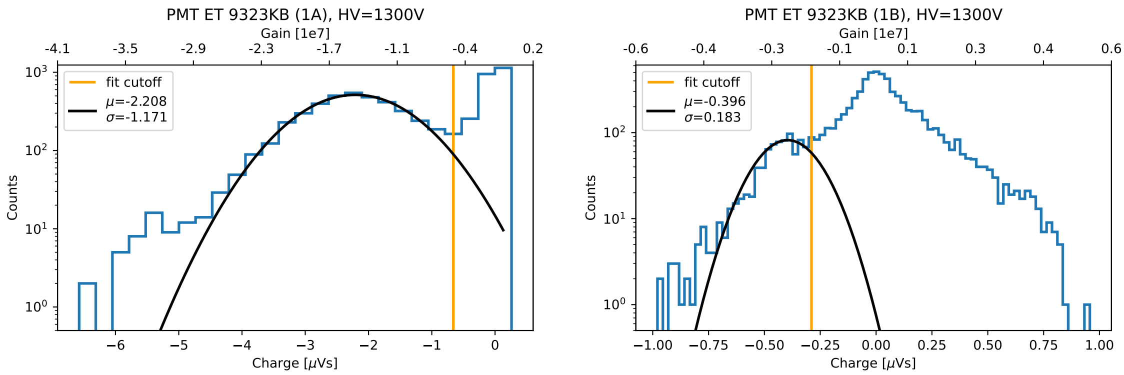

Figure 5.8: Single photoelectron charge/gain distribution at HV=1300 V for one ET PMT with both bases A and B. The peak at around 0 represents dark noise pulses. The Gaussian fit curve of the spe charge distribution is depicted in black, the parameters μ and σ are given in the legend. The vertical line marks the y-value of the fit cutoff.

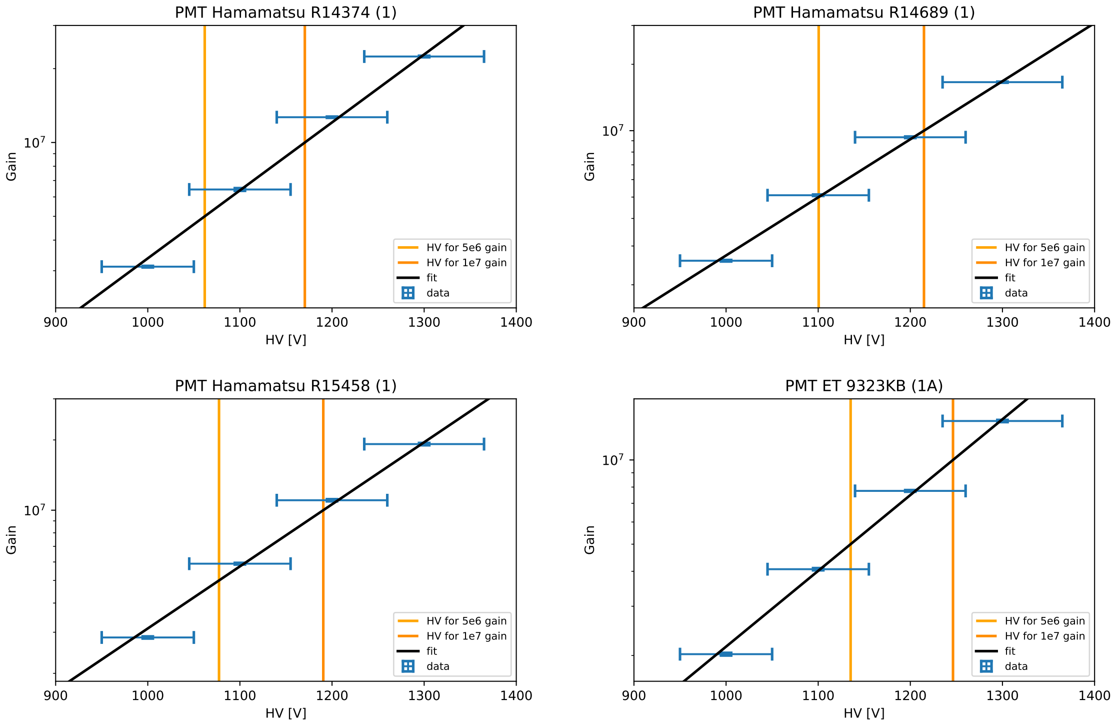

Figure 5.9: Gain dependence on supply voltage with errorbars, fit curve, and vertical lines at y-values of gain=5×10^6 and 1×10^7 for one of each tested PMT candidate.

Company	**PMT type**	**HV [V]** gain $= 5 \times 10^6$	**HV [V]** gain $= 1 \times 10^7$
Hamamatsu	R14374 (1)	1061 ± 69	1170 ± 72
	R14374 (2)	1072 ± 95	1183 ± 100
	R14689 (1)	1101 ± 44	1215 ± 46
	R14689 (2)	1133 ± 34	1251 ± 36
	R15458 (1)	1077 ± 72	1191 ± 75
	R15458 (2)	1071 ± 73	1180 ± 76
ET Enterprises	9323KB (1A)	1135 ± 54	1246 ± 57
	9323KB (2A)	1334 ± 206	1483 ± 219

Table 5.6: Calculated HV values for gain= 5×10^6 and 1×10^7 from the fit curve of the charge/gain histograms for all tested PMT candidates.

5.4.4 Transit Time Spread

The transit time of a PMT is the time difference between the rising edge of the trigger and the pulse signal. When put into a histogram, the TTS is described by the FWHM of a gaussian fit curve and shows the statistical fluctuations as explained in sec. 4.2. The TTS measurements have been performed with the data of the previous measurements of all PMT candidates. The threshold was set to 1/3 of the single photoelectron pulse. The transit time histograms at HV = 1100 V of one of each tested Hamamatsu PMT with fit curve are shown in 5.10. The transit time histograms of one ET PMT with both bases A and B and at HV = 1300 V are depicted in 5.11. The transit time histograms of all testedPMTs at all HVs are shown in the appendix A.2.4.

The calculated values of the TTS of all tested PMTs are presented in table 5.7. However, for one of the ET PMTs no significant pulses could be found when using base B. No histograms were plotted, and no TTS values were determined. The uncertainties have been calculated using Gaussian error propagation (see appendix A.3.3).

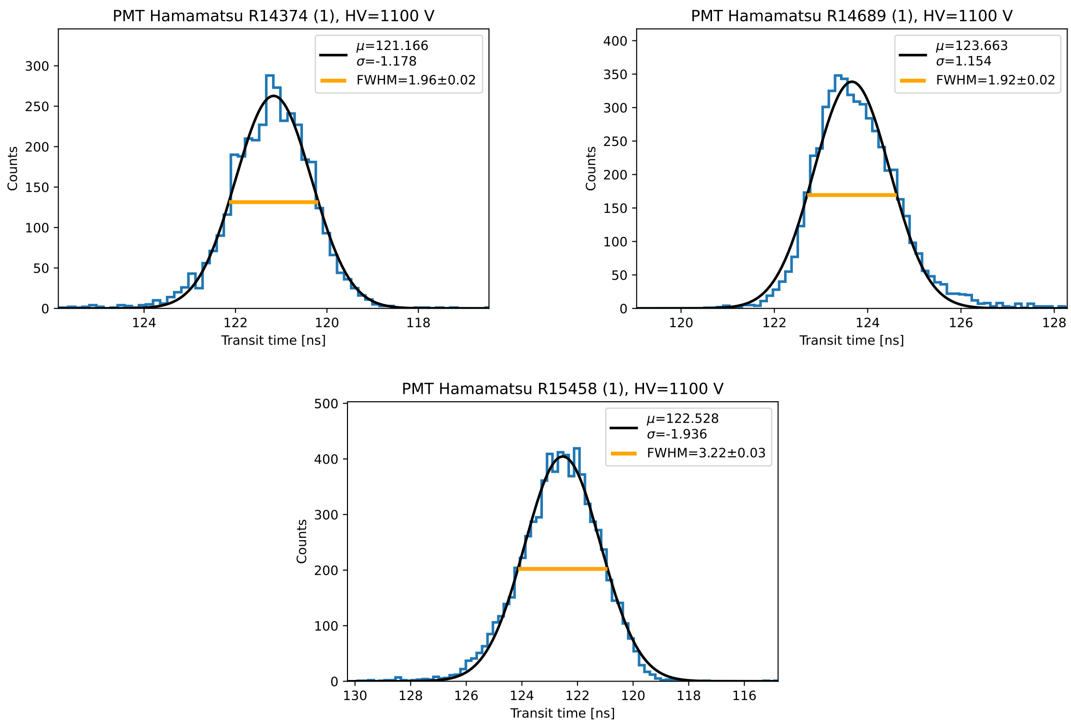

Figure 5.10: Transit time histograms at HV=1100 V with gaussian fit curve of one of each tested Hamamatsu PMT. The FWHM of the fit is the PMT's TTS in ns.

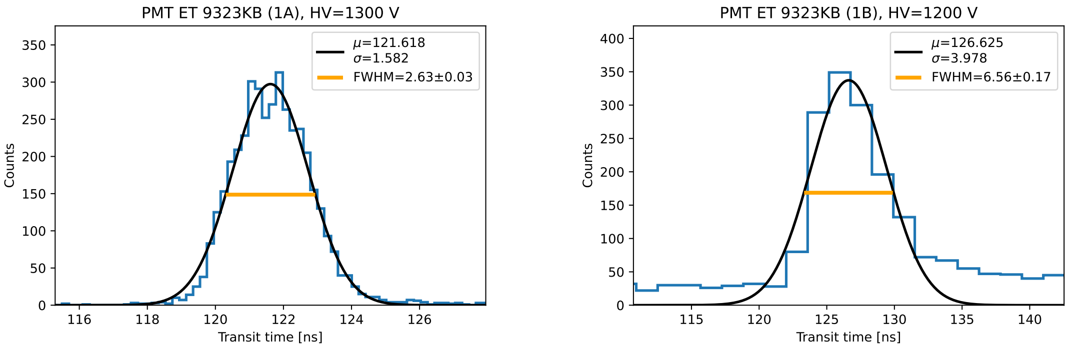

Figure 5.11: Transit time histograms at HV=1300 V/1200 V with gaussian fit curve of one ET PMT with bases A and B. The FWHM of the fit is the PMT's TTS in ns.

Company	PMT type	HV [V]	TTS [ns]
Hamamatsu	R14374 (1)	1100	1.96 ± 0.02
	R14374 (2)	1100	1.90 ± 0.01
	R14689 (1)	1100	1.92 ± 0.02
	R14689 (2)	1100	2.04 ± 0.01
	R15458 (1)	1100	3.22 ± 0.03
	R15458 (2)	1100	3.01 ± 0.03
ET Enterprises	9323KB (1A)	1300	2.63 ± 0.03
	9323KB (2A)	1300	2.96 ± 0.03
	9323KB (1B)	1200	6.56 ± 0.17
	9323KB (2B)		n/a

Table 5.7: Calculated TTS values from fit curve of transit time histograms for all tested PMTs at HV=1100 V.

The TTS values for the Hamamatsu types R14374 and R14689 are around 2 ns, which allows a good time resolution. The R15458 and the ET PMTs (base A) have values around 3 ns, which is still below the maximum required TTS (table 4.1). The base B measurement with the ET PMTs show relatively large TTS values.

5.4.5 Photocathode Scan

A performance scan of the whole photocathode can be done by rotating the tube while shooting laser pulses at it and comparing the differences of the respective responses. Due to the shape of the photocathode, the arrival of a photon from a certain angle can influence the transit time and the collection efficiency. This measurement can be done with the OMCU setup and will be conducted as one of the next evaluation steps.

5.4.6 Quantum Efficiency

To determine the quantum efficiency, a light source of different wavelengths is needed. This can be achieved by using various monochromatic light sources of different wavelengths, or a multi-wavelength light source and a monochromator. To do this measurement with the OMCU setup, the laser needs to be exchanged by such a light source. The photodiode connected to the picoammeter serves as a reference measurement of the light output. The QE is calculated as the ratio between the PMT's and the diode's photocurrent for different wavelengths.

Chapter 6

Summary and Conclusion

At the beginning of this thesis, the basics of astroparticle physics have been explained, leading to a more detailed discussion of the physics of neutrinos and their detection principle. Further, the current state of the development of P-ONE, a future neutrino telescope, and the first installation in the form of P-ONE-1 have been presented. After a comprehensive description of photomultiplier tubes, possible candidates for the P-ONE optical modules were presented. These include three tubes from Hamamatsu: R14374, R14689, and R15458, the 9323KB from ET Enterprises, and one from a third supplier, but these results could not be published in the scope of this thesis. The measurements with the ET PMTs were performed with two different bases with varying voltage divisions.

The developed setup for PMT testing and characterisation was introduced. The different setup components were displayed, focusing on the developed code to operate them. Finally, performed measurements with the PMTs were presented and evaluated.

The measured dark rates are relatively high. The reasons for that were determined to be a too short waiting period of 30 minutes before taking the data. Further, the time interval of taking the data would need to be substantially longer to increase statistics. However, hardware limitations of the picoscope buffer reduced the maximum number of waveforms to 10^5. A triggered system needs to be implemented to measure the dark rate for a longer period.

The measurements with an attenuated laser pulse as a light source showed that the Hamamatsu PMTs have higher gains in comparison to the other candidates. A high gain is essential for detecting the light signal induced by neutrinos but can effectively be corrected by the applied high voltage. On further notice, one base from ET Enterprises showed significantly better results than the other.

The Hamamatsu R14374 and R14689 have TTS values around 2 ns, which tendentially allow a good time resolution of the detector and can be used as input for further development of the DAQ system.

For the further evaluation of the PMTs, additional next steps are planned. The photocathode scan measurements using the rotation station will be performed and analysed. To measure the quantum efficiency, a different light source will be implemented, and a light-shielding housing for the photodiode and the second laser output will be constructed to reduce systematics induced by scattering and reflection effects.

The OMCU setup will also be used for the evaluation of the gel pads for the optical module. There, the effectiveness of different gel pad geometries and other reflector types can be studied by comparing measurements with and without a gel pad attached to the PMT. Additionally, refractional behaviour of a mounted system, consisting of PMTs and gel pads mounted in a glass hemisphere can be studied with the setup by adjusting the laser direction via, e.g., a system of mirrors mounted on the rotational stages.

Furthermore, the OMCU setup will be used for the development of a suitable HV base. The photomultipliers inside the multi-PMT-modules need to be supplied with high voltages. A suitable base, which can provide HV for the individual PMTs and which can be connected to the internal DAQ electronics and mounting, will be designed.

Finally, the influence of the metal springs, intended to be used as part of the click-in mounting mechanism, will be studied. The material could generate unwanted noise or a reduced PDE by the accumulation of electrons in the metal due to the applied negative HV. Also, the influence of magnetic fields on the PMTs and the possible use of a shielding mesh has to be investigated.

When designing, testing, and calibrating the optical modules for P-ONE-1, the OMCU setup will need to be adjusted in a way that the glass (hemi-)spheres can be mounted inside the dark box, and that all PMTs can be supplied with HV. The response of the different PMTs in one optical module to a small light signal from one side can be studied, also the use of an isotropising sphere as used in the calibration modules can be considered to perform angular measurements of the individually mounted PMTs.

Finally, the influence of the light emitters in the calibration module on the PMTs and potential ageing effects or other disturbances have to be investigated.

In conclusion, the setup, that was developed in the scope of this thesis, is a valuable tool for the research and development phase of the optical and calibration modules for P-ONE-1. It works on a "plug and play" principle and thus enables an easy and efficient way of performing tests.

Chapter 7

Outlook

At the current state of the development of the P-ONE prototype line, the hybrid backbone cable, module termination and designs, and the deployment strategy are in full progress. In addition to the knowledge gained from the pathfinder missions and ONC's experience, the lessons learned from IceCube, ANTARES, KM3NeT, and Baikal-GVD are being integrated. After the deployment of P-ONE-1, P-ONE shall be successively extended, allowing potential reconstruction with a minimal number of three moored observatories.
However, with the size in the order of a cubic kilometre, the neutrino samples collected from the cosmos are limited. P-ONE will contribute to a global effort to establish more statistics and exposure to the entire sky, in complement to already existing neutrino telescopes. This can pave the way for fundamental discoveries in astro and particle physics, otherwise not possible with a single detector [66, 67]. Using a combined neutrino telescope network distributed around the globe is beneficial for the all-time exposure. While IceCube's best sensitivity is at the horizon, telescopes in the northern hemisphere have changing optimal detection regions due to the Earth's rotation. Like that, a large region of the Universe is covered by at least one telescope at all times [44]. A map of the existing and the under construction neutrino telescopes is depicted in fig. 7.1.

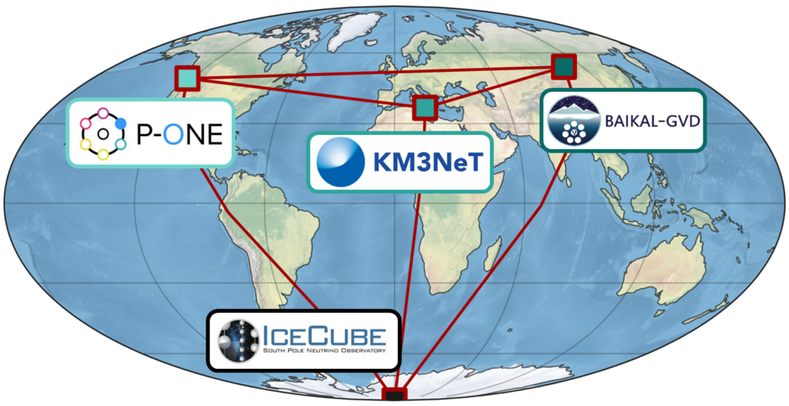

Figure 7.1: Map of existing or under construction neutrino telescopes. Figure taken from [66].

A Appendix

A.1 Optical Module Calibration Unit Code

Picoscope The *Picoscope* class uses elements of the code examples on the *PicoTech* Github page [62]. The examples helped to understand the working principle and the programming of the picoscope.

Code A.1: Code cut-out of OMCU Picoscope.py

```
import ctypes
import numpy as np
from numpy import trapz
from picosdk.ps6000a import ps6000a as ps
from picosdk.PicoDeviceEnums import picoEnum as enums
import matplotlib.pyplot as plt
from picosdk.functions import adc2mV
import time


class Picoscope:
    """
    This is a class for the PicoTech Picoscope 6424E
    """

    def __init__(self):
        self.chandle = ctypes.c_int16()
        self.resolution = enums.PICO_DEVICE_RESOLUTION["PICO_DR_12BIT"]
        ps.ps6000aOpenUnit(ctypes.byref(self.chandle), None,
            self.resolution) # opens connection

        # CHANNEL SETUP
        self.coupling_sgnl = enums.PICO_COUPLING["PICO_DC_50OHM"]
        self.coupling_trg = enums.PICO_COUPLING["PICO_DC"]
```

```
        self.voltrange_sgnl = 3 # 3=PICO_100MV: pm 100 mV
        self.voltrange_trg = 9 # 9=PICO_10V: pm 10 V
        self.bandwidth = enums.PICO_BANDWIDTH_LIMITER["PICO_BW_FULL"]
        self.noOfPreTriggerSamples = 100
        self.noOfPostTriggerSamples = 250
        self.nSamples = self.noOfPreTriggerSamples +
            self.noOfPostTriggerSamples

    def channel_setup(self, trgchannel=0, sgnlchannel=2):
        """
        This is a function to set a trigger channel and a signal channel
            on and the others off.
        :param trgchannel: int: 0=A, 1=B, 2=C, 3=D, default: 0
        :param sgnlchannel: int: 0=A, 1=B, 2=C, 3=D, default: 2
        :return: trgchannel, sgnlchannel: int (0, 1, 2, 3)
        """
        # channel setup

        # handle = chandle
        # channel = channel
        # coupling = self.coupling_trg/sgnl
        # channelRange = self.voltrange_trg/sgnl
        # analogueOffset = 0 V
        # bandwidth = self.bandwidth

        ps.ps6000aSetChannelOn(self.chandle, trgchannel,
            self.coupling_trg, self.voltrange_trg, 0, self.bandwidth)
        ps.ps6000aSetChannelOn(self.chandle, sgnlchannel,
            self.coupling_sgnl, self.voltrange_sgnl, 0, self.bandwidth)

        for ch in [0, 1, 2, 3]:
            if trgchannel == ch or sgnlchannel == ch:
                pass
            else:
                ps.ps6000aSetChannelOff(self.chandle, ch)
                #print("Channel off:", ch)

        return trgchannel, sgnlchannel
```

```
def trigger_setup(self, trgchannel=0, direction=2, threshold=1000):
    """
    This is a function to set the trigger on the given channel. The
        threshold can be given in [mV].
    :param trgchannel: int: 0=A, 1=B, 2=C, 3=D, default: 0
    :param direction: int, default: 2 (rising edge)
    PICO_ABOVE = PICO_INSIDE = 0, PICO_BELOW = PICO_OUTSIDE = 1,
        PICO_RISING = PICO_ENTER = PICO_NONE = 2,
    PICO_FALLING = PICO_EXIT = 3, PICO_RISING_OR_FALLING =
        PICO_ENTER_OR_EXIT = 4
    :param threshold: int [mV] trigger value, default value: 1000 mV
    :return: channel (int), direction (int), threshold(int) [mV]
    """
    # Set simple trigger on the given channel, [thresh] mV rising with
        1 ms autotrigger
    # handle = chandle
    # enable = 1
    # source = channel
    # threshold = threshold [mV], default value: 1000 mV
    # direction = 2 (rising)
    # delay = 0 s
    autoTriggerMicroSeconds = 1000000 # [us]
    ps.ps6000aSetSimpleTrigger(self.chandle, 1, trgchannel, threshold,
        direction, 0, autoTriggerMicroSeconds)
    return trgchannel, direction, threshold

def timebase_setup(self):
    """
    This is a function to get the fastest available timebase.
    The timebases allow slow sampling in block mode to overlap the
        streaming sample intervals.
    :return: timebase: int
    """
    # Get fastest available timebase
    # handle = chandle
    enabledChannelFlags =
        enums.PICO_CHANNEL_FLAGS["PICO_CHANNEL_A_FLAGS"]
    # PICO_CHANNEL_A_FLAGS = 1, PICO_CHANNEL_B_FLAGS = 2,
        PICO_CHANNEL_C_FLAGS = 4, PICO_CHANNEL_D_FLAGS = 8
```

```
        timebase = ctypes.c_uint32(0)
        timeInterval = ctypes.c_double(0)
        # resolution = resolution
        ps.ps6000aGetMinimumTimebaseStateless(self.chandle,
            enabledChannelFlags, ctypes.byref(timebase),
                                               ctypes.byref(timeInterval),
                                                   self.resolution)
        #print("timebase = ", timebase.value)
        #print("sample interval =", timeInterval.value, "s")
        return timebase.value, timeInterval.value

    def buffer_setup_block_multi(self, trgchannel=0, sgnlchannel=2,
        number=10):
        """
        This function tells the driver to store the data unprocessed: raw
            mode (no downsampling).
        One trigger channel and one signal channel, several waveforms -
            indicated by number
        :param trgchannel: int: 0=A, 1=B, 2=C, 3=D, default: 0
        :param sgnlchannel: int: 0=A, 1=B, 2=C, 3=D, default: 2
        :param number: int (number of waveforms)
        :return: buffersMax_trgch, buffersMin_trgch, buffersMax_sgnlch,
            buffersMin_sgnlch
                format: ((ctypes.c_int16 * nSamples) * number)()
        """

        # Set number of samples to be collected
        nSamples = self.nSamples

        # Create buffers
        buffersMax_trgch = ((ctypes.c_int16 * nSamples) * number)()
        buffersMin_trgch = ((ctypes.c_int16 * nSamples) * number)()
        buffersMax_sgnlch = ((ctypes.c_int16 * nSamples) * number)()
        buffersMin_sgnlch = ((ctypes.c_int16 * nSamples) * number)()

        # Set data buffers
        # handle = chandle
        # channel = channel
        # bufferMax = bufferMax
```

```
        # bufferMin = bufferMin
        # nSamples = nSamples
        dataType = enums.PICO_DATA_TYPE["PICO_INT16_T"]
        downSampleMode = enums.PICO_RATIO_MODE["PICO_RATIO_MODE_RAW"]
        clear = enums.PICO_ACTION["PICO_CLEAR_ALL"]
        add = enums.PICO_ACTION["PICO_ADD"]
        action = clear|add # PICO_ACTION["PICO_CLEAR_WAVEFORM_CLEAR_ALL"]
            | PICO_ACTION["PICO_ADD"]

        for i in range(0, number):
            waveform = i
            if i == 0:
                ps.ps6000aSetDataBuffers(self.chandle, trgchannel,
                    ctypes.byref(buffersMax_trgch[i]),
                                        ctypes.byref(buffersMin_trgch[i]),
                                            nSamples, dataType, waveform,
                                        downSampleMode, action)
                ps.ps6000aSetDataBuffers(self.chandle, sgnlchannel,
                    ctypes.byref(buffersMax_sgnlch[i]),
                                        ctypes.byref(buffersMin_sgnlch[i]),
                                            nSamples, dataType, waveform,
                                        downSampleMode, add)
            if i > 0:
                ps.ps6000aSetDataBuffers(self.chandle, trgchannel,
                    ctypes.byref(buffersMax_trgch[i]),
                                        ctypes.byref(buffersMin_trgch[i]),
                                            nSamples, dataType, waveform,
                                        downSampleMode, add)
                ps.ps6000aSetDataBuffers(self.chandle, sgnlchannel,
                    ctypes.byref(buffersMax_sgnlch[i]),
                                        ctypes.byref(buffersMin_sgnlch[i]),
                                            nSamples, dataType, waveform,
                                        downSampleMode, add)

        return buffersMax_trgch, buffersMin_trgch, buffersMax_sgnlch,
            buffersMin_sgnlch

    def block_measurement(self, trgchannel=0, sgnlchannel=2, direction=2,
        threshold=1000, number=10):
```

```
"""
This is a function to run a block measurement. Several waveforms
    are stored. The number is indicated with the
parameter number.
First, it runs channel_setup(channel) to set a channel on and the
    others off.
Then, it runs trigger_setup(trgchannel, direction, threshold),
    which sets the trigger to a rising edge at the
given value [mV].
Then, it runs timebase_setup() to get the fastest available
    timebase.
Then, it runs buffer_multi_setup(bufchannel, number) to setup the
    buffer
to store the data unprocessed.
:param trgchannel: int: 0=A, 1=B, 2=C, 3=D, default: 0
:param sgnlchannel: int: 0=A, 1=B, 2=C, 3=D, default: 2
:param direction: int, default: 2 (rising)
PICO_ABOVE = PICO_INSIDE = 0, PICO_BELOW = PICO_OUTSIDE = 1,
    PICO_RISING = PICO_ENTER = PICO_NONE = 2,
PICO_FALLING = PICO_EXIT = 3, PICO_RISING_OR_FALLING =
    PICO_ENTER_OR_EXIT = 4
:param threshold: int [mV] trigger value, default value: 1000 mV
:param number: int (number of waveforms)
:return: data_sgnl, data_trg
"""
self.channel_setup(trgchannel, sgnlchannel)
# self.channel_setup_all()

# Set number of memory segments
maxSegments = ctypes.c_uint64(number)
ps.ps6000aMemorySegments(self.chandle, number,
    ctypes.byref(maxSegments))

# Set number of captures
ps.ps6000aSetNoOfCaptures(self.chandle, number)

timebase, timeInterval = self.timebase_setup()

self.trigger_setup(trgchannel, direction, threshold)
```

```
buffersMax_trgch, buffersMin_trgch, buffersMax_sgnlch,
    buffersMin_sgnlch =\
    self.buffer_setup_block_multi(trgchannel=trgchannel,
        sgnlchannel=sgnlchannel, number=number)

nSamples = self.nSamples

# Run block capture
# handle = chandle
# timebase = timebase
timeIndisposedMs = ctypes.c_double(0)
# segmentIndex = 0
# lpReady = None Using IsReady rather than a callback
# pParameter = None

t1 = time.time()
ps.ps6000aRunBlock(self.chandle, self.noOfPreTriggerSamples,
    self.noOfPostTriggerSamples, timebase,
                    ctypes.byref(timeIndisposedMs), 0, None, None)
t2 = time.time()
deltaT = t2-t1

# Check for data collection to finish using ps6000aIsReady
ready = ctypes.c_int16(0)
check = ctypes.c_int16(0)
while ready.value == check.value:
    ps.ps6000aIsReady(self.chandle, ctypes.byref(ready))

# Get data from scope
# handle = chandle
# startIndex = 0
noOfSamples = ctypes.c_uint64(nSamples)
# segmentIndex = 0
end = number-1
# downSampleRatio = 1
downSampleMode = enums.PICO_RATIO_MODE["PICO_RATIO_MODE_RAW"]
# Creates an overflow location for each segment
overflow = (ctypes.c_int16 * number)()
```

```
ps.ps6000aGetValuesBulk(self.chandle, 0,
    ctypes.byref(noOfSamples), 0, end, 1, downSampleMode,
                                        ctypes.byref(overflow))

# get max ADC value
# handle = chandle
minADC = ctypes.c_int16()
maxADC = ctypes.c_int16()
ps.ps6000aGetAdcLimits(self.chandle, self.resolution,
    ctypes.byref(minADC), ctypes.byref(maxADC))

self.stop_scope()

# convert ADC counts data to mV
adc2mVMax_trgch_list = np.zeros((number, nSamples))
for i, buffers in enumerate(buffersMax_trgch):
    adc2mVMax_trgch_list[i] = adc2mV(buffers, self.voltrange_trg,
        maxADC)

adc2mVMax_sgnlch_list = np.zeros((number, nSamples))
for i, buffers in enumerate(buffersMax_sgnlch):
    adc2mVMax_sgnlch_list[i] = adc2mV(buffers,
        self.voltrange_sgnl, maxADC)

# Create time data
timevals = np.linspace(0, nSamples * timeInterval * 1000000000,
    nSamples)

# create array of data and save as npy file
data_sgnl = np.zeros((number, nSamples, 2))
data_sgnl[:, :, 0] = timevals
data_sgnl[:, :, 1] = adc2mVMax_sgnlch_list

data_trg = np.zeros((number, nSamples, 2))
data_trg[:, :, 0] = timevals
data_trg[:, :, 1] = adc2mVMax_trgch_list

return data_sgnl, data_trg # filename_sgnl, filename_trg
```

```
    def stop_scope(self):
        """
        This is a function to stop whatever the picoscope is doing.
        """
        ps.ps6000aStop(self.chandle)

    def close_scope(self):
        """
        This function stops whatever the picoscope is doing and closes its
            connection.
        """
        ps.ps6000aStop(self.chandle)
        ps.ps6000aCloseUnit(self.chandle)
```

Laser The pulsed picosecond laser used in OMCU is operated via a control unit. The laser control device comes with implemented commands that are used in the *Laser* class.

Code A.2: Code cut-out of OMCU Laser.py

```
import logging
import serial
import time

class Laser:
    """
    This is a class for the Picosecond Laser System Controller EIG2000DX.
    """

    def __init__(self, dev="/dev/Laser_control", simulating=False,
        delay=.1):
        self.logger = logging.getLogger(type(self).__name__)

        self.off_pulsed() # pulsed laser emission OFF
        self.set_trig_edge(1) # trigger edge: rising
        self.set_trig_source(0) # trigger source: internal
        self.set_trig_level(0) # trigger level: 0 mV
        self.set_tune_value(710) # tune value at 71%
```

```
        self.set_freq(10e3) # frequency = 10 kHZ
        self.off_cw() # CW laser emission OFF

    def __write_serial(self, cmd, delay=None, line_ending=b'\r\n'):
        """
        PARAMETERS
        ----------
        cmd: Str, bytes, optional
        delay: float or None, optional
        line_ending: bytes, optional
        """
        if delay is None:
            delay = self.delay

        if type(cmd) is str:
            cmd = cmd.encode()

        if not cmd.endswith(line_ending):
            cmd += line_ending

        self.serial.write(cmd)
        time.sleep(delay)

        return_str = self.serial.readline().decode()

        self.logger.debug(f'Serial write cmd: {cmd}; return {return_str}')
        return return_str

    def on_pulsed(self):
        """
        This function enables the pulsed laser emission (laser on)
        :return: int: 0 = emission off, 1 = emission on, (2 = something
            went wrong)
        """
        self.__write_serial('ld=1') # enables pulsed laser emission
        return self.get_ld()

            def off_pulsed(self):
        """
```

```
        This function disables the pulsed laser emission (laser off)
        :return: int: 0 = emission off, 1 = emission on, (2 = something
            went wrong)
        """
        self.__write_serial('ld=0') # disables pulsed laser emission
        return self.get_ld()

    def get_ld(self):
        """
        This is a function to get information about the pulsed laser
            emission state
        :return: int: 0 = emission off, 1 = emission on, (2 = something
            went wrong)
        """
        ld_string = self.__write_serial('ld?') # returns string 'pulsed
            laser emission: off/on'
        print(ld_string)
        if 'off' in ld_string:
            ld_val = 0
        elif ' on' in ld_string:
            ld_val = 1
        elif 'test' in ld_string:
            ld_val = 0
        else:
            ld_val = 2
            print('Error: pulsed laser emission state could not be
                determined. Try again!')
        return ld_val
```

Power Supply For the power supply units, the existing Python class *gpd3303s* was used. The *PSU* class defines a setting function for voltage and current by channel, and an on-/ off-function.

Code A.3: Code cut-out of OMCU PSU.py

```
import gpd3303s
import time

class PSU(gpd3303s.GPD3303S):
```

```python
    """
    This class makes an instance for the USB power supply.
    The udev rules must allow access to the current user.
    """

    def __init__(self, dev="/dev/PSU_1"): # PSU_0 or PSU_1
        """
        This is the init function for the power supply device
        :param dev: device path, use: dev="/dev/PSU_0" or dev="/dev/PSU_1"
        """
        super().__init__()
        self.state = False
        self.open(dev)
        self.enableOutput(False)
        self.setCurrent(1, 3.0)
        self.setCurrent(2, .1)
        self.setVoltage(1, 12.0)
        self.setVoltage(2, 3.6)

    def settings(self, channel, voltage=5.0, current=0.1):
        """
        This is a function set voltage and current for the desired channel
        :param channel: int (1/2)
        :param voltage: float, default 5.0 V
        :param current: float, default 0.1 A
        :return: boolean (state)
        """
        self.setVoltage(channel, voltage)
        self.setCurrent(channel, current)
        return self.state

    def on(self):
        self.enableOutput(True)
        self.state = True
        time.sleep(1)

    def off(self):
        self.enableOutput(False)
        self.state = False
```

A.2 Measurement Plots

A.2.1 Average Waveforms

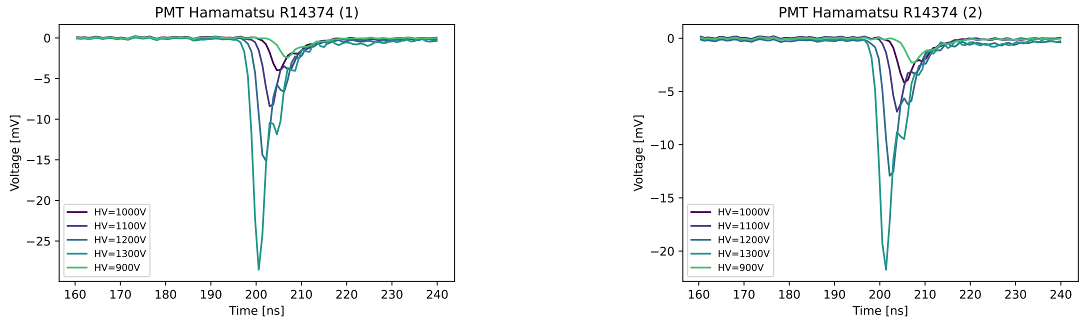

Figure A.1: Average waveforms of the single photoelectron signal for the Hamamatsu R14374 PMTs.

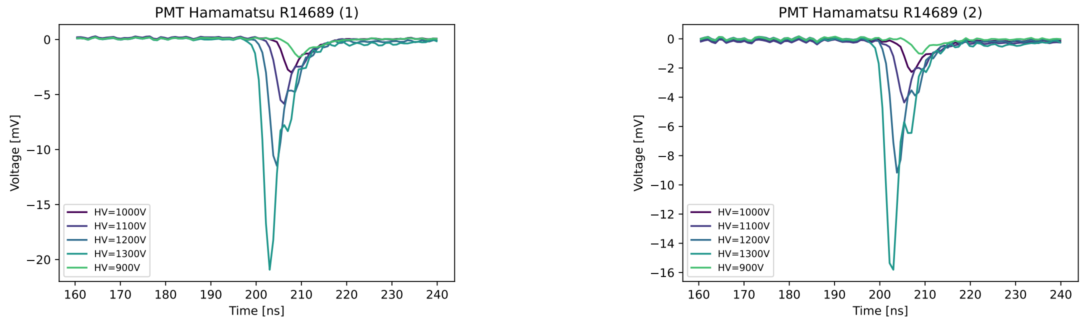

Figure A.2: Average waveforms of the single photoelectron signal for the Hamamatsu R14689 PMTs.

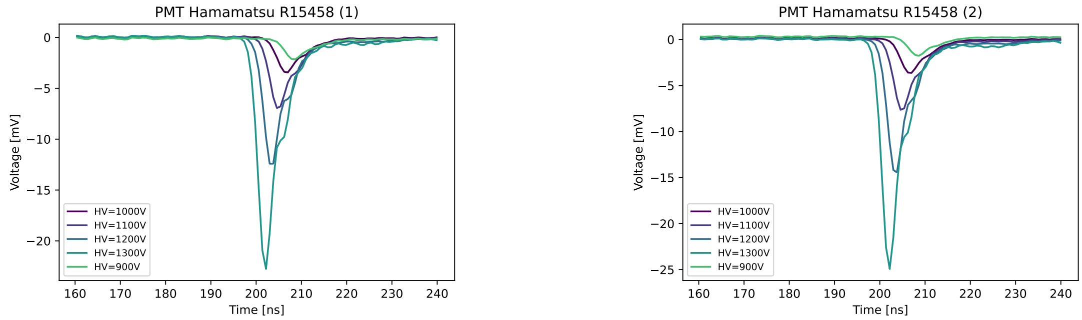

Figure A.3: Average waveforms of the single photoelectron signal for the Hamamatsu R15458 PMTs.

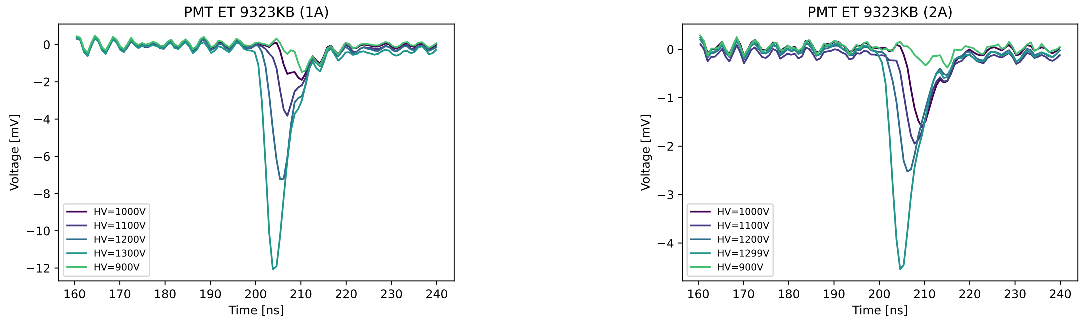

Figure A.4: Average waveforms of the single photoelectron signal for the ET Enterprises 9323KB PMTs, base A.

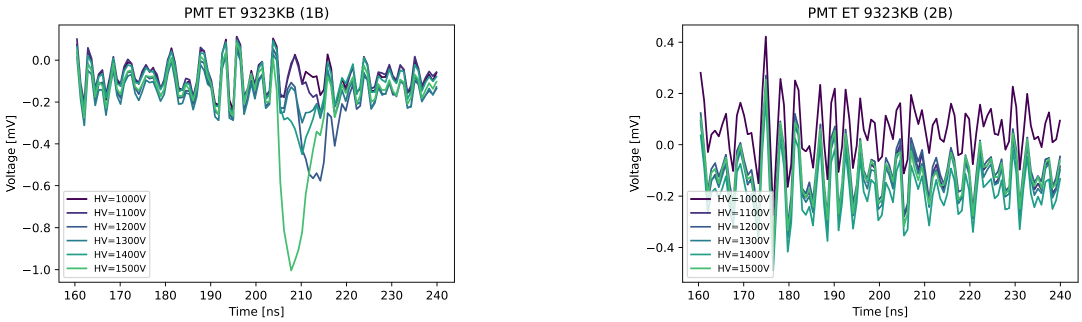

Figure A.5: Average waveforms of the single photoelectron signal for the ET Enterprises 9323KB PMTs, base B.

A.2.2 Charge-Gain Histograms

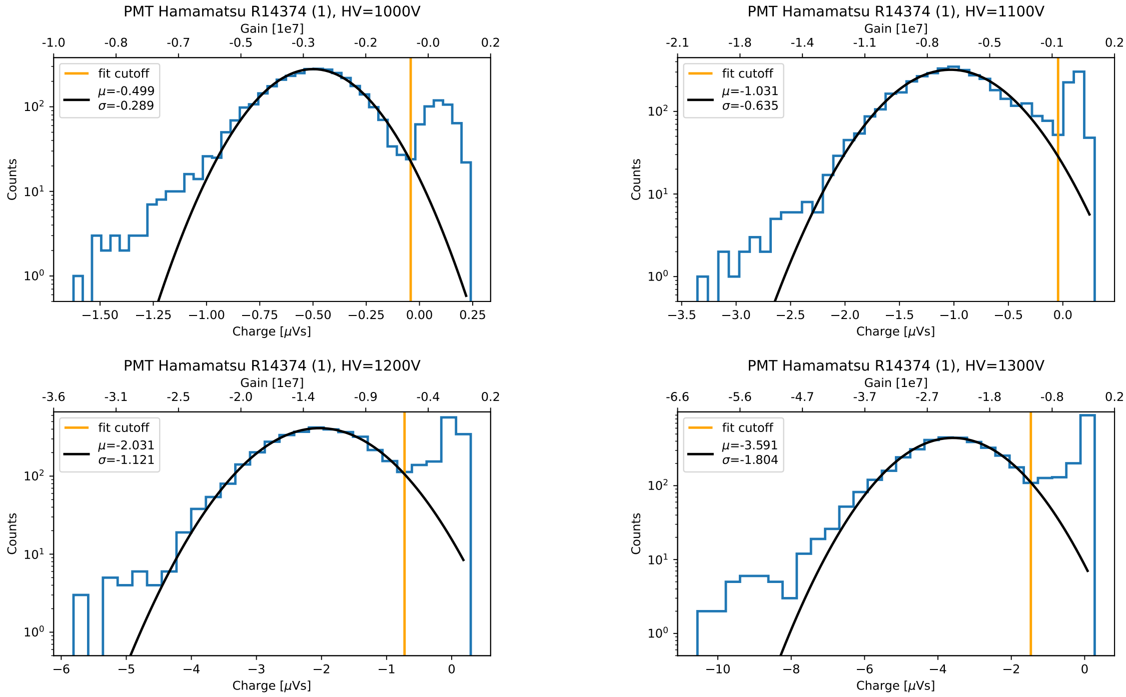

Figure A.6: Charge/gain histograms with fit for the Hamamatsu R14374 (1) PMT.

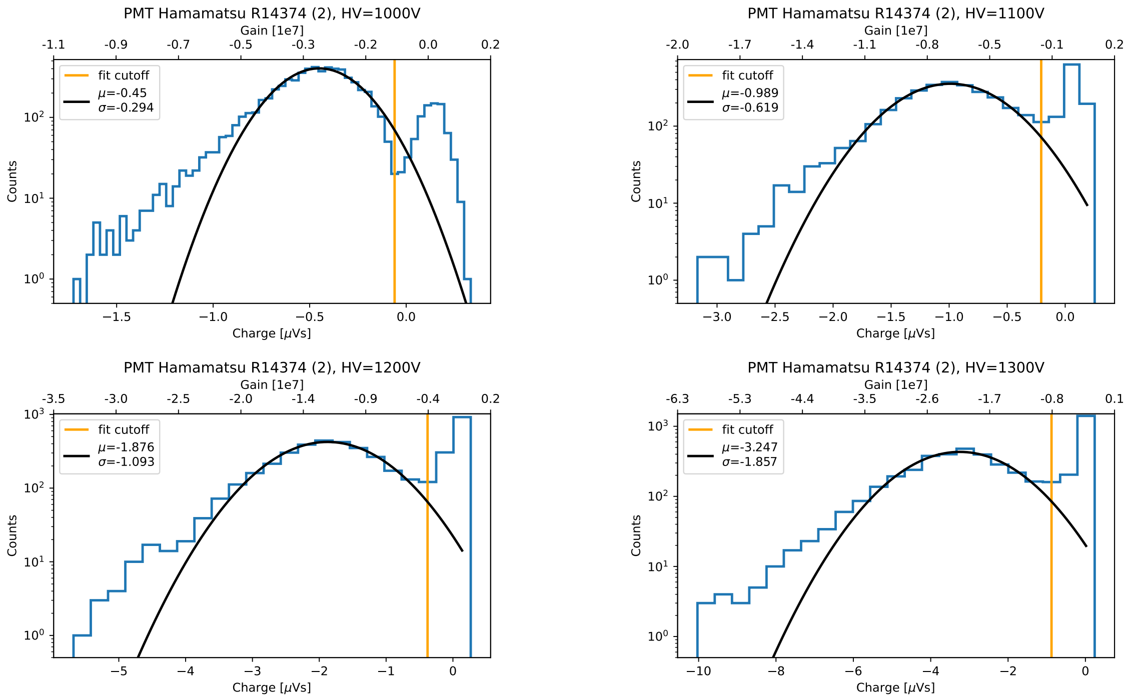

Figure A.7: Charge/gain histograms with fit for the Hamamatsu R14374 (2) PMT.

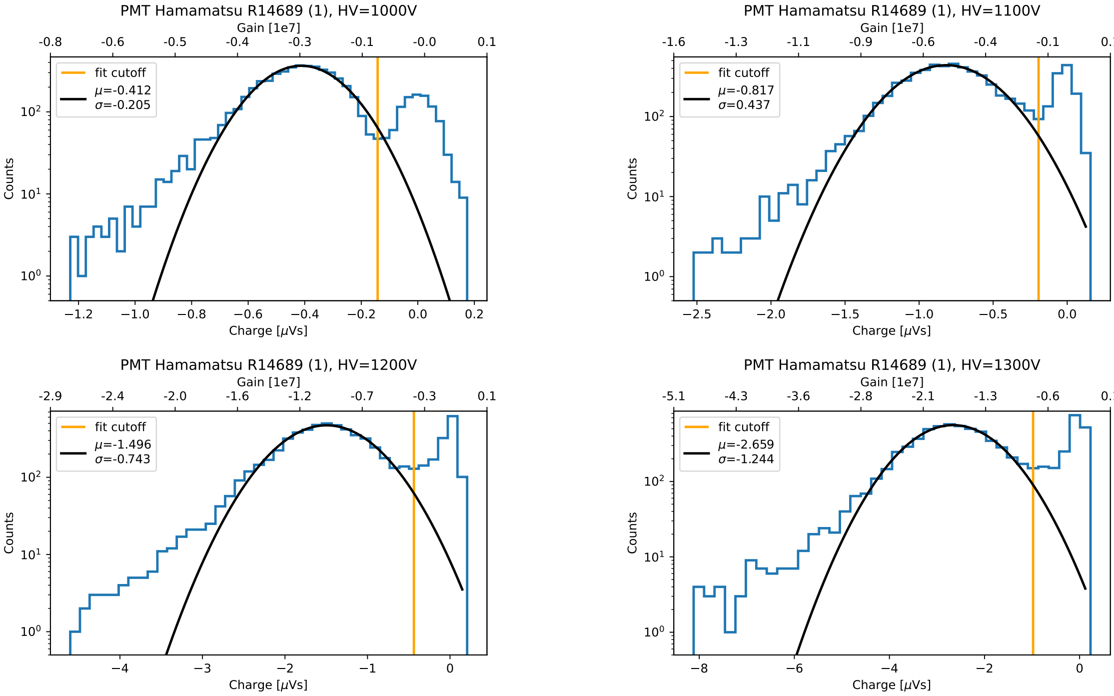

Figure A.8: Charge/gain histograms with fit for the Hamamatsu R14689 (1) PMT.

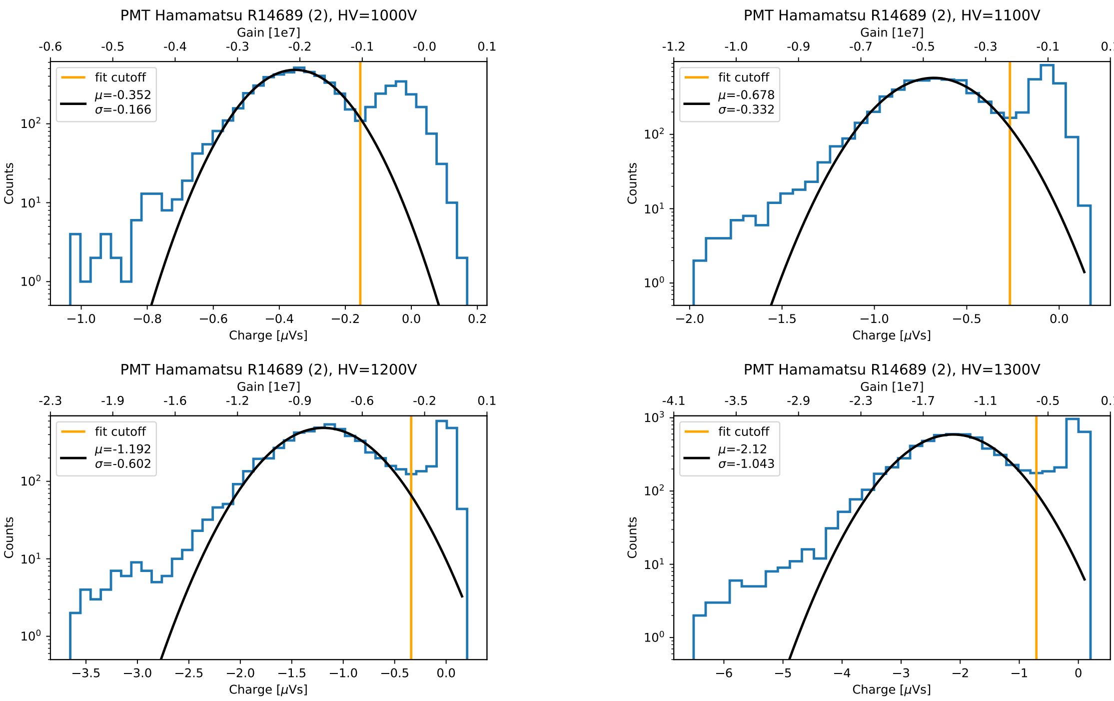

Figure A.9: Charge/gain histograms with fit for the Hamamatsu R14689 (2) PMT.

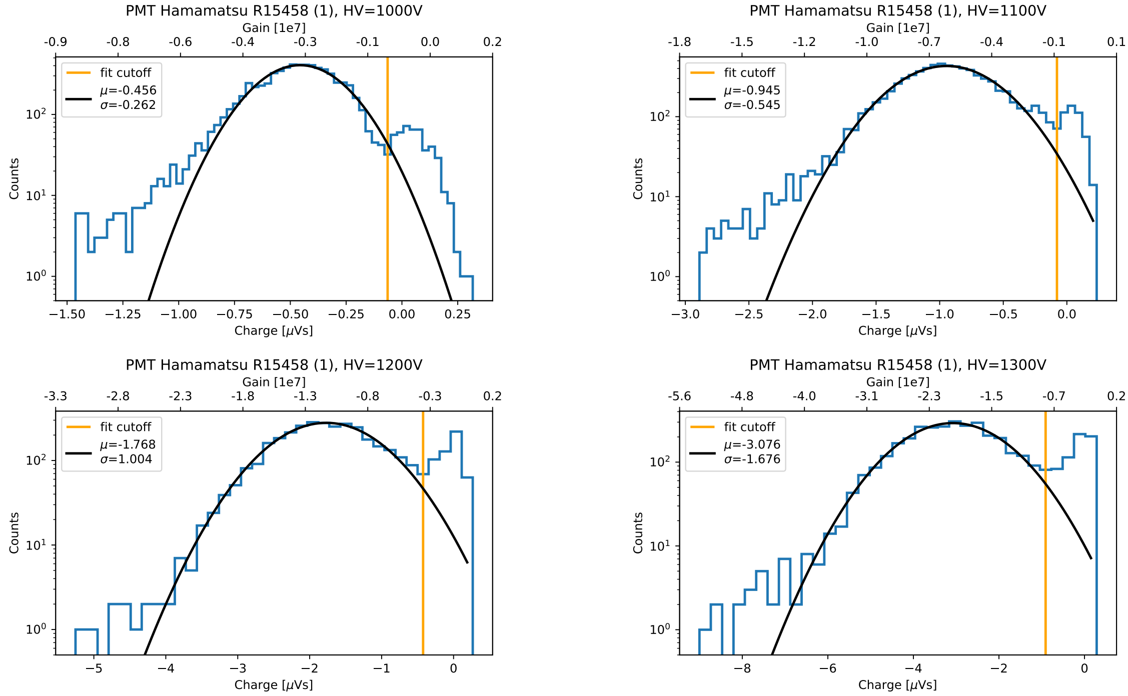

Figure A.10: Charge/gain histograms with fit for the Hamamatsu R15458 (1) PMT.

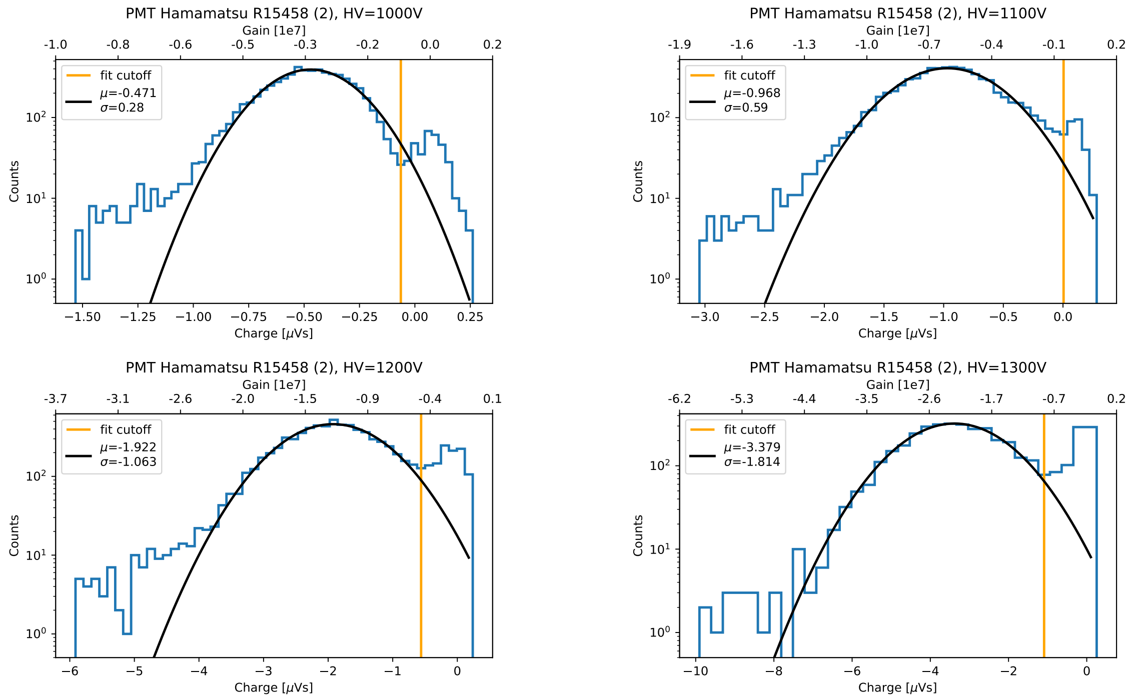

Figure A.11: Charge/gain histograms with fit for the Hamamatsu R15458 (2) PMT.

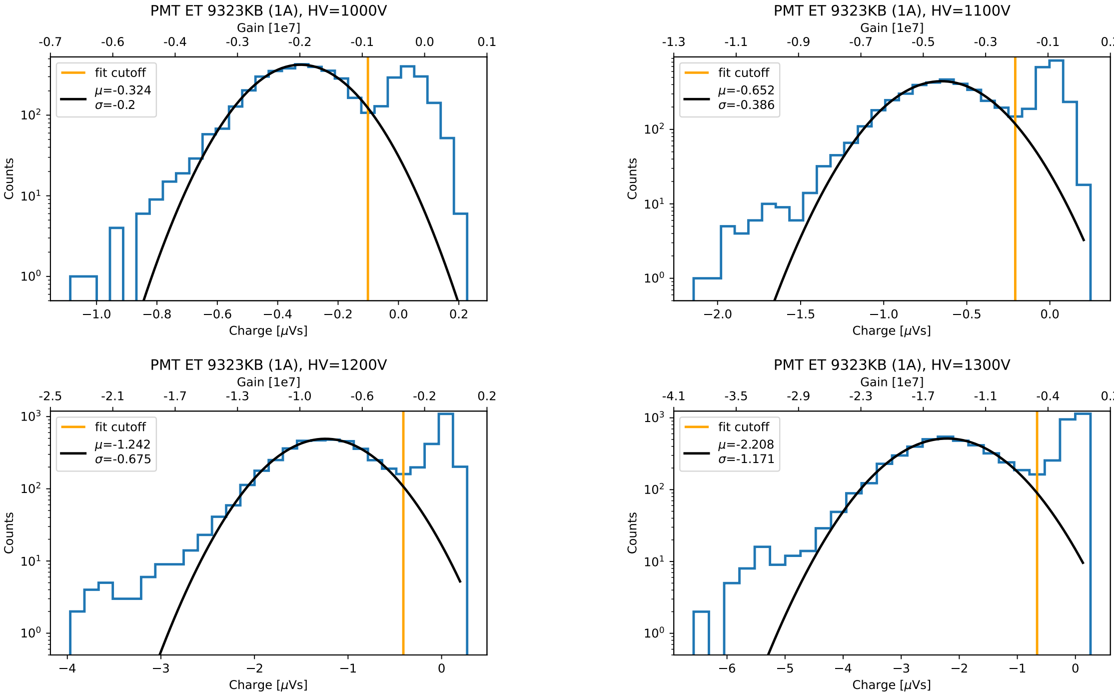

Figure A.12: Charge/gain histograms with fit for the ET 9323KB (1) PMT, base A.

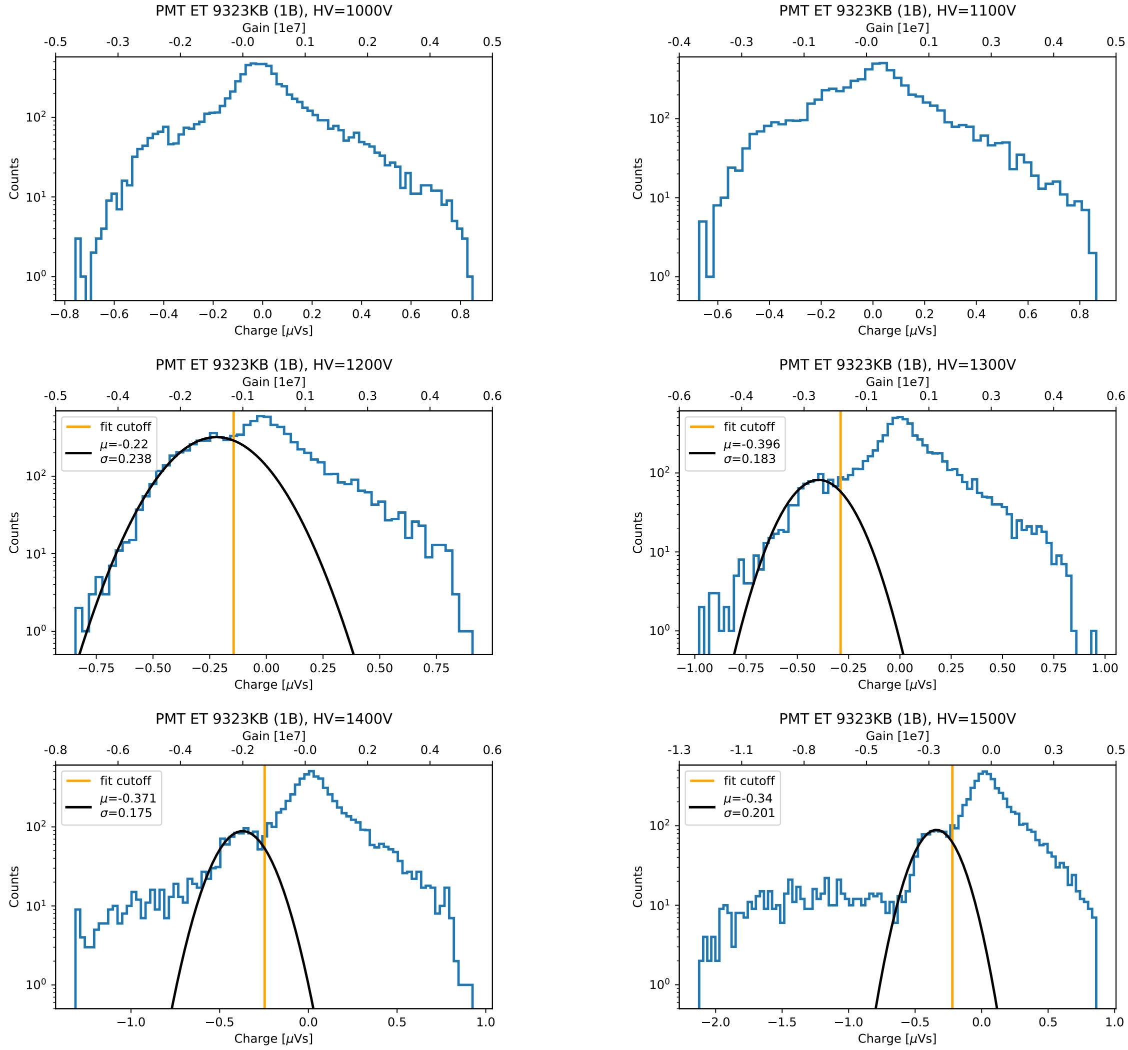

Figure A.13: Charge/gain histograms for the ET 9323KB (1) PMT, base B.

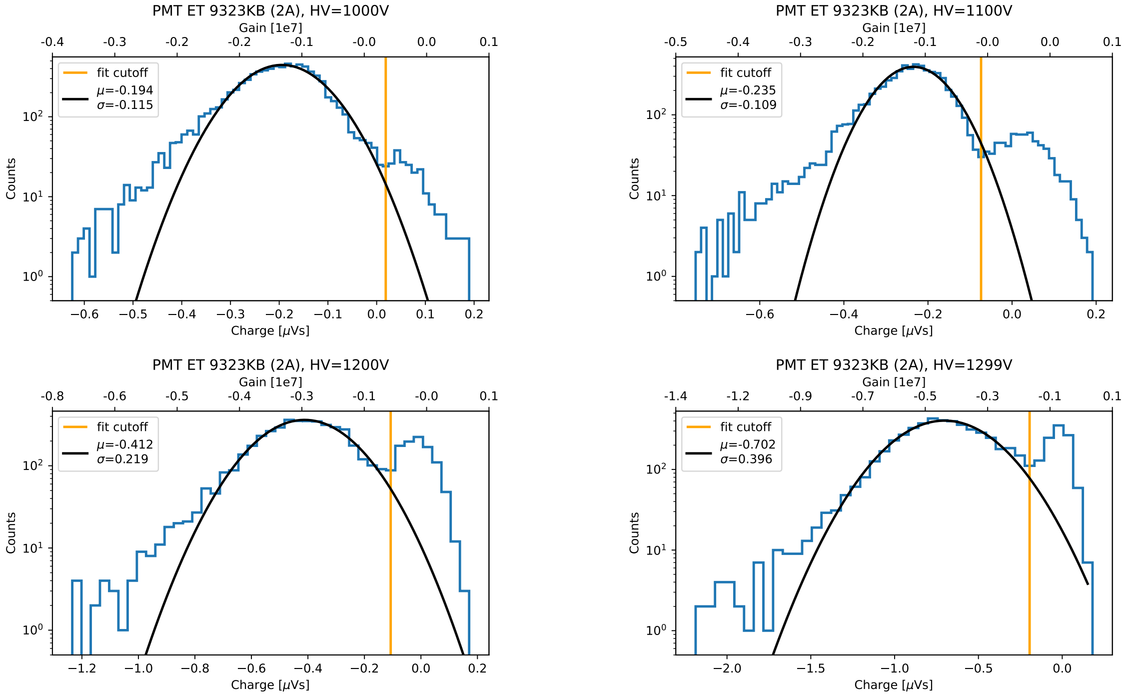

Figure A.14: Charge/gain histograms with fit for the ET 9323KB (2) PMT, base A.

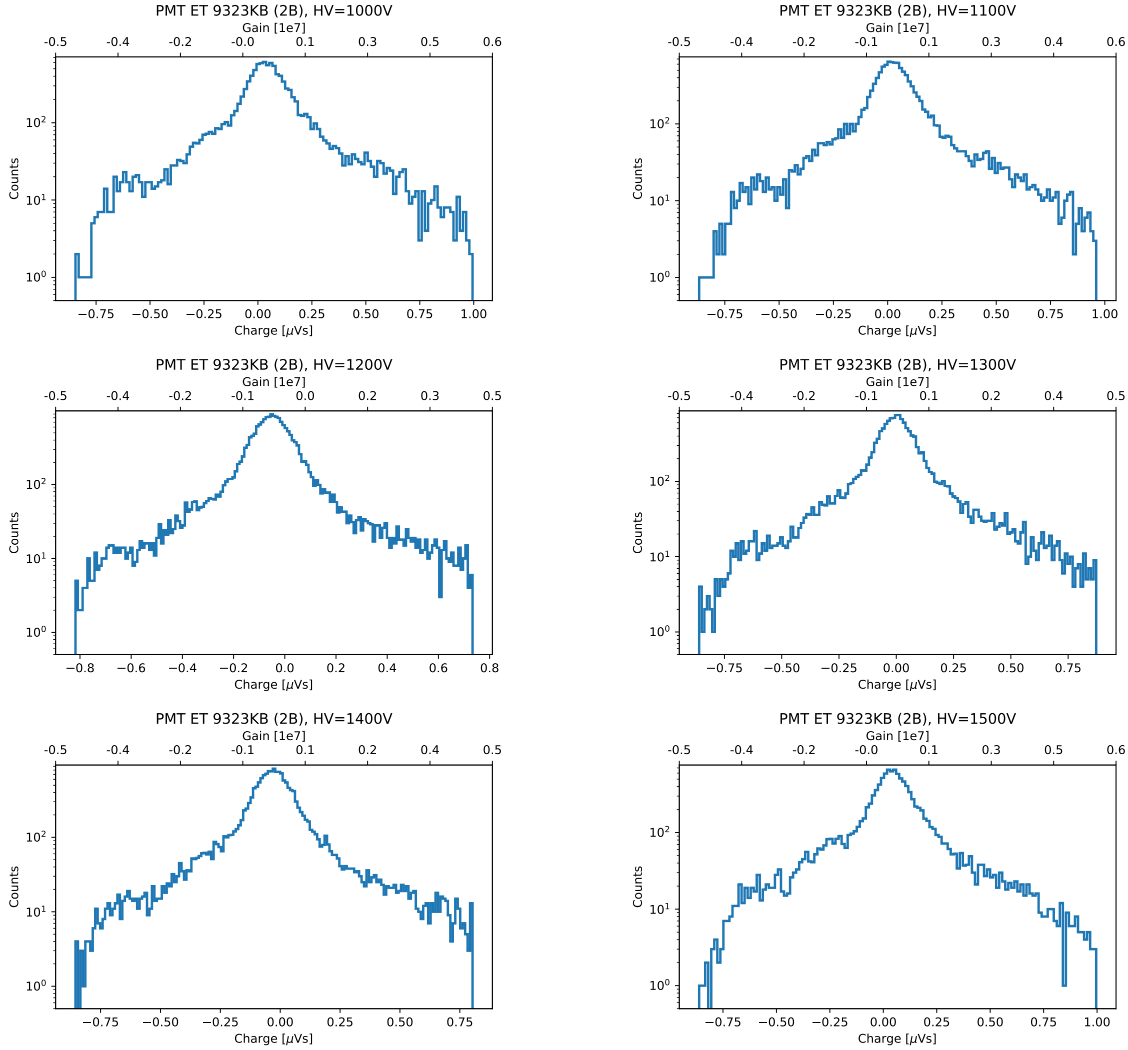

Figure A.15: Charge/gain histograms for the ET 9323KB (2) PMT, base B.

A.2.3 Gain-HV Dependence

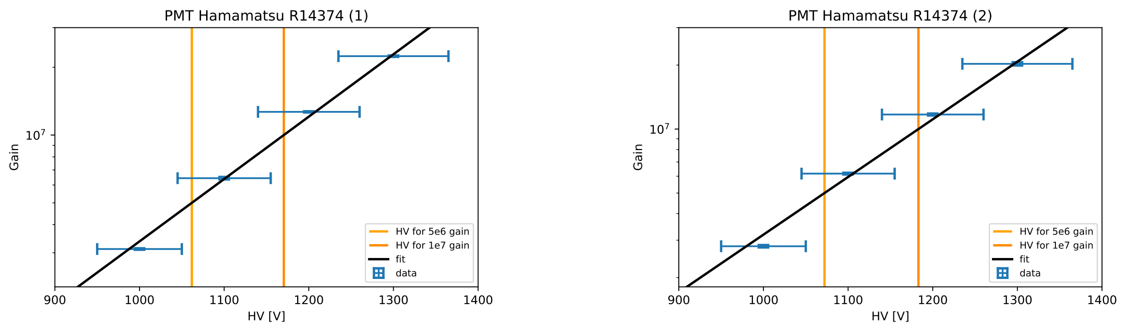

Figure A.16: Gain dependence on supply voltage (HV) with fit and vertical lines at y-values for gain=5×10^6 and 1×10^7 for the Hamamatsu R14374 PMTs.

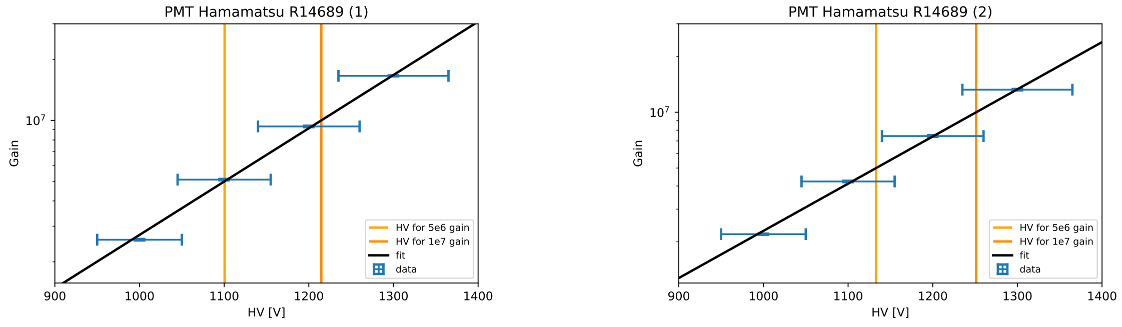

Figure A.17: Gain dependence on supply voltage (HV) with fit and vertical lines at y-values for gain=5×10^6 and 1×10^7 for the Hamamatsu R14689 PMTs.

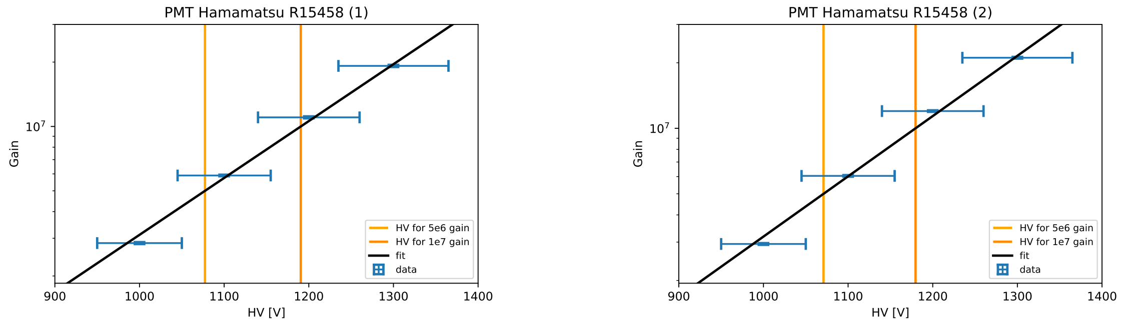

Figure A.18: Gain dependence on supply voltage (HV) with fit and vertical lines at y-values for gain=5×10^6 and 1×10^7 for the Hamamatsu R15458 PMTs.

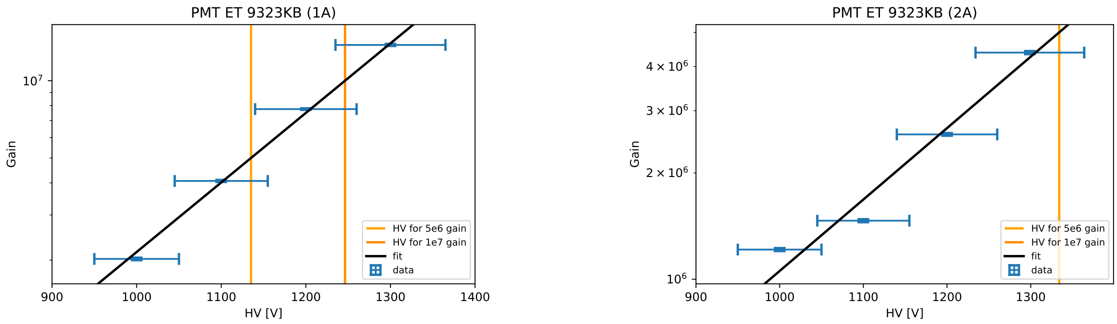

Figure A.19: Gain dependence on supply voltage (HV) with fit and vertical lines at y-values for gain=5×10^6 and 1×10^7 for the ET 9323KB PMTs, base A.

A.2.4 Transit Time Spread

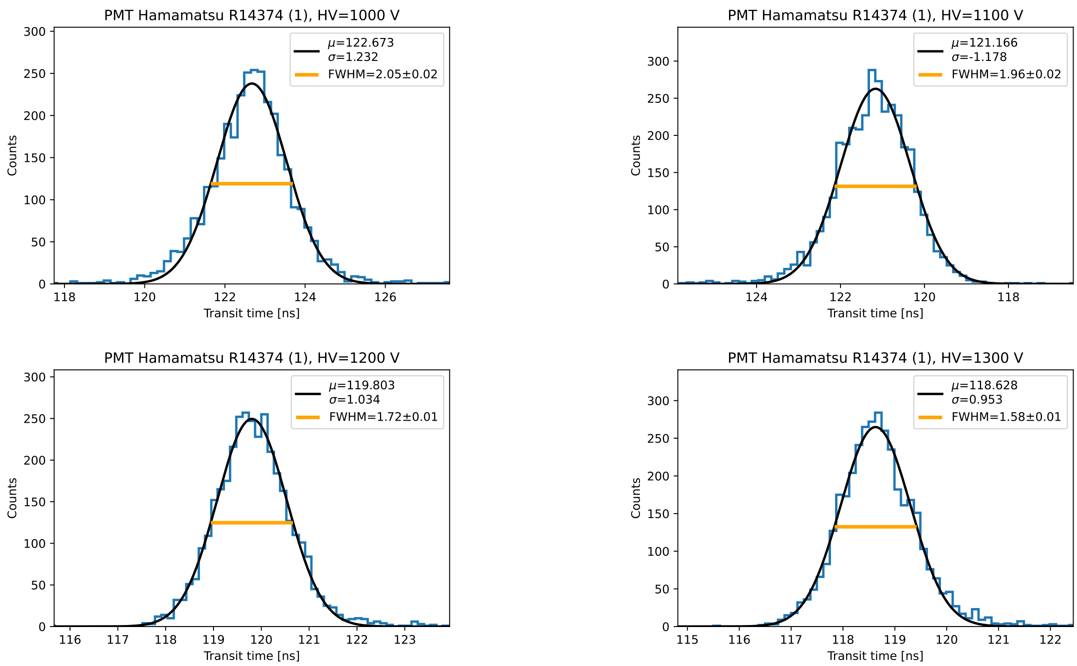

Figure A.20: Transit time histograms with fit for the Hamamatsu R14374 (1) PMT. The FWHM represents the TTS in ns.

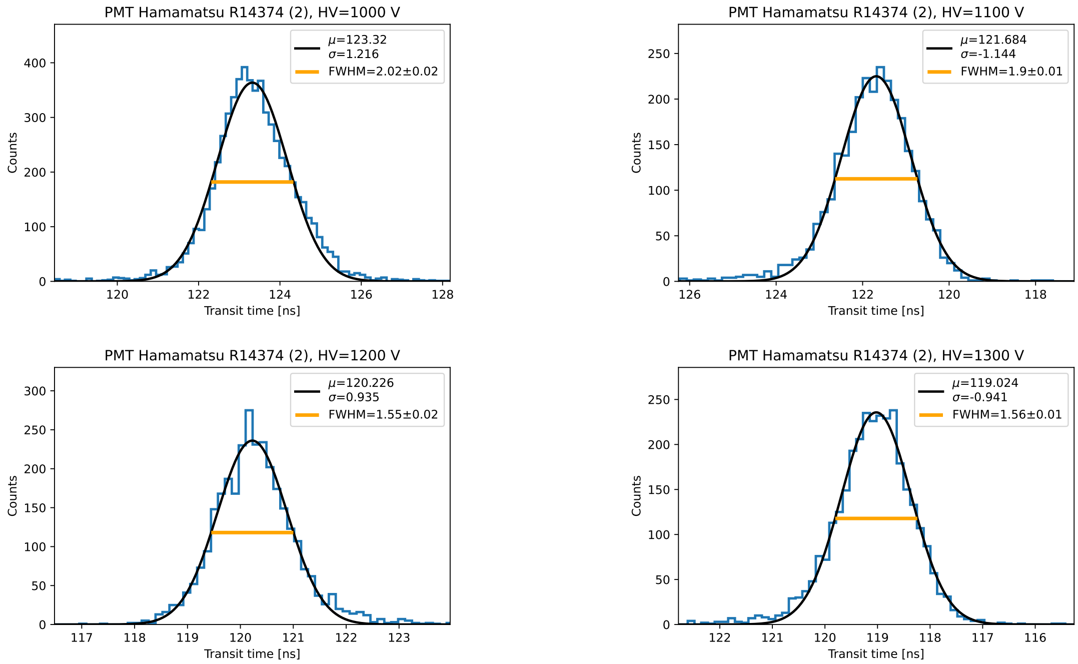

Figure A.21: Transit time histograms with fit for the Hamamatsu R14374 (2) PMT. The FWHM represents the TTS in ns.

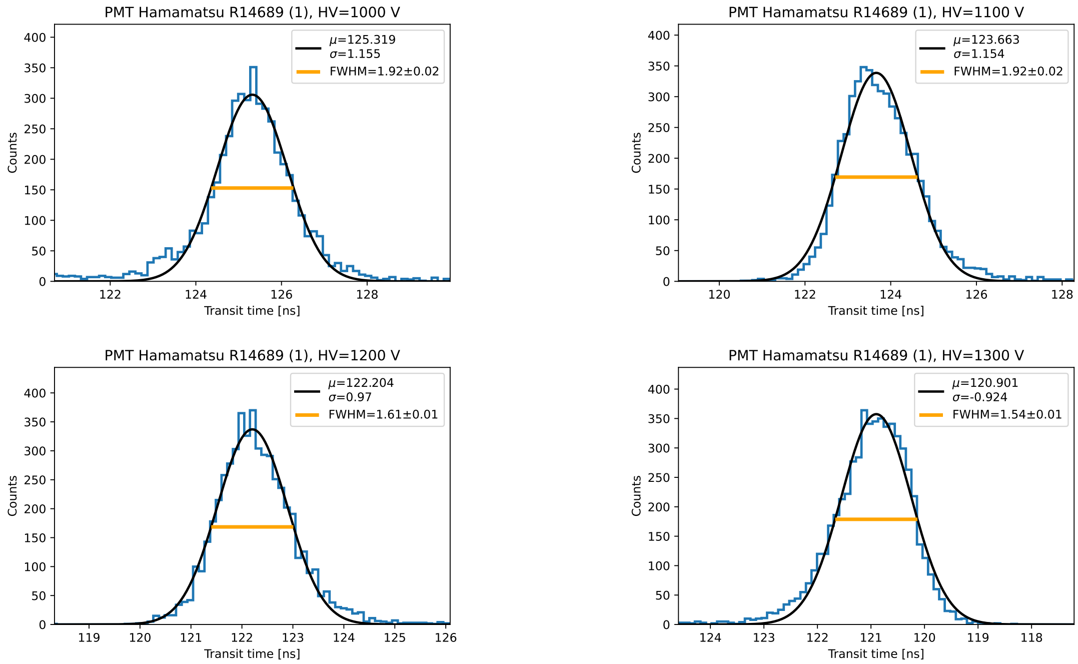

Figure A.22: Transit time histograms with fit for the Hamamatsu R14689 (1) PMT. The FWHM represents the TTS in ns.

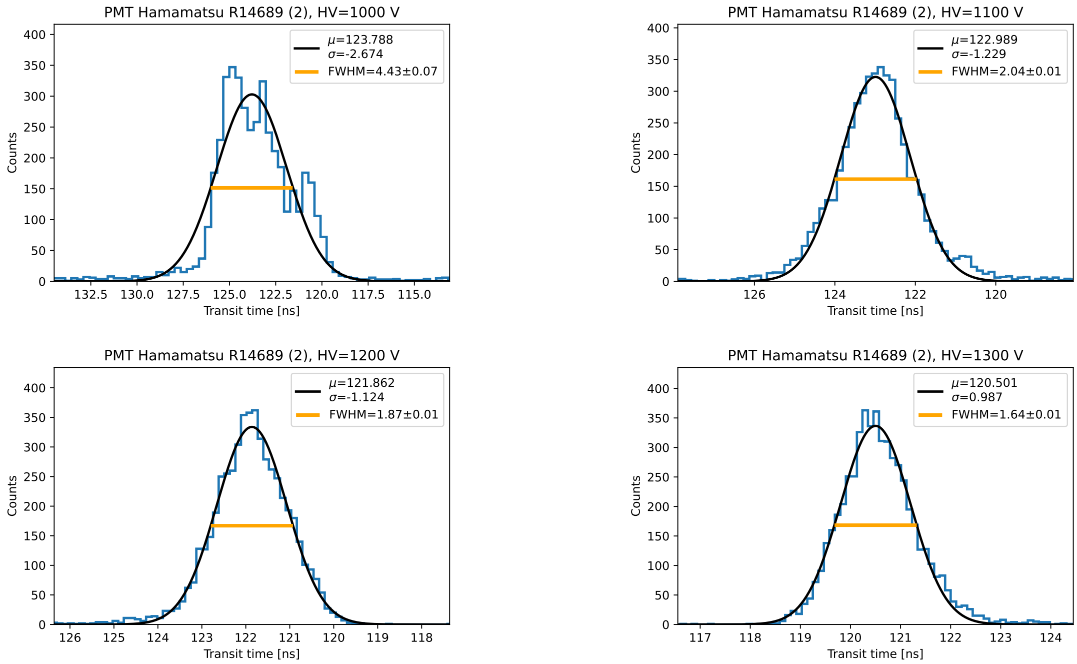

Figure A.23: Transit time histograms with fit for the Hamamatsu R14689 (2) PMT. The FWHM represents the TTS in ns.

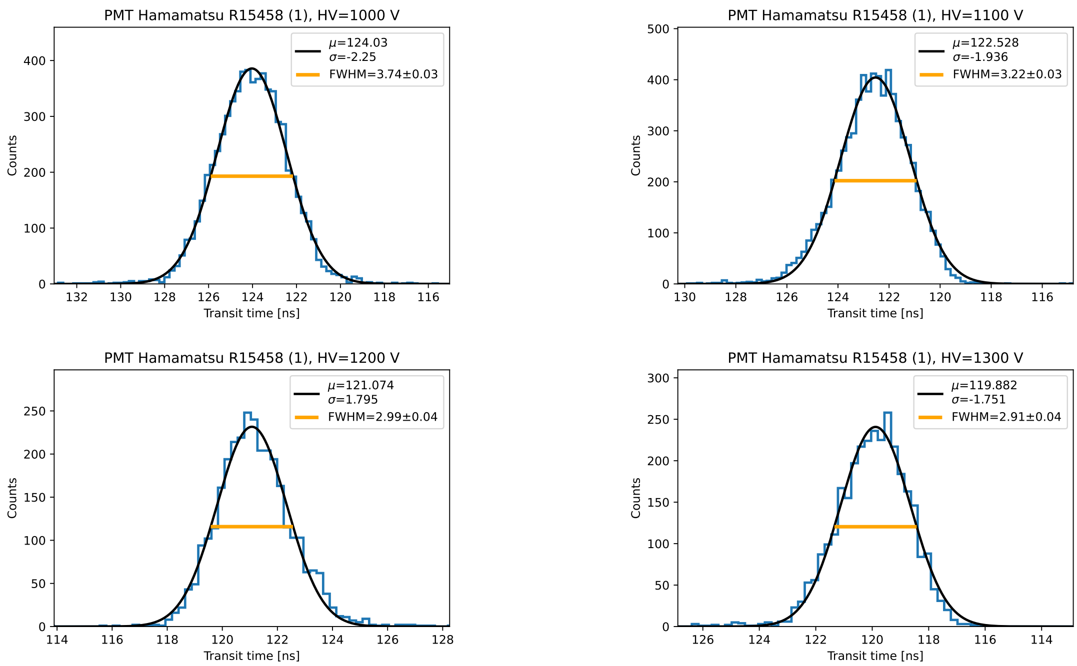

Figure A.24: Transit time histograms with fit for the Hamamatsu R15458 (1) PMT. The FWHM represents the TTS in ns.

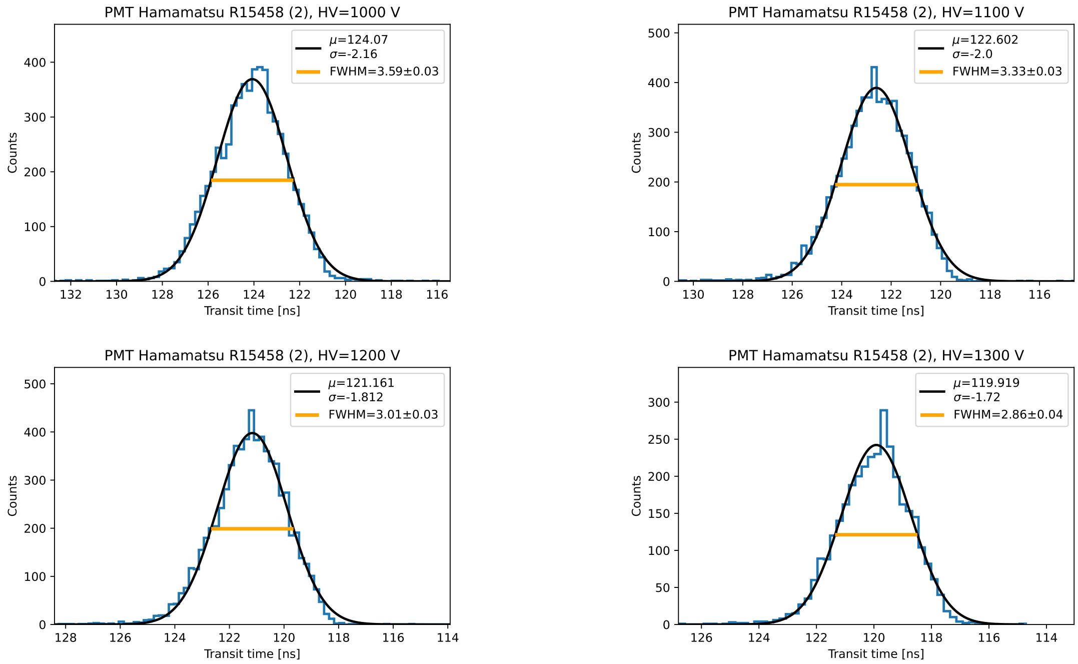

Figure A.25: Transit time histograms with fit for the Hamamatsu R15458 (2) PMT. The FWHM represents the TTS in ns.

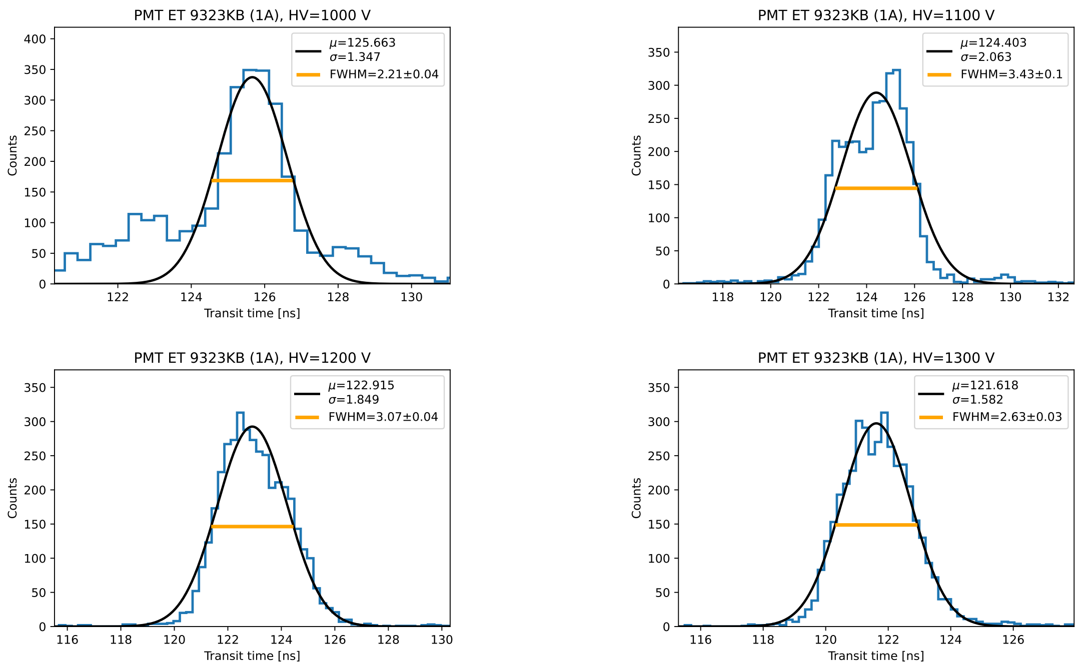

Figure A.26: Transit time histograms with fit for the ET Enterprise 9323KB (1) PMT, base A. The FWHM represents the TTS in ns.

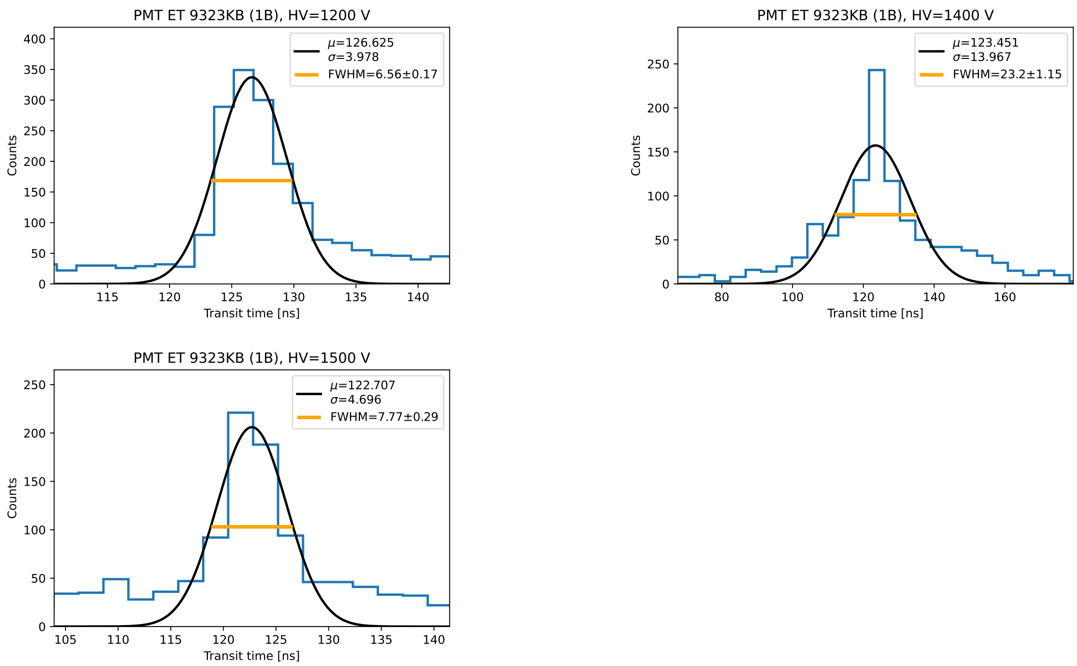

Figure A.27: Transit time histograms with fit for the ET Enterprise 9323KB (1) PMT, base B. The FWHM represents the TTS.

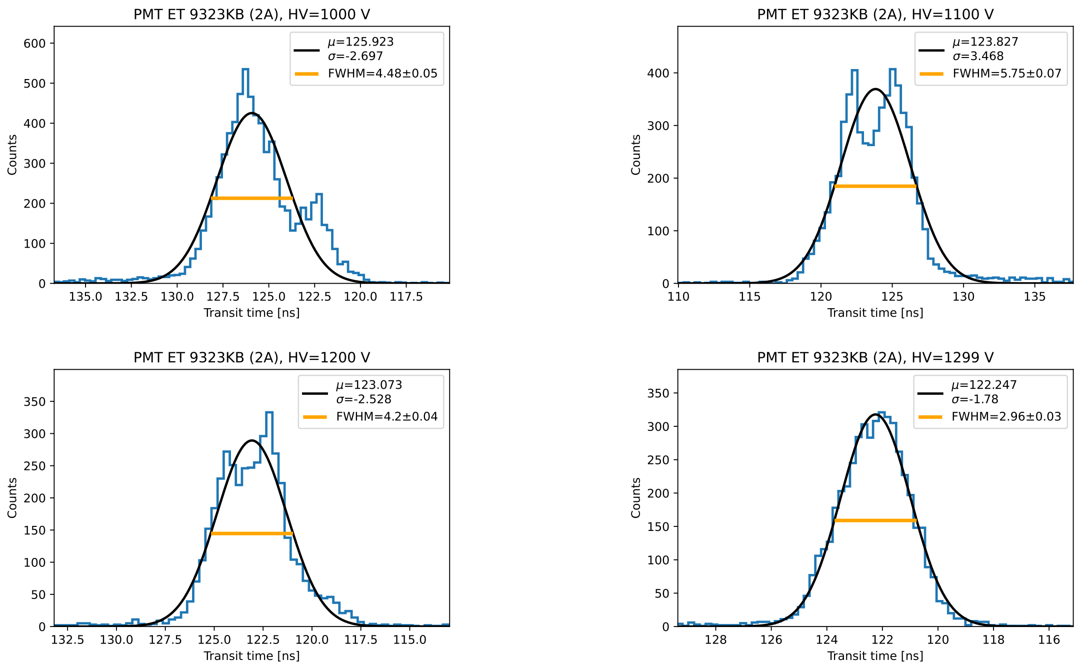

Figure A.28: Transit time histograms with fit for the ET Enterprise 9323KB (2) PMT, base A. The FWHM represents the TTS in ns.

A.3 Error Propagation

In this section the calculations of the error propagation are presented. For a measured value

$$g = g(x, y, z)$$

the mean is given by

$$\bar{g} = g(\bar{x}, \bar{y}, \bar{z})\,.$$

The error can be calculated using the formula for Gaussian error propagation

$$\Delta g = \sqrt{\Delta x^2 \left[\frac{\partial g}{\partial x}\right]^2_{\bar{x},\bar{y},\bar{z}} + \Delta y^2 \left[\frac{\partial g}{\partial y}\right]^2_{\bar{x},\bar{y},\bar{z}} + \Delta z^2 \left[\frac{\partial g}{\partial z}\right]^2_{\bar{x},\bar{y},\bar{z}}}\,. \tag{A.1}$$

For the special case that g is given by only sums or differences

$$g = \pm x \pm y \pm z\,,$$

the error is calculated by

$$\Delta \bar{g} = \sqrt{\Delta \bar{x}^2 + \Delta \bar{y}^2 + \Delta \bar{z}^2}\,. \tag{A.2}$$

For the special case that g is given by only products or quotients

$$g = \frac{x \cdot y}{z}\,,$$

the error is calculated by

$$\frac{\Delta \bar{g}}{g} = \sqrt{\left(\frac{\Delta \bar{x}}{\bar{x}}\right)^2 + \left(\frac{\Delta \bar{y}}{\bar{y}}\right)^2 + \left(\frac{\Delta \bar{z}}{\bar{z}}\right)^2}\,. \tag{A.3}$$

A.3.1 Dark Rate

The dark rate is given by the dark counts divided by the time interval

$$\text{rate} = \frac{\text{counts}}{\text{time}}\,.$$

The uncertainty of the counts is

$$\Delta\text{counts} = \sqrt{\text{counts}}\,.$$

As the error in *time* is small in comparison, the error of the dark rate can be calculated by

$$\Delta\text{rate} = \overline{\text{rate}} \cdot \frac{\Delta\text{counts}}{\overline{\text{counts}}}\,.$$

A.3.2 Gain-HV

The HV is given by the set voltage at the PSU multiplied by the amplification factor 250. The systematic uncertainty of the voltage setting is 0.001 V. The error of the amplification was estimated with 5%. The error of the HV value can be calculated using equ. A.3:

$$\Delta\text{HV} = \overline{\text{HV}} \cdot \sqrt{\left(\frac{0.001}{\overline{\text{HV}}/250}\right)^2 + (0.05)^2}\,.$$

The HV values for gain=5×10^6 and 1×10^7 were calculated using a fit curve of the charge/gain histograms. The fit function gain=$g(\text{HV})$

$$g(\text{HV}) = \mathrm{e}^a \cdot \mathrm{e}^{b \cdot \text{HV}}$$

can be rearranged as a function HV(g)

$$\text{HV}(g) = \frac{1}{b} \cdot [\ln(g) - a]\,.$$

The error of HV can then be determined using equ. A.1:

$$\begin{aligned}\Delta\text{HV} &= \sqrt{\Delta a^2 \left[\frac{\partial\text{HV}}{\partial a}\right]^2_{\bar{a},\bar{b},\bar{g}} + \Delta b^2 \left[\frac{\partial\text{HV}}{\partial b}\right]^2_{\bar{a},\bar{b},\bar{g}}} \\ &= \sqrt{\Delta a^2 \cdot \frac{1}{\bar{b}^2} + \Delta b^2 \cdot \frac{1}{\bar{b}^4} \cdot [\ln(\bar{g}) - a]^2}\end{aligned}$$

for

$$\begin{aligned}\bar{g}_1 &= 5 \times 10^6 \\ \bar{g}_2 &= 1 \times 10^7\,.\end{aligned}$$

The fit function gives the values of the parameter a and b and their errors Δa and Δb.

A.3.3 Transit Time Spread

The TTS is determined by the FWHM of the Gaussian fit of the transit time histogram. It can be described as

$$\overline{\text{FWHM}} = x_2 - x_1$$

with x_1 and x_2, the x-values, where $y = y_{\text{max}}/2$. The error of the FWHM can calculated by using equ. A.2:

$$\Delta\text{FWHM} = \sqrt{\Delta x_1^2 + \Delta x_2^2}\,.$$

To determine the error of x_i, the fit function

$$y = a \cdot \exp\left[-\left(\frac{x-\mu}{\sigma}\right)^2\right]$$

needs to be rearranged as a function for x:

$$\pm x = \mu \pm \sigma \cdot \sqrt{-\ln\left(\frac{y}{a}\right)}\,.$$

The error can then calculated using A.1:

$$\begin{aligned}\Delta x &= \sqrt{\Delta a^2 \left[\frac{\partial x}{\partial a}\right]^2_{\bar{a},\bar{\mu},\bar{\sigma},\bar{y}} + \Delta\mu^2 \left[\frac{\partial x}{\partial \mu}\right]^2_{\bar{a},\bar{\mu},\bar{\sigma},\bar{y}} + \Delta\sigma^2 \left[\frac{\partial x}{\partial \sigma}\right]^2_{\bar{a},\bar{\mu},\bar{\sigma},\bar{y}} + \Delta y^2 \left[\frac{\partial x}{\partial y}\right]^2_{\bar{a},\bar{\mu},\bar{\sigma},\bar{y}}} \\ &= \sqrt{\frac{\Delta a^2 \cdot \sigma^2}{4a^2} \cdot \left[-\ln\left(\frac{y}{a}\right)\right]^{-1} + \Delta\mu^2 + \Delta\sigma^2 \cdot \left[-\ln\left(\frac{y}{a}\right)\right] + \frac{\Delta y^2 \cdot \sigma^2}{4y^2} \cdot \left[-\ln\left(\frac{y}{a}\right)\right]^{-1}}\end{aligned}$$

List of Abbreviations

AGN Active Galactic Nuclei 5, 9

AMANDA Antarctic Muon And Neutrino Detector Array 22

AMS Alpha Magnetic Spectrometer 5, 8

ANTARES Astronomy with a Neutrino Telescope and Abyss environmental RESearch 22, 23, 60

ARCA Astroparticle Research with Cosmics in the Abyss 23, 24

Baikal-GVD Baikal-Gigaton Volume Detector 22, 60

CC Charged Current 13, 18, 21

CMB Cosmic Microwave Background 7, 9, 17

CP Charge Parity 14, 15

DOM Digital Optical Module 22–24

DUMAND Deep Underwater Muon and Neutrino Detector 22

e.g. "exempli gratia" (lat.) = for example 8, 20, 42

FC Fibre-optic Connector 45

FC/APC Fibre-optic Connector, Angled Physical Contact 43, 45, 46

FC/PC Fibre-optic Connector, Physical Contact 45, 46

FWHM Full Width Half Max 35, 54, 55, 84–89, 92

GRB Gamma Ray Bursts 5, 9

GZK K. Greisen, G. Zatsepin and V. Kuzmin cut-off 6, 7

HV High Voltage 30, 40, 41, 43, 46, 47, 51–55, 59, 82, 83, 91

i.e. "id est" (lat.) = that is 15, 19, 20, 31, 33

IH Inverted Hierarchy (of neutrino mass eigenstates) 15

ISS International Space Station 5, 8

KM3NeT km^3 Neutrino Telescope 22–24, 37, 47, 60

LAT Large Area Telescope 5, 9, 10

LIGO Laser Interferometer Gravitational Wave Observatory 10

MAGIC Major Atmospheric Gamma Imaging Cherenkov 6, 10, 22

MMA Multi-Messenger Astronomy 8

n/a not available 48, 55

NASA National Aeronautics and Space Administration 5, 9

NC Neutral Current 13, 18, 21

NEPTUNE North East Pacific Time-series Underwater Networked Experiment 24

NH Normal Hierarchy (of neutrino mass eigenstates) 15

OMCU Optical Module Calibration Unit 40–44, 46, 55, 56, 59

ONC Ocean Networks Canada ii, 24, 60

ORCA Oscillation Research with Cosmics in the Abyss 23, 24

P-ONE Pacific Ocean Neutrino Experiment ii, 2, 22, 24, 26–30, 36–38, 58–60

PDE Photon Detection Efficiency 33

PKMS Pontecorvo-Maki-Nakagawa-Sakata (matrix) 14

PMT PhotoMultiplier Tube ii, 2, 19, 20, 22, 23, 28–30, 32–38, 40–56, 58, 59, 74–89

PSU Power Supply Unit 40, 43, 91

QE Quantum Efficiency 33, 37, 38, 56

SNR SuperNova Remnants 5, 9

spe Single Photoelectron 47, 52

STRAW STRings for Absorption length in Water ii, 24, 26, 29, 37

STRAW-b STRings for Absorption length in Water part b ii, 24, 26

TTS Transit Time Spread 35, 37, 38, 54, 55, 58, 84–89, 92

List of Figures

List of Tables

Listings

Bibliography

[1] M. G. Aartsen et al. "Measurement of South Pole ice transparency with the IceCube LED calibration system". In: *Nuclear Instruments and Methods in Physics Research, Section A: Accelerators, Spectrometers, Detectors and Associated Equipment* 711 (2013), pp. 73–89. ISSN: 01689002. DOI: 10.1016/j.nima.2013.01.054. arXiv: 1301.5361.

[2] M. G. Aartsen et al. "The IceCube Neutrino Observatory: Instrumentation and online systems". In: *Journal of Instrumentation* 12.3 (2017). ISSN: 17480221. DOI: 10.1088/1748-0221/12/03/P03012. arXiv: 1612.05093.

[3] M. G. Aartsen et al. "Differential limit on the extremely-high-energy cosmic neutrino flux in the presence of astrophysical background from nine years of IceCube data". In: *Physical Review D* 98.6 (2018), pp. 1–12. ISSN: 24700029. DOI: 10.1103/PhysRevD.98.062003. arXiv: 1807.01820.

[4] M.G. Aartsen et al. "Development of a General Analysis and Unfolding Scheme and its Application to Measure the Energy Spectrum of Atmospheric Neutrinos with IceCube". In: *Eur. Phys. J.* C75.116 (2015). DOI: 10.1140/epjc/s10052-015-3330-z.

[5] S. Abe et al. "Precision measurement of neutrino oscillation parameters with KamLAND". In: *Physical Review Letters* 100.22 (2008). ISSN: 00319007. DOI: 10.1103/PhysRevLett.100.221803. arXiv: 0801.4589.

[6] Y. Abe et al. "Reactor anti-electron-neutrino disappearance in the Double Chooz experiment". In: *Physical Review D - Particles, Fields, Gravitation and Cosmology* 86.5 (2012), pp. 1–21. ISSN: 15507998. DOI: 10.1103/PhysRevD.86.052008. arXiv: arXiv:1207.6632v4.

[7] S. Adrin-Martnez et al. "Measurement of the atmospheric muon-neutrino energy spectrum from 100 GeV to 200 TeV with the ANTARES telescope". In: *Eur. Phys. J.* C73.2606 (2013). DOI: https://doi.org/10.1140/epjc/s10052-013-2606-4.

[8] S. Adrin-Martnez et al. "Letter of intent for KM3NeT 2.0". In: *Journal of Physics G: Nuclear and Particle Physics* 43.8 (2016). ISSN: 13616471. DOI: 10.1088/0954-3899/43/8/084001. arXiv: 1601.07459.

[9] M. Ageron et al. “ANTARES: The first undersea neutrino telescope”. In: *Nuclear Instruments and Methods in Physics Research Section A: Accelerators, Spectrometers, Detectors and Associated Equipment* 656.1 (Nov. 2011), pp. 11–38. ISSN: 0168-9002. DOI: 10.1016/J.NIMA.2011.06.103. arXiv: 1104.1607.

[10] M. Ageron et al. “Dependence of atmospheric muon flux on seawater depth measured with the first KM3NeT detection units: The KM3NeT Collaboration”. In: *European Physical Journal C* 80.2 (2020), pp. 1–11. ISSN: 14346052. DOI: 10.1140/epjc/s10052-020-7629-z.

[11] Matteo Agostini et al. “The Pacific Ocean Neutrino Experiment”. In: *Nature Astronomy* 4.10 (2020), pp. 913–915. ISSN: 23973366. DOI: 10.1038/s41550-020-1182-4. arXiv: 2005.09493.

[12] S. Aiello et al. “Characterisation of the Hamamatsu photomultipliers for the KM3NeT Neutrino Telescope”. In: *Journal of Instrumentation* 13.5 (May 2018). ISSN: 17480221. DOI: 10.1088/1748-0221/13/05/P05035.

[13] S. Aiello et al. “Determining the neutrino mass ordering and oscillation parameters with KM3NeT/ORCA”. In: *European Physical Journal C* 82.1 (2022), pp. 1–16. ISSN: 14346052. DOI: 10.1140/epjc/s10052-021-09893-0.

[14] Behcet Alpat. “Alpha magnetic spectrometer (AMS02) experiment on the International Space Station (ISS)”. In: *Nuclear Science and Techniques/Hewuli* 14.3 (2003), p. 182. ISSN: 10018042.

[15] E. Andres et al. “The AMANDA neutrino telescope: principle of operation and first results”. In: *Astroparticle Physics* 13.1 (Mar. 2000), pp. 1–20. ISSN: 0927-6505. DOI: 10.1016/S0927-6505(99)00092-4.

[16] W. B. Atwood et al. “The large area telescope on the fermi gamma-ray space telescope mission”. In: *Astrophysical Journal* 697.2 (2009), pp. 1071–1102. ISSN: 15384357. DOI: 10.1088/0004-637X/697/2/1071. arXiv: 0902.1089.

[17] A.D. Avrorin et al. “Baikal-GVD: first results and prospects”. In: *EPJ Web of Conferences* 209.201 9 (2019), p. 01015. DOI: 10.1051/epjconf/201920901015.

[18] Nicolai Bailly et al. “Two-year optical site characterization for the Pacific Ocean Neutrino Experiment (P-ONE) in the Cascadia Basin”. In: *The European Physical Journal C* 81.12 (2021), pp. 1–11. ISSN: 1434-6044. DOI: 10.1140/epjc/s10052-021-09872-5. arXiv: 2108.04961.

[19] John Etienne Beckman. *Multimessenger astronomy.* 2021. ISBN: 978-3-030-68371-9.

[20] I A Belolaptikov et al. “The Baikal underwater neutrino telescope : Design , performance , and first results”. In: 7.97 (1997), pp. 263–282.

[21] M. Boehmer et al. "STRAW (STRings for Absorption length in Water): Pathfinder for a neutrino telescope in the deep Pacific Ocean". In: (2019). arXiv: arXiv:1810.13265v5.

[22] Burle Industries Inc. *Photomultiplier Handbook*. Tech. rep. 1980.

[23] J. Carr and G. Hallewell. "Neutrino telescopes in the Mediterranean Sea". In: *New Journal of Physics* 6 (2004), pp. 1–31. ISSN: 13672630. DOI: 10.1088/1367-2630/6/1/112.

[24] K. Daum et al. "Determination of the atmospheric neutrino spectra with the Frejus detector". In: *Zeitschrift fr Physik C Particles and Fields* 66 (1995), pp. 417–428. DOI: https://doi.org/10.1007/BF01556368.

[25] Raymond Davis, Don S. Harmer, and Kenneth C. Hoffman. "Search for Neutrinos from the Sun". In: *Phys. Rev. Lett.* 20.21 (1968), pp. 1205–1209. DOI: 10.1103/PhysRevLett.20.1205.

[26] Alessandro De Angelis and Mrio Pimenta. *Introduction to Particle and Astroparticle Physics*. 2018. ISBN: 978-3-319-78180-8.

[27] W. Demtroeder. *Experimentalphysik 4 Kern-, Teilchen- und Astrophysik*. 2014. ISBN: 9783642254659.

[28] ET Enterprises. *Data sheet PMT 9323KB*. Tech. rep. 2021.

[29] Brigitte Falkenburg and Wolfgang Rhode. *From Ultra Rays to Astroparticles*. July. 2012. ISBN: 2013206534.

[30] Josep Flix. "The MAGIC Cherenkov Telescope for gamma ray astronomy". In: (2003), pp. 1–4. arXiv: 0311207 [astro-ph].

[31] S. Fukuda et al. "Determination of solar neutrino oscillation parameters using 1496 days of Super-Kamiokande-I data". In: *Physics Letters, Section B: Nuclear, Elementary Particle and High-Energy Physics* 539.3-4 (2002), pp. 179–187. ISSN: 03702693. DOI: 10.1016/S0370-2693(02)02090-7. arXiv: 0205075 [hep-ex].

[32] Y. Fukuda et al. "Study of the atmospheric neutrino flux in the multi-GeV energy range". In: *Physics Letters, Section B: Nuclear, Elementary Particle and High-Energy Physics* 436.1-2 (1998), pp. 33–41. ISSN: 03702693. DOI: 10.1016/S0370-2693(98)00876-4. arXiv: 9805006 [hep-ex].

[33] T. Gaisser, R. Engel, and E. Resconi. *Cosmic Rays and Particle Physics*. 2nd ed. Cambridge University Press, 2016. ISBN: 9781139192194.

[34] P. Giommi et al. "Dissecting the regions around IceCube high-energy neutrinos: Growing evidence for the blazar connection". In: *Monthly Notices of the Royal Astronomical Society* 497.1 (2020), pp. 865–878. ISSN: 13652966. DOI: 10.1093/mnras/staa2082. arXiv: 2001.09355.

[35] Carlo Giunti and Chung W. Kim. *Fundamentals of Neutrino Physics and Astrophysics*. 2007.

[36] Kenneth Greisen. "End to the Cosmic-Ray Spectrum?" In: *Phys. Rev. Lett.* 16.17 (1966), pp. 748–750. DOI: 10.1103/PhysRevLett.16.748.

[37] D. Griffiths. *Introduction to elementary particles*. Wiley, 2004. ISBN: 9780471603863.

[38] Claus Grupen. *Astroparticle Physics*. 2nd ed. 2020. ISBN: 9783030273415.

[39] Gwinstek. *Data sheet Power Supply*. Tech. rep. URL: https://www.farnell.com/datasheets/2267008.pdf.

[40] Hamamatsu. *Photomultiplier Tubes - Basics and Applications*. Tech. rep. 2017. URL: https://www.hamamatsu.com/eu/en/our-company/business-domain/electron-tube-division/related-documents.html.

[41] Hamamatsu. *Data sheet PMTs R12199, R14374, R14689*. Tech. rep. 2019.

[42] V.F. Hess. "ber Beobachtungen der durchdringenden Strahlung bei sieben Freiballonfahrten". In: (1912).

[43] K. Hirata et al. "Observation of a neutrino burst from the supernova SN1987A". In: *Phys. Rev. Lett.* 58.14 (1987), pp. 1490–1493. DOI: 10.1103/PhysRevLett.58.1490.

[44] Matthias Johannes Huber. "Multi-Messenger correlation study of Fermi-LAT blazars and high-energy neutrinos observed in IceCube". PhD thesis. 2020.

[45] IceCube Collaboration. *IceCube Multi-Messenger Propagation*. URL: https://gallery.icecube.wisc.edu/internal/d/318865-1/physicus.pdf.

[46] IceCube Collaboration. "Neutrino emission from the direction of the blazar TXS 0506 + 056 prior to the IceCube-170922A alert". In: (2018). arXiv: arXiv:1807.08794v1.

[47] IceCube Collaboration et al. "Multi-messenger observations of a flaring blazar coincident with high-energy neutrino". In: (2018). arXiv: arXiv:1807.08816v1.

[48] IceCube Masterclass. *The Detection of Neutrinos in IceCube*. URL: https://masterclass.icecube.wisc.edu/en/learn/detecting-neutrinos.

[49] Albrecht Karle. "IceCube: Construction status and first results". In: *Nuclear Instruments and Methods in Physics Research, Section A: Accelerators, Spectrometers, Detectors and Associated Equipment* 604.1-2 SUPPL. (2009), pp. 1–8. ISSN: 01689002. DOI: 10.1016/j.nima.2009.03.180. arXiv: 0812.3981.

[50] Keithley. *Data sheet Picoammeter 6482*. Tech. rep. URL: https://www.farnell.com/datasheets/1697244.pdf.

[51] KM3NeT Collaboration. *KM3NeT Web Page*. URL: https://www.km3net.org/.

[52] M. L. Kntig. "Light Sensor Candidates for the Cherenkov Telescope Array". PhD thesis. Technical University Munich, 2012.

[53] Kurokesu. *Data sheet Rotary stage RSA1*. Tech. rep. 2017. URL: https://kurokesu.com/uploads/datasheets/Kurokesu%7B%5C_%7DRSA1.pdf.

[54] LIGO Caltech. *LIGO Web Page*. URL: https://www.ligo.caltech.edu/page/what-are-gw.

[55] Annarita Margiotta. "The KM3NeT deep-sea neutrino telescope". In: *Nuclear Instruments and Methods in Physics Research, Section A: Accelerators, Spectrometers, Detectors and Associated Equipment* 766 (2014), pp. 83–87. ISSN: 01689002. DOI: 10.1016/j.nima.2014.05.090. arXiv: 1408.1392.

[56] Mathieu de Naurois and Daniel Mazin. "Ground-based detectors in very-high-energy gamma-ray astronomy". In: *Comptes Rendus Physique* 16.6-7 (2015), pp. 610–627. ISSN: 18781535. DOI: 10.1016/j.crhy.2015.08.011. arXiv: 1511.00463.

[57] Newport. *Optical Power and Energy Meters Optical Power and Energy Meters*. Tech. rep. URL: https://www.newport.com/medias/sys%7B%5C_%7Dmaster/images/images/h3b/hb5/8796989751326/1936-R-2936-R-Power-and-Energy-Meter-Datasheet.pdf.

[58] Ocean Networks Canada. *ONC Web Page*. URL: https://www.oceannetworks.ca/.

[59] P Padovani et al. "Dissecting the region around IceCube-170922A : the blazar TXS 0506 + 056 as the first cosmic neutrino source". In: (2018). arXiv: arXiv:1807.04461v1.

[60] NKT Photonics. *Data sheet Pilas DX*. Tech. rep. URL: https://contentnktphotonics.s3-eu-central-1.amazonaws.com/Datasheets/PILAS/ALS%7B%5C_%7DPilas%7B%5C_%7DDX.pdf?1639731741.

[61] Pico Technology. *Data sheet PicoScope 6000E Series*. Tech. rep. URL: https://www.picotech.com/download/datasheets/picoscope-6000e-series-data-sheet.pdf.

[62] Pico Technology. *Github PicoTech*. URL: https://github.com/PicoTech.

[63] Pico Technology. *PicoScope 6000 Series (A API) Programmer's Guide*. Tech. rep. URL: https://www.picotech.com/download/manuals/picoscope-6000-series-a-api-programmers-guide.pdf.

[64] B. Povh et al. *Teilchen und Kerne*. 2014. ISBN: 978-3-642-37821-8.

[65] Immacolata Carmen Rea et al. “P-ONE second pathfinder mission: STRAW-b”. In: *PoS (ICRC2021) 1092*. 2021. DOI: https://doi.org/10.22323/1.395.1092.

[66] Elisa Resconi and P-ONE Collaboration. “The Pacific Ocean Neutrino Experiment”. In: *PoS (ICRC2021) 024*. 2021. DOI: 10.22323/1.395.0024. arXiv: 2111.13133.

[67] Lisa Schumacher et al. “Plenum: A global and distributed monitoring system of high-energy astrophysical neutrinos”. In: *PoS (ICRC2021) 1185*. 2021. DOI: https://doi.org/10.22323/1.395.1185.

[68] Science Communication Lab and Deutsches Elektronen-Synchrotron DESY. *Multi-messenger Astronomy*. URL: https://multimessenger.desy.de/.

[69] Christian Spannfellner and Matthias Danninger. “Pacific Ocean Neutrino Experiment (P-ONE): prototype line development”. In: *PoS (ICRC2021) 1197*. 2021. DOI: https://doi.org/10.22323/1.395.1197.

[70] M. Spurio. *Particles and Astrophysics - A Multi-Messenger Approach*. 2016. ISBN: 9783319080505.

[71] Maurizio Spurio. *Probes of Multimessenger Astrophysics*. 2nd ed. 2018. ISBN: 9783319968537.

[72] S. Tavernier. *Experimental Techniques in Nuclear and Particle Physics*. 2010. ISBN: 9783642008283.

[73] A. G. Wright. *The Photomultiplier Handbook*. 2017.

[74] G. T. Zatsepin and V. A. Kuz'min. “Upper Limit of the Spectrum of Cosmic Rays”. In: *Journal of Experimental and Theoretical Physics Letters* 4 (1966), pp. 78–80.

[75] Kai Zuber. *Neutrino Physics,* 2nd ed. 2011. ISBN: 9781420064728.

Acknowledgements

I want to thank all the people that helped me throughout the past year.

First, I want to thank Elisa. Your urgency to involve and listen to young people as much as to the experienced ones and your never-ending thirst for knowledge are inspiring. With your wise and observing words, you have truly helped me believe more in myself and my capabilities. Thank you for believing in me.

A big thanks goes to Christian (CS, of course). Together we developed this cool setup. Even though I didn't call it that too many times, I do believe in our achievement. Thank you for being an understanding supervisor and the best office-mate I could have wished for.

To complete the list of the three Christians, I would like to thank Christian Fruck (CF) and Christian Haack (CH), who both seem to have a smart answer to everything. And together with Felix and Kilian, I want to thank you all for helping me with my programming questions.

I want to thank all the other members of the ECP, a unique group of people. Especially, the ones who are always there: Martina and Stephan. Thank you for all the good conversations during lunch breaks and for pushing me when I needed it.

I want to thank also my parents, who always support me. Thank you for not putting any pressure on me but trying to release it, and for always being there for me.

And last but not least, Henni. What would I do without you? Thank you for supporting me throughout this year, helping me with programming issues, and cooking for me when I was in the office or the library all day. Thank you for coming all the way to Utrecht to support me during the last couple of days of writing. I am grateful to have you.